NANOFABRICATED FLUID-FILLED CHANNELS FOR ANALYSIS OF SINGLE DNA MOLECULES

A Dissertation

Presented to the Faculty of the Graduate School

of Cornell University

In Partial Fulfillment of the Requirements for the Degree of

Doctor of Philosophy

by

John Thomas Mannion

January 2009

NANOFABRICATED FLUID-FILLED CHANNELS FOR ANALYSIS OF SINGLE DNA MOLECULES

John Thomas Mannion, Ph. D.

Cornell University 2009

Nanofabricated, fluid filled channels are presented as tools for the manipulation and detection of single DNA molecules. Both the conformation and position of DNA molecules within such devices can be controlled using a combination of electrophoretic and entropic forces. Application of these forces allows for fluorescently labeled molecules to be stretched in the channel, visualized using fluorescence microscopy, and analyzed in a number of ways, providing valuable and biologically relevant information about a DNA sample. In addition to investigating fluorescence microscopy as a means for sensing molecules in the channel, the possibility of electrical detection is explored. To this end, a fabrication method is described which allows for the integration of single walled carbon nanotube sensors and nanofluidic channels. While this device is currently being tested, it is intended that the incorporated carbon nanotubes may be used in a field effect transistor mode with the goal of detecting perturbations in local solution potential caused by DNA molecules as they are driven through the channels.

BIOGRAPHICAL SKETCH

John T. Mannion was born to Dr. John D. Mannion and Maryanne Mannion at New York Hospital in Manhattan's Upper East Side on November 9, 1980 at 6:04pm. In July of 1983 John, his younger brother Mark, and their parents, 30 and 28 years of age, moved to Burlington County in south Jersey, an area in which they lived for the subsequent 19 years. During that time, several new and interesting individuals were introduced into the family. Christina, David, and Mary Rose, all starting off as little shrimps, quickly turned into real people, and became John's best friends.

For various lengths of time, each of the three guys and two girls attended Our Lady of Good Counsel Roman Catholic grade school, in Moorestown, NJ. In 1995, John began at St. Joseph's Preparatory school in Philadelphia, PA, where he dedicated himself to two personal causes: grades and rowing. The work paid off, and in 1999 John matriculated at Princeton University. While an undergraduate, he was a member of the Varsity Lightweight Rowing team, through which he met some of his closest friends. He pursued an undergraduate degree in Physics, with a certificate in Biophysics. The summer before his senior year, after learning a little about nanotechnology, he applied to graduate school with the hope of working in that area.

At the end of his first year at Cornell, he began research in nanofluidics in the lab of Professor Harold Craighead. During his time there, John received an education in the field of Applied Physics and learned the fundamentals of nanofabrication. He has recently accepted a position as a research scientist in the molecular diagnostics division of Agilent Labs in Santa Clara, CA, where he hopes to continue work in the area of nanofluidics for lab on chip diagnostics.

To My Grandparents:

Theresa and Ferdinand T. Armenti

Mary Rose and John V. Mannion

ACKNOWLEDGMENTS

As is evidenced by the list of multiple authors presented at the beginning of several chapters of this thesis, many people contributed to the work described here. It is important to acknowledge both their efforts and the efforts of many others who are not listed as co-authors. Additionally in this section, I would like to thank friends and family members who have provided support and guidance over the course of the graduate school experience.

I would like to thank Harold Craighead for being an excellent Ph.D. advisor. To begin with, the opportunity that was available to me, to perform research and receive an education in the field, existed because of him. But more than that, Harold has created an environment in which students are greatly encouraged to pursue original ideas. In addition to establishing a research course through the field of bio-nanotechnology, and guiding students to perform meaningful experiments, he has also allowed space for his students to pursue their own novel concepts. In my own experience, regardless of how risky my proposed techniques appeared, or how difficult the processes proved to be, Harold never lost his willingness to permit continued investigation. This was an extremely encouraging environment within which to work.

Harold's work experience is unique for a professor in that it is of both the academic and business areas, which enables him to advise students interested in either. He had many conversations with me regarding the possible directions my own career could take, long before it was time to start writing the thesis. Both the specific words of advice and the interest that he showed in my future were greatly beneficial.

I would also like to thank the two other professors who served on my thesis committee, Paul McEuen and Brian Kirby. They have provided much thought and attention to the research projects described in the thesis, and to the written document itself. Much of the work from the later chapters was carried out using the facilities available in Paul McEuen's lab for growing and measuring carbon nanotubes. During the two and a half years in which I frequented the McEuen labs, I received nothing but encouragement and assistance from Paul and his students. As a person who knew very little about carbon nanotubes at the start, I was relieved to find so many experts happy to pause from their work and answer my ridiculous questions. The individuals who answered a particularly large number of those questions are Yaqiong Xu, Nathan Gabor, Lisa Larrimore, Arend van der Zande, Patrycja Paruch, Sam Roberts, Luke Donev, Shahal Ilani, Zhaohui Zhong.

Other members of the Craighead group have also played a major role in the research projects described in this thesis. First I would like to thank Steve Levy, who has proofread every chapter of this thesis. He is co-first-author of Chapter 5, which is a recently accepted article in the journal Nano Letters. This article is the result of approximately two years of fabrication and lab work by the two of us. He is exclusively responsible for the Matlab program used for image analysis of DNA video data, and we worked together to determine proper methods of data analysis and theoretical models for DNA dynamics. Steve has also been a partner in the carbon nanotube project, which is the topic of Chapters 6 and 7. For this he has worked together with me on fabrication, design of the experimental setup and development of experimental procedures.

Christian Reccius and Josh Cross are previous group members whose names appear on

the author list of Chapter 4, a published article on DNA dynamics. Christian and Josh were both experienced researchers who taught me much during the first few years in graduate school. Christian performed much work for the project described in Chapter 4. For this he and I worked together on fabrication, experimental procedures and data analysis, and he is exclusively responsible for the Matlab program used to extract data from video files.

Other group members who deserve a great deal of thanks are Seung-min Park, Ben Cipriany, Elizabeth Strychalski, Leon Bellan, Madhukar Varshney, Scott Verbridge, Christine Tan, Samuel Stavis, Kevan Samiee, Jose Moran-Mirabal, Paul Zhu, Philip Waggoner and Grant Meyer.

Two others worked, for one semester each, with Steve Levy and I on DNA dynamics in nanochannels. Sebastien Ricoult worked with us during the summer of 2007 as part of an undergraduate internship. He performed valuable data analysis. Jim Cheng assisted Steve and I during the spring of 2008, while on group rotation during his first year in graduate school. Jim ran DNA unfolding experiments, processed video data, helped to develop theoretical models for our observations, and is a co-author of the article shown in Chapter 5.

Due to the nature of the research projects, at least half of the work for this thesis required use of the Cornell Nanoscale Facility (CNF), which is home to nanofabrication equipment and a dedicated team of staff members. I would like to thank several staff members including Rob Ilic and Meredith Metzler (also both former Craighead group members) for the enormous amount of training and technical advice they have provided over the past five years. These two have saved fabrication

projects from certain failure on several occasions. Thanks also to Dan Woodie, Phil Infante, Kelly Baker, Garry Bordonaro, Jim Clair, Jerry Drumheller, Mike Skvarla, Daron Westly, Sam Wright and Edward Camacho. I would also like to thank Steve Jones who is a regular CNF user. Steve is extremely knowledgeable and generous in helping students while they attempt to learn fabrication techniques.

Finally it only seems right to thank the friends and family members who provided a network of support and encouragement during the Ph.D. process. Thanks to Grant Meyer, for being a great friend and roommate during the past five years. Thanks to Andrew Chadeayne for showing me the bike and what it means to "send it back." Thanks to David Manke for integrating Clint Eastwood and Denny Crane into my vision of the ideal man. The three friends above were always there to talk with, grill a burger with, or drink a glass of scotch with, and the Ph.D. experience would not have been nearly as enjoyable without them.

Thanks also to my family members who have given their constant attention and support. Thanks to my Mom and Dad for being a source of good advice regardless of type of situation their son encountered. I would not be writing this thesis were it not for years filled with their guidance and encouragement. Mom has been there with an unwavering positive attitude, a love for her family, an incredible kindness towards others, and the knowledge that things will always work out in the end. Dad has put family first throughout his whole life. He is a great example of success through hard work, determination, generosity and thoughtful analysis on behalf of those around him. Thanks also to Mom and Dad for their constant interest in research updates and in how life was going in Ithaca during my time in graduate school.

My brothers and sisters, Mark, Christina, David and Mary, have been good allies throughout the graduate school years. Whether it was a motivational phone call from Mark, a timely and sweet one-liner from Dave, an encouraging conversation with Christina, or a much needed and supportive conversation with Mary, they have always been there for me during the long winters in Ithaca.

Finally, I would like to thank my four grandparents, to whom this thesis is dedicated. Mary Rose Mannion and John V. Mannion were great examples to me growing up. Grandma Mannion was one of the most well read and well travelled persons I have ever met. Grandpa Mannion was a highly successful business man and an incredible builder of teams. Theresa Armenti and Ferdinand Armenti were also great examples to me growing up. Grandpa Armenti worked as an inspector of highly complex machines. I remember many occasions on which he told me something I will never forget: “anything the human mind can imagine is possible.” More than anyone I know, Grandma Armenti has the ability to engage any person she meets in conversation. This comes from her rarely found quality, namely that she has a true interest in the details of the lives of others.

I thank my grandparents because they have been inspirational on many levels. As a child I received nothing but care from them, and they always passed down their wisdom in the most entertaining ways. They have encouraged and supported my growth and education. And finally, they have expressed, to me, a belief in the value of life and the goodness of people. I hope to follow their lead, I hope that I have made them proud and will continue to do so, and I cannot thank them enough for everything they have done.

John T. Mannion, October 2008

TABLE OF CONTENTS

LIST OF FIGURES

Chapter 1

Chapter 2

Chapter 3

Chapter 4

Chapter 5

Chapter 6

Chapter 7

LIST OF TABLES

CHAPTER 1
INTRODUCTION

1.1 Nanofluidic Channels for Observation of DNA Molecules

Nanofluidic channels are long, narrow cavities, manufactured in glass or silicon wafers by thin film fabrication methods. When filled with fluid, these structures can be used for the purpose of performing biological or chemical analysis on minute amounts of sample. Traditional nanoscale cavities, such as those that lie within polymer gels and nanoporous packed beds, have long been employed in separation science. However, it is only within the last decade or so that nanofabricated structures with lithographically defined geometries have been explored and utilized in analytical systems.

Already, arrays of nanoscale posts [1-4], traps [5-10], pores [11-13], wires [14-19], channels [20-23], and other structures have been tested in "lab-on-chip" devices. They have been used for the purposes of separating cells [24, 25], proteins [26], and DNA [4, 27] by size, charge and other properties, and for single molecule manipulation and detection [28]. In all cases, the devices derive their unique functionality from the fact that critical dimensions of the nanostructures are of similar order to the size of the molecules being analyzed. While there are many possible nanofabricated structures worth investigating, in this thesis we focus on the use of nanochannels for manipulation and observation of individual, double stranded DNA molecules.

There are two main reasons for studying DNA molecules in nanoscale channels. The first is technological, and the second is purely scientific. Technologically, lab on chip

devices with nanochannel features hold promise for automation of what are currently labor intensive DNA assays. For example, both fragment length analysis and optical mapping are widely used techniques in molecular biology, and both can be performed in nanochannels.

From a purely scientific point of view, the study of DNA conformation and dynamics in nanochannels can be used to validate theoretical models for confined polymers. Even since the 1970s have theorists been interested in this topic, and they developed models for confined polymers long before it was possible to image them experimentally [29, 30]. Here, we elaborate on the two areas which benefit from DNA/nanochannel experiments: bioanalytical technology and polymer theory.

1.2 Technological Applications of Single Molecule DNA Observation

In the past decade, considerable effort has been spent incorporating the DNA detection methods described above into lab on chip devices. It has long been believed that such devices would have the advantages of lower cost, faster run times, lower required sample volumes, a higher degree of automation, and portability [31-33]. Already there are a number of devices [34-40], both in commercial and proof of principle stages, that can obtain DNA sequence information and whose performance benefits from the advantages listed above.

DNA fragment length measurement is just one of the many types of procedures performed in bioanalysis, however its importance cannot be overstated. Nearly all gel and capillary based DNA electrophoresis techniques function to segregate the components of a heterogeneous collection of DNA molecules according to fragment length. The distance that a segregated plug of molecules is observed to migrate

through the separation medium can be used to infer fragment length. These length measurements, combined with other standard processes, such as digestion by restriction enzymes, yield valuable sequence information.

Here, we describe two examples of applications which directly employ measurement of DNA fragment lengths. In genetic fingerprinting, an individual's DNA is cleaved by an enzyme at a unique set locations along the genome. The result is a collection of fragments with a specific set of lengths for each individual. To determine molecular lengths, typically gel or capillary electrophoresis separations are performed. In order to generate enough DNA molecules for a strong signal, polymerase chain reaction (PCR) is used to amplify the DNA molecules before they are run through the separation medium. However, when nanochannels are used for sizing, the single molecule nature of the measurement precludes the need for pre-measurement DNA amplification. Another standard technique in which information is obtained from length measurements is the Sanger sequencing method. In this method a gel or capillary separation with single base resolution is used to infer a DNA sequence de novo. While nanochannel length measurements with single base resolution have not yet been demonstrated, such are theoretically possible.

Fragment length measurements are of great use, and we will see later why nanochannels are well suited for assisting with this. In some cases, however determining the lengths of various fragments in a sample is not enough. For example, biologists may wish to do such things as 1) correctly order the short sequences generated during shotgun sequencing, 2) detect genetic rearrangements within a chromosomes or between two different chromosomes, 3) identify an organism based on a hybridized probe fingerprint, a concept similar to the restriction enzyme

fingerprinting described above, with the difference being that the order of identified motifs is preserved, or 4) obtain epigenetic information.

One molecular biology technique used to obtain such information is called optical mapping. In optical mapping of the most general sense, the DNA backbone is labeled with a die of one color, and a probe with a second color is bound to some feature or a set of features on the DNA. Conceivably, those features may be anything from DNA motifs of a specific sequence, to proteins bound to the DNA or even methylation sites. The location of a particular sequence motif is determined by binding a complimentary oligomer probe with its own label. Other features may be identified by binding labeled antibodies. Either before or after the probes are bound, the entire DNA molecule can be elongated so that it is in a conformation suitable to optical investigation. The elongated molecules and bound probes are eventually imaged, resulting in a map which reveals the position of each probe relative to the end points of the DNA molecule.

The accuracy of optical mapping depends largely on the reliability of the DNA stretching method. One approach for elongating and stabilizing DNA is called molecular combing. In molecular combing, DNA molecules in solution are attached to a silanized glass slide and are then stretched out during evaporation of the solution. Microfluidic and nanofluidic channels offer new approaches for molecular elongation, and it is the belief of this author that nanochannels represent the best approach. The reasons for this will be discussed shortly.

1.3 Importance of the Theory of Confined Polymers

From a purely scientific standpoint, theoretical polymer physics benefits greatly from the study of DNA molecules in nanochannels. Double stranded DNA in a channel is an ideal system for studying both contour and dynamics of dilute, linear, self-avoiding polymers in confined environments. Here we mention two examples, from biology, of concepts that rely on an understanding of the behavior of confined polymers. Those situations are 1) the packing of a bacteriophage genome into its viral capsid head, and 2) segregation of chromosomal DNA molecules during cellular mitosis.

As part of the viral life cycle, viruses must package their newly replicated genomes for delivery into other host cells. Bacteriophage $\phi 29$ must package its 6.6 μm long double stranded DNA genome into a $42nm \times 54nm$ capsid. Because this space is smaller than the volume occupied by the DNA molecule in free solution, energy is required to pack it in tightly. In 2001 Smith et. al published a paper showing that the bacteriophage $\phi 29$ motor can package DNA against a large internal force [41].

According to concepts from polymer theory, the force resisting packing arises from the electrostatic and entropic repulsion between segments of the DNA molecule. In order to estimate such forces, an large number of models are available, however there is still much room for improving the models. Experiments involving DNA packed into nanochannels offer a unique opportunity to directly measure the forces required for compression.

Another example from biology is the segregation of chromosomal DNA molecules during cell division of rod shaped bacteria. This basic physical issue of chromosome segregation has been in question for many years, despite recent progress in in-vivo

visualization experiments. In 2006, Jun and Mulder [42] reported Monte Carlo simulations which suggest that under the strong confinement conditions of a rod shaped bacterial membrane, topologically distinct domains of a polymer complex repel each other through entropic repulsion. Computer simulations showed that this explanation can account for all of the major spatiotemporal features of the replicating circular chromosomes.

The following year, in a report by Arnold and Jun the segregation process was remodeled using molecular dynamics simulations [43]. In this article, a simpler topology was investigated, namely, two overlapping linear polymers confined to a nanochannel. It was again found that that the entropic repulsion between chains can be sufficiently strong to cause segregation over a time scale that is short compared to diffusion. Later in this chapter we describe a nanochannel-based single molecule experiment which gives support to the theory of entropic segregation.

As is evident, experiments which allow for direct observation of an ideal polymer, in environments with various degrees of confinement, are of great help in further development of polymer theory. The study of DNA in nanochannels is a valuable tool in this area (the study of DNA molecules with manipulation by optical tweezers [44] or magnetic beads [45] being an example of others). In the next section, and throughout this thesis, we give examples of specific nanochannel experiments which provide data to corroborate or modify concepts from polymer theory.

1.4 Specific Experiments Demonstrating the Use of Nanochannels and Similar Structures for DNA Analysis

In this section we review the literature of nanofluidic channel devices for DNA analysis. We also review work involving structures which differ slightly from nanochannels but which rely on the same principles and perform many of the same functions. The section is organized according to the geometry of the described structures. We start with microchannels, which are the largest of the structures discussed. We then review intermediate structures such as nanoslits, entropic traps, and pillar arrays. Finally, we discuss recent work on nanochannels. This section differs from Chapter 2, in that we do not presently develop the theory of confined polymers in detail or discuss measurement limitations. Instead we only give a survey of the performed experiments and the results. This section differs from Chapter 3 as well. Here the reviewed experiments are only those which involve DNA molecules, and do not include experiments involving zero mode waveguides. Throughout the following subsections, the relevance of the described experiments to either lab on chip technology or to polymer theory will be discussed.

1.4.1 Microchannel Devices

In 2002, Foquet et. al demonstrated a device in which double stranded DNA molecules were flowed through a microscale channel, and were illuminated with a focused laser spot [20]. Emitted light from the fluorescently stained molecules was collected, resulting in a series of pulses of various height and duration. It was found that the integrated intensity of each pulse corresponded linearly to the number of dye molecules present in the molecule. This in turn could be used to infer the number of base pairs in each DNA fragment.

As mentioned in Section 1.2, there are certain situations in biological analysis for which only a small amount of initial sample can be obtained but for which it is desirable to avoid pre-measurement amplification of DNA. This single molecule microchannel sizing technique was shown to be suitable for those situations. A histogram showing the various fragment populations in the sample was generated after detecting a total of just 10,000 molecules over a period of two minutes. This corresponds to only 76 fg of DNA.

The microchannels used in this experiment had cross sections which were large enough that DNA conformation was not significantly altered. The path of the flowing molecules through space was well defined by the channel walls, and the flow speed could be controlled using electroosmosis. This allowed for a sample which was dilute enough that the probability of having two molecules pass through the observation volume at the same time was extremely small. The moderate confinement of the channel walls, in conjunction with an under-filled objective, also allowed for an evenly illuminated observation volume. Had the intensity of incident light in the observation volume tapered significantly at the channel edges, reliable fragment sizing would not have been achievable.

The Foquet fragment sizing method is interesting because it performs the same measurement as pulsed gel electrophoresis. Pulsed gel is a technique used for separating large DNA molecules (10's of kb and larger), which typically requires high voltages and run times which are on the order of 10's of hours. The advantage of pulsed gel over the Foquet method is that it can be used as a preparative step in DNA purification. Typically, after separation of the molecules into bands, those bands may be cut out of the gel. Many DNA molecules are present in each band, and after the gel

is dissolved, the DNA can be used for other purposes. Foquet's method of single molecule observation and counting does not currently allow for recovery of the analyzed molecules. Although, one might imagine modifications of the chip that would permit single molecule sorting and collection.

In addition to being used for DNA sizing, microchannels can be employed in experiments which test polymer theory models. In 1997 Perkins et al. examined the stretching of DNA in elongational flow in microchannels [46]. Both the internal mechanics and hydrodynamic coupling between molecular segments were probed in this experiment. It was found that the molecule could be modeled as a wormlike chain. Tension was transmitted along the backbone, and a gradient of high tension at the center of the molecule and zero tension at the free ends was found to exist. This resulted in a number of possible dumbbell-like conformations

This type of analysis is critical for the refinement of polymer theory. The behavior of dilute polymers in elongational flow has been a topic of theoretical discussion since the 1970s, and single molecule theories had been developed [47], but the proposed models had not been tested by single molecule observation until the Perkins report in 1997. In elongational flows, the velocity gradient along the direction of flow stretches the polymer, and the polymer exerts a force back on the solvent. According to Perkins, this leads to non-Newtonian properties of dilute polymer solutions such as viscosity enhancement and turbulent drag reduction [46].

1.4.2 Nanoslits

While the uniform illumination volume and high throughput of single molecules through microchannels are advantages, microchannel cross sections are too large to

have an effect on the conformation and dynamics of a DNA molecule. A double stranded molecule does not need to deform in order to enter a microchannel. If the channel depth is made to be 10's of nanometers, however, then the story is a much different one. Long DNA strands must deform in order to enter the channel. In addition to altering DNA equilibrium conformation, this confinement affects both internal and external dynamics of the molecule.

As a demonstration of this, Bakajin et al studied DNA stretching and relaxation in nanoslit devices of various depths [48]. In the experiment, they electrophoretically drove a DNA molecule through a nanoslit until it happened to wrap around a pillar which was intentionally fabricated in the channel. This caused the DNA strand to elongate as would a ribbon hooked on a post in the wind. When the molecule finally freed itself from the pillar, it continued downstream, relaxing as it moved through the channel. This relaxation process was observed using fluorescence microscopy, and the end to end extension as a function of time was determined. It was found that relaxation time varied with nanoslit depth. It was also found that an electrophoretic force acts on a tethered molecule in same way as does a hydrodynamic flow. This concept was termed electrohydrodynamic equivalence.

The initial study by Bakajin was followed by a number of papers which investigate polymer dynamics in slits. In a series of works Doyle et. al experimentally investigated both the relaxation times and diffusivity of several lengths of DNA molecules in slits [49-52]. In keeping pace with experimental reports, theorists have used brownian dynamics simulations [53-55], dynamic Monte Carlo simulations [56], lattice Boltzmann methods [57] in attempts to explain the data, and to corroborate previously published analytical approaches to modeling polymers in slits [29]. Most

recently Levy and Strychalski of the Craighead group [58] and Bonthuis of the Dekker group [59] have investigated DNA diffusion in slits with depths of 33nm and higher. Proper theoretical interpretation of these experiments remains under debate, because there is still a discussion in the polymer physics community as to whether the models proposed by Brochard and deGennes' [29, 60] or Odijk [61, 62] should be used for DNA in nanoslits.

While the study of DNA in nanoslits is interesting from a polymer physics point of view, it also has significant technological application. Here we describe the methods being used to stretch and detect single DNA molecules in sub-micron sized channels for the purpose of rapid gene mapping. A key component of optical mapping analysis is elongation of DNA molecules so that they are in a conformation conducive to fluorescent visualization of hybridized probes or cleaved restriction sites. While molecular combing and other techniques stretch DNA and affix it to a surface, it is also possible to elongate a DNA molecule in a controlled way, and interrogate it while it is still in solution. Two approaches to single molecule elongation are: 1) stretching via hydrodynamic forces; 2) stretching via confinement induced forces.

In recent reports, chips have been designed to hydrodynamically stretch a DNA molecule as it enters a detection region [35, 40]. When a pressure gradient is applied, the channel geometry near the region of interest induces a non-uniform sheer flow, which stretches DNA molecules. Due to high flow speeds through the microchannel, many molecules may be detected per unit time. Obtaining large a number of single molecule measurements combines the unique information gained by interrogating molecules on an individual basis, with the statistics of an ensemble average. Such a

setup has been used to rapidly map the position of fluorescently labeled probes on long DNA molecules [35, 40].

In 2006, Schwartz et al. presented a novel approach to optical mapping using nanoslit devices [61]. In the report, DNA molecules were elongated using $100\,nm$ deep nanoslit devices filled with low ionic strength solution which increased the degree of stretching. Specific sites on the DNA strands were marked prior to insertion in the nanoslit by using using a complementary enzymatic labeling scheme. A new class of endonucleases was used to nick, but not cleave, double stranded molecules at specific sites. Nick translation of DNA molecules in bulk solution using fluorochrome-labeled nucleotides followed by counterstaining of DNA backbones with the bis-intercalator YoYo-1 resulted in molecules for which the backbone appeared as one color, and the modified restriction sites as another color. The pre-processed molecules were then elongated in the nanoslit device and imaged used fluorescence microscopy. The YoYo-1 dye and the nick translated fluorochrome emitted at different wavelengths but could be excited with a single laser. The experiments resulted in optical barcode maps which could be used for any number of purposes (See Section 1.2).

1.4.3 Nanopillar Arrays

The earliest nanofluidic devices employed channels which contained arrays of nanoscale pillars. The devices were designed to be used as sieving matrices for separation of DNA molecules according to length. It was hoped that precise control of pillar geometry and spacing would lead to greater separation performance as compared with traditional polymer matrices. In articles by Cabodi [27] and Austin [2-4] several variations of pillar devices were tested. It was shown that large DNA molecule

separation could be achieved, although single base pair resolution was not demonstrated.

Often, for molecular diagnostic purposes, it is desirable to use a separation process as a purification step with the idea that the separation molecules will be isolated and used for a variety of purposes. In order to separate nucleic acids and proteins by size for preparative purposes, most often gel filtration chromatography or gel electrophoresis is used. Though these methods are popular for sample preparation, they are not ideal. The disadvantages are that gel filtration chromatography has poor resolution, and that sample recovery following gel electrophoresis is difficult. The nanofabricated separation devices mentioned have resulted in greatly improved separation speed and resolution as compared to gels, however, due to small initial plug sizes in the channels, throughput is extremely low. The solution to this may lie in continuous mode separation, which has been demonstrated in a variety of nanofluidic devices.

Initially it was shown that an asymmetric "Brownian-ratchet" based devices could be used to separate long DNA molecules in a continuous mode [63, 64]. In the presence of an electric field and no sieving matrix, DNA molecules of different sizes migrate at the same velocity. However, as they migrate, they also diffuse at a size dependent rate. An initially tight band of small molecules, driven through free solution, spreads out to a greater degree than an equally initially tight band of large molecules, since the small ones diffuse faster. Austin et. al showed that a lattice of asymmetric obstacles can rectify the Brownian motion of the molecules. Thus, instead of the band of small molecules simply becoming more disperse, it is deflected to one side as it's driven down the obstacle course. DNA molecules of different sizes, or any other analytes

with a range of diffusivities can be separated in a continuous fashion as they are driven down the Brownian ratchet array [65].

Pillar arrays were also shown to effect separation using a novel pulsed gel procedure called “entropic recoil” [66]. Entropic recoil occurs when molecules are positioned so that they straddle the interface between a microchannel and nanopillar populated region. Through thermally induced motion, the segment of the DNA strand straddling the interface tests the volume of configuration space available to it in the microchannel versus nanopillar regions. The difference in available configuration volume between the two regions corresponds to a difference in entropy. Finally, the entropic difference results in a free energy gradient and thus a force, which pulls the molecule out of the pillar array [67].

This entropic recoil effect is significant for two reasons. First, it presents a means for directly measuring a confinement induced force. Such measurements can be used to corroborate models of polymer theory. Second, it can be employed in the separation of molecules by size. A procedure for doing this was developed by Turner et. al and is illustrated in Figure 1 below.

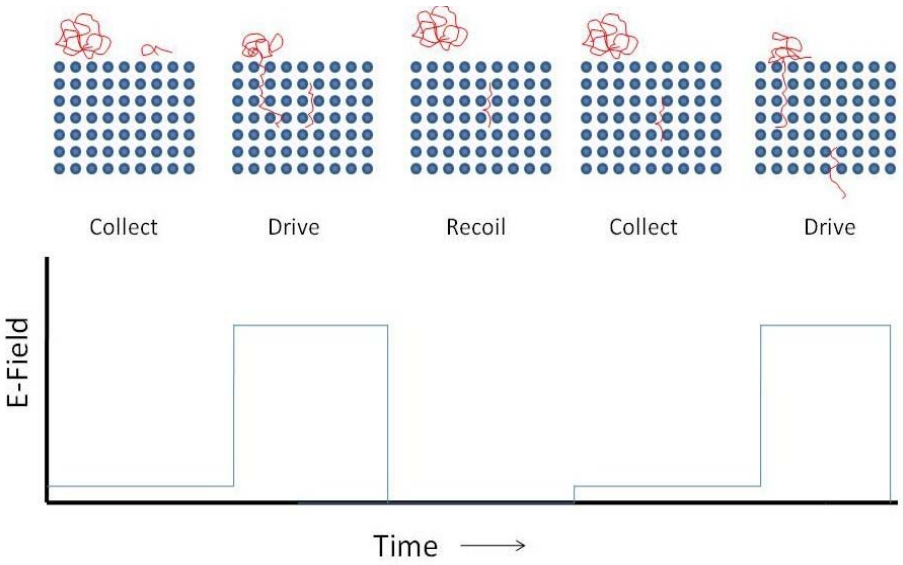

Figure 1. Phases of entropic recoil separation procedure. **Collect)** A sub-threshold voltage is applied which causes the DNA molecules to migrate to the entrance of the nanopillar array, but which is not large enough to drive them into the array. **Drive)** a larger voltage is applied, driving the collected molecules into the array, either partly or entirely, depending on their length. **Recoil)** The electric field is switched off. Short, fully inserted molecules remain in the nanopillar array. Longer molecules, which straddle the interface between the pillar region and the microchannel region experience an entropically induced force, which causes them to recoil into the microchannel. The three phases are repeated until separation of two populations is achieved.

1.4.4 Entropic Trap Arrays

The entropic trap array consists of alternating deep and shallow regions in series as part of a microfabricated, fluid-filled channel [5-8]. DNA molecules are forced to

change conformation as they travel through the alternating deep and shallow regions. Because the internal conformation change costs entropic free energy, they are temporarily trapped at the entrance to a thin region. A molecule in the deep region diffuses, when a sufficient number of DNA monomers happen to move into the high field region near the slit entrance, the molecule's escape from that trap is initiated. Interestingly, longer DNA molecules have a higher probability of escaping due to the fact that they have more surface area in contact with the high field region. This effect, higher mobilities for larger molecules, is being studied in great detail by a number of groups and ways in which it can be optimally used in an integrated system are being investigated. In its first design the entropic trap array was particularly well suited for separation of DNA molecules of length 10's of kbp and greater. This is a size range of considerable practical importance, since it is difficult to separate any molecules greater than around 40 kbp in a gel without the use of a pulsed field approach.

While the relative size of the thin slit and the DNA's radius of gyration are important, another critical parameter in entropic trap array separation efficiency is the spacing between subsequent traps. As DNA molecules exit one narrow gap, travel through the deep region, and approach the next narrow gap, they must have sufficient time to relax to their equilibrium conformation in each deep region before encountering the next thin slit. It has been shown that even at high fields and trap spacing on the order of microns, the molecules still have sufficient time to relax, a fact which allows the field to be applied in a DC mode. Note that this is in contrast to pulsed field gel electrophoresis where DNA relaxation is achieved by temporarily turning off, or switching the direction of the electric field.

In the spirit of continuous flow separation, Han et. al has adapted the entropic trap device by creating a two dimensional periodic nanofilter array [9, 10, 26]. Deep nanochannels (~330 nm) run longitudinally and shallow (~50 nm) channels run laterally. Additionally, two perpendicular components of the applied electric field can be independently controlled. The structural anisotropy leads to different trajectories for different-sized or charged biomolecules.

This anisotropic nanofilter array (ANA) allows for three Sieving mechanisms to be used (Ogston sieving, entropic trapping, and electrostatics sieving.) In Ogston sieving, the mobility of different sized molecules is solely determined by the configurational or conformational entropy loss within the constrictions due to steric exclusion. For macromolecules with diameters larger than the constriction size, molecules must deform to pass, a process known as entropic trapping and described above. Mobility through the array is therefore determined by the entrance attempt frequency which varies significantly with polymer length. Finally the devices can also be used in an electrostatic sieving mode. In this mode, repulsive or attractive interaction between charged analyte molecules and the electric potential in the nanoconstriction determine the probability of a molecule entering that constriction, and thus the mobility through the array.

1.4.5 Nanochannels for DNA Analysis and Polymer Theory

It was previously mentioned that DNA molecules confined to nanoslits change their conformation by flattening in the vertical dimension and bulging in the other two spatial dimensions. Similarly, the conformation of a molecule is greatly altered when it enters a nanochannel. A nanochannel confines the molecule in two dimensions and allows it to expand in the third dimension only (i.e. the direction of the nanochannel

axis) . The theory describing this confinement induced expansion is covered in detail in Chapter 2, but here we say a few brief words about the basic characteristics of the theory and its applications.

Since as early as 2002, researchers have been using observation of fluorescently labeled DNA molecules in nanochannels for technological applications. Cao et al created 10nm wide channels for DNA analysis [68] and gradient structures for loading DNA into nanochannels from microchannels [69]. Tegenfeldt et al. showed that a genomic length molecule could be stretched and its observed length used to infer the total contour length of the molecule [70]. As a proof of principle, $\lambda - phage$ DNA concatemers were imaged in $100nm$ diameter channels and analyzed. Given just twenty statistically independent measurements, or one minute of observation, the extension length of a λ monomer could be measured to an accuracy of $\pm 0.15\mu m$, or $\pm 400bp$.

The method for measuring fragment length compares well with the pulsed field gel technique. For electrophoretic separations in gels, there is a loss of resolution at high molecular weights because of the nonlinear decrease of mobility with increasing molecule length. However, for single molecules measurements of fluctuating molecules, by collecting enough photons, fragment length can be determined to arbitrary precision. This concept is developed fully in Chapter 2.

As was mentioned in section 1.4, it is also possible to determine the contour length of a fluorescently stained DNA molecule simply by measuring its fluorescence intensity. What, then, is the advantage of performing length measurements on elongated molecules in channel? In fact if the goal is length measurement on its own, then there

is no advantage to using nanochannels. Nanochannels can only provide increased utility when length measurements are combined with additional measurements, performed simultaneously on the molecule, in which the information obtained is sensitive to preservation of the order of bases along the direction of elongation. Several examples of this follow.

In 2005 Rhein et. al demonstrated real time observation of enzymatic digestion of an elongated DNA molecule in a channel [23]. Briefly, a nanofluidic channel was filled with buffer and restriction enzymes known to cut the DNA strand at two locations. A chemical gradient of magnesium ions was also set up across the channel. Because magnesium ions are required for proper functioning of the restriction enzyme, a DNA molecule could only be cleaved once it reached the part of the nanochannel where the Mg2+ concentration was sufficient. DNA molecules were driven into nanochannels, were allowed to rest in the channel, and were observed to break into several pieces over a period of tens of seconds. Confinement of the fragments in a nanochannel resulted in an elongated length that was linearly dependent on contour length. It also resulted in highly suppressed center of mass diffusion. Thus, immediately after the molecule broke into fragments, both the size and order of each fragment could be determined. In this first example, as in the next two, we see that the ability of a nanochannel to both elongate a molecule and preserve the order of the monomers in space is the reason for its technological utility.

The essential function of a restriction digest assay is to identify and localize a finite number of sequence motifs in a larger DNA sequence. This is due to the fact that each restriction enzyme cuts only after recognizing specific sequences and is sensitive even to single base mutations. But localizing motifs along a sequence can also be achieved

by other methods, as mentioned in the discussion in Section 1.4.3, on optical mapping in nanoslits. The complementary enzymatic labeling scheme of Schwartz et al. is a convenient method, although target motifs are limited to sites which can be recognized by a special class of restriction enzymes. Another technique, employed by U.S. Genomics company [35, 40], is to hybridize fluorescently tagged oligomer probes or PNA molecules, either of which can be designed to target a motif of an arbitrary sequence. While neither labeling technique has yet been demonstrated in nanochannels, both should be possible, in principle. The main advantage of nanochannels would be to improve the elongation and detection methods.

Although the U.S Genomics experiments showed that hydrodynamic elongation can be employed to linearize and detect individual molecules for gene mapping, there are several aspects of this method which likely limit its resolution and sensitivity. Here we explain why confinement induced stretching in nanochannels offers a path around such measurement limitations. Figure 2 illustrates the difference in geometry between devices used for hydrodynamic elongation versus those used for confinement induced elongation.

To begin with, DNA molecules that are stretched by confinement in a nanofluidic channel are observed to elongate in an extremely uniform manner, while hydrodynamically stretched polymers adopt a “flower and stem” configuration (2). This uneven degree of elongation may introduce complications during genomic mapping analysis.

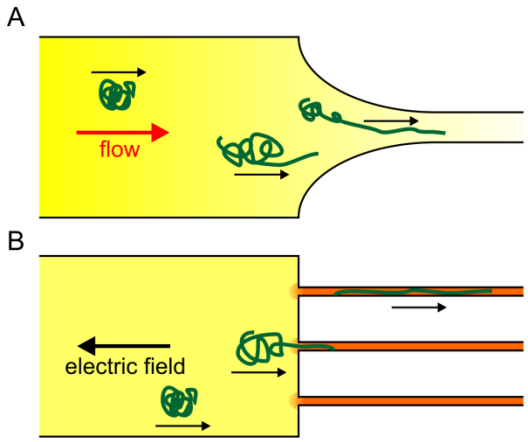

Figure 2. Comparison between **(A)** hydrodynamic stretching a microfluidic device, and **(B)** confinement induced stretching in a nanofluidic device. Red arrow indicates direction of fluid flow, large black arrow indicated direction of electric field, and small black arrows indication direction of DNA motion

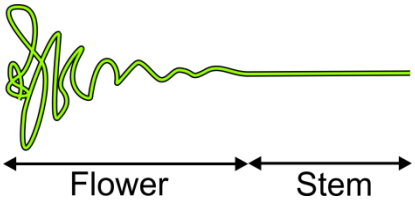

Figure 3. Flower and Stem Model of polymer in a fluid flow. In polymer strands in fluid flow with high velocities tension is believed to increase along the strand leading to an inhomogeneous stretching. The stretched out part is called "stem" while the trumpet-like end is called "flower". This behavior which was originally observed for tethered DNA. (2)

Secondly, using hydrodynamic forces, it is possible to stretch a molecule to about 80% if its full contour length, but extremely difficult to achieve higher degrees of elongation.(2) For DNA molecules in nanochannels, 80% stretching has also been

observed, and higher degrees of elongation are expected as channel dimensions continue to shrink.

Confinement induced elongation also acts on each molecule in an extremely reliable and consistent way. For hydrodynamic stretching, the elongation factor may depend on where and how the molecule enters the region of non-uniform sheer flow [35, 40]. The result of this is that many molecules passing through the illumination volume do so in a minimally stretched state.

Finally, effective hydrodynamic stretching requires that flow speeds be greater than a certain threshold value to obtain a significant degree of elongation. Further increasing the flow speed only minimally increases the stretching factor. While it is true that high flow speeds permit more molecules to be detected per unit time, the number of photons collected from each molecule decreases linearly with a decrease in exposure time. The tradeoff between single molecule resolution and frequency of events must be considered. It is clearly desirable to have flexibility with flow speed in order to find the optimal operating conditions. Stretching by nanochannel confinement works at zero velocity as well as at very high flow speeds.

For these reasons, there is motivation to improve nanochannel procedures for DNA elongation. In line with this goal, work has been done in the Craighead group on rapid fragment sizing using various DNA flow speeds through a nanochannel. In an article by Reccius et al. it was reported that a molecular length resolution of 114nm could be achieved with a measurement time of 20ms per molecule [71]. Various aspects of the contour and dynamics of DNA molecules were also investigated in detail as the molecules passed through the channels.

In addition to the technological justification for studying DNA in nanochannels, there is theoretical motivation. Nanochannel experiments provide a means for testing polymer theory in ways that were previously not possible. Here are several examples.

The report by Tegenfeldt, described in the beginning of this subsection, demonstrated a method of single molecule fragment sizing. In order to perform analysis using that method, a number of concepts from polymer theory were applied, the details of which are described fully in Chapter 2. In brief, it was shown that fundamental characteristics of confined flexible polymers, such as molecular width and persistence length (a characterization of backbone flexibility), are responsible for statistical mechanical properties such as extension factor, spring constant and relaxation time. The analysis was based on Pierre deGennes' "blob" model, which is valid as long as the diameter of the channel is much larger than the persistence length of the molecule. Since the persistence length of double stranded DNA is on the order of $50nm$, this condition is just barely met for the 100nm channels investigated in the Tegenfeldt report. The data was described very well by the model, lending support to deGennes' decades old theoretical description of self avoiding polymers in cylindrical confinement.

If channels with much smaller diameters are used, deGennes' model begins to break down and an entirely different mathematical description is required. Evidence supporting this model, attributed to Odijk, was made available with the experiment of Reisner et. al, in which the dynamics of double stranded DNA in channels with diameters as small as $35nm$ was investigated [72]. While we do not go into the details

of the Odijk model in this thesis, the interested reader is referred to a number of articles on the topic [62, 73].

In addition to testing DNA in nanochannels of various diameters, intrinsic properties of the molecule itself, such as persistence length and effective DNA width, may be adjusted and their affect on polymer dynamics can be determined. This was shown recently in an article by Reisner, in which buffer solutions of various ionic strengths were used as a knob to adjust intrinsic molecular properties [74]. The effect of ionic strength on DNA extension in a channel is quite dramatic. In addition to its technological applications, the result has received attention in the polymer physics community, reigniting the debate between applicability of the deGennes' and Odijk models.

The experiments just mentioned, probed the dynamics of DNA molecules in nanochannels, caused by thermal fluctuations about an equilibrium state. In contrast, there have been several investigations of DNA dynamics resulting from a particular initial conformation or position that is not an equilibrium state of the molecule. Following Turner's description of entropic recoil from pillar arrays, the same recoil process was observed to occur for molecules partly inserted into nanochannels. Molecules recoiling from nanochannels were easier to track and analyze, due to the fact that the portion of a molecule in the low entropy region was confined to a straight channel, as opposed an array of posts where it could zigzag through space. Analysis led to the discovery an additional dynamic process termed "contraction" and a modification to the recoil theory. This is elaborated upon further in Chapter 4.

In 2005 Reccius et. al reported an investigation of the dynamical properties of highly compressed DNA molecules in nanochannels [75]. In the experiment, constrictions were created inside of nanochannels, such that a molecule travelling through the channel could not easily pass. It would compress up against the constriction, and when the driving force was switched off, it would slowly decompress to its equilibrium comformation in the nanochannel. This is an interesting experiment from a polymer physics point of view. Many biophysical questions involve DNA compression such as DNA packaging in bacteriophage heads, as mentioned earlier, or winding of DNA into tightly packed coils in the nucleus. However, long DNA molecules such as λ-phage DNA form micron size spherical coils in free solution, which are difficult to resolve in detail with optical microscopy. Consequently, previous quantitative studies had been restricted to investigating elongated DNA. Because confining DNA in nanochannels increases its equilibrium dimensions in one dimension, it enabled optical investigation of this previously unreachable regime of compression and ensuing expansion.

More recently, a single molecule, fluorescence video microscopy experiment was performed by the Craighead group demonstrating the spontaneous unfolding of initially folded DNA molecules in nanochannels. This experiment provides evidence for the theory by Jun and Arnold, which describes entropically induced segregation of overlapping segments of a DNA molecule in a nanochannel Although some differences were found between simulation and experiment, the result definitively shows the existence of an entropically induced force causing resisting the overlap of topologically distinct molecular segments. This report is described in more detail later, as the article is presented verbatim in Chapter 5.

1.5 Chapter Summaries

Here we give brief summaries of the remaining Chapters in this thesis, and, where appropriate, describe the way in which a chapter relates to the others. Chapter 2 lays the conceptual groundwork for understanding the behavior of single DNA molecules confined to nanofluidic channels. Initially, the structure and properties of DNA molecules in free solution are reviewed. While the chemical composition of DNA is important to its biological function, emphasis is placed on understanding the mechanical properties, which are critical in determining DNA configuration and dynamics in solution. The mechanics are explained in terms of theories for self-avoiding linear polymers, originally developed by Flory, deGennes and others. For randomly coiled DNA molecules in free solution, we review scaling laws for the mean coil radius, and the entropic spring like forces which resist expansion or compression of the sphere. This is done both for an ideal polymer, and a real polymer in aqueous solvent.

Next, a brief review of important concepts in the field of micro- and nano-fluidics is given. It is shown that interactions between channel walls and electrolyte solutions result in both bound surface charge and an accumulation of mobile charges near the wall surfaces. An understanding these effects is required for proper interpretation of observed DNA conformation and dynamics. Of those effects reviewed is the dependence of zeta potential and Debye screening length on ionic strength. Particular consideration is given to the limiting cases of both high and low ionic strengths. High ionic strength conditions are pertinent to the experiments described in Chapters 3, 4, and 5, in which the conformation and dynamics of DNA molecules in $100\,nm$ X $100\,nm$ cross sectional channels are studied. Low ionic strength conditions, on the

other hand, are relevant for the device described in Chapters 6 and 7, constructed with the objective of electrically detecting single DNA molecules.

For the final part of Chapter 2, having established a basic model for DNA in free solution and an understanding of the chemical and physical environment inside of a nanochannel, the behavior of highly confined single DNA molecules is reviewed using a combination of theoretical models and published experimental results. The deGennes' blob model is derived for linear polyelectrolytes in cylindrical confinement. This model enables the calculation of end to end extension length along the direction of the channel axis, fluctuations about the mean extension, spring-like forces resisting extension and compression, expressions for hydrodynamics friction of the confined polymers, and from this, calculated relaxation times for polymers whose end to end distance is transiently perturbed about its equilibrium length. In all cases, emphasis is placed on scaling with channel diameter and molecular properties such as persistence length and contour length.

Chapter 3 is a published review on the use of nanofabricated, fluid filled cavities for manipulation and detection of single biomolecules. The article was written for a special issue of the journal Biopolymers with a focus on modern, single molecule microscopy. The focus of the paper is on two separate effects that depend on dimensional relations. The first is the relationship between nanofluidic channel length scales and the length scale associated with a diffraction-limited, focused beam of light. It is shown that, using structures which are smaller in size than the spatial resolution afforded by the diffraction limit, one is able to tailor the size and shape of the optical probe (the illuminated volume of fluid) in a way that was previously challenging or impossible. The second dimensional relation explored is a comparison between

nanofluidic cavity length scales and length scales associated with single biological macromolecules, such as DNA. Due to the fact that nanocavities can be made with critical dimensions smaller than the radius of gyration for long DNA molecules in free solution, one can use the structures to manipulate the conformation and dynamics of the molecules in ways that were previously not possible. Such manipulation allows for new methods of obtaining information about a particular DNA molecule's biological or mechanical properties

Chapter 4 is a published article on dynamics of single DNA molecules in nanochannels. In this article, entropic recoil from nanochannels is investigated for the first time. In addition to the recoil motion, a new type of motion is observed for molecules after they enter a nanochannel at high velocity and are then stopped in the channel. During the entrance event, the spring-like molecules are stretched beyond their equilibrium extension length. If the driving force is subsequently switched off, the molecule will remain in the channel and will slowly contract to its equilibrium length. That equilibrium length is dictated by the channel diameter and molecular properties. Contraction of a hyperextended molecule in a channel may also occur while a molecule is undergoing the recoil process, given the appropriate starting conditions. Decoupling these two types of motion is critical for proper analysis of the forces exerted on the confined polymer.

During analysis of recoil data, it was observed that on rare occasions molecules were driven into a channel in such a way that some middle portion of the molecule enters first, creating a folded front end. In such cases, the recoil force could be used to pull on the longer end alone, causing the molecule to unfold. Initial observations of folded molecules at rest in a channel, and not perturbed by the recoil force, revealed that

spontaneous unfolding did not occur over a short timescale. Later, however, by extending the duration of measurement, spontaneous unfolding was observed. Chapter 5 is a recently published article describing experiments in which this spontaneous unfolding process is analyzed and a theory describing the driving force is proposed.

Chapter 6 is a paper in progress. It describes the concept of a device in which nanofluidic channels with integrated carbon nanotubes is constructed for electrical detection of single DNA molecules. Chapter 7 is a description of the fabrication process of this device. It includes discussion of various fabrication restrictions that result from anticipated device requirements. Chapter 8 includes concluding remarks and discussion of a number of possible future projects. Finally, Appendix A shows calculations from Chapter 2 for determining the full chemical equilibria in a nanofluidic channel given a variety of buffer concentrations, and Appendix B gives step by step instructions for fabricating the electrical detection devices.

1.6 Conclusion

Nanofludic channels have utility as tools for the investigation of polymer theory, and as technological devices. For testing polymer theory, the high degree of confinement imposed on DNA molecules, and ease of observation using fluorescence video microscopy permit convenient and novel experiments. Due to the similar size of nanochannels to some biological structures such as cellular nuclei and viral capsids, nanochannel experiments help to answer fundamental questions in biology.

For developing new technologies, the ability of nanochannels to assist in performing single molecule fragment length measurements makes them an important tool. The

true advantage of nanochannels, is that while enabling measurement of the end to end length of a molecule they also preserve the order of bases and allow for a range of other features to be probed and mapped along the molecule. In this thesis, one of our goals is to describe the physics involved with elongating, manipulating and observing molecules in nanochannels. In the course of doing so, we discuss the fundamental limits of the technology for acquiring sequence specific information, and outline current avenues of investigation for building the next generation of devices.

REFERENCES

1. Austin, R.H., et al., *Ratchets: the problems with boundary conditions in insulating fluids.* Applied Physics a-Materials Science & Processing, 2002. **75**(2): p. 279-284.
2. Bakajin, O., et al., *Fractionation of long DNA molecules in microfabricated arrays.* Biophysical Journal, 2000. **78**(1): p. 266A-266A.
3. Bakajin, O., et al., *Fractionation of chromosomal size DNA in microfabricated arrays.* Biophysical Journal, 1999. **76**(1): p. A398-A398.
4. Bakajin, O., et al., *Separation of 100-kilobase DNA molecules in 10 seconds.* Analytical Chemistry, 2001. **73**(24): p. 6053-6056.
5. Han, J. and H.G. Craighead, *Entropic trapping and sieving of long DNA molecules in a nanofluidic channel.* Journal of Vacuum Science & Technology a-Vacuum Surfaces and Films, 1999. **17**(4): p. 2142-2147.
6. Han, J. and H.G. Craighead, *Separation of long DNA molecules in a microfabricated entropic trap array.* Science, 2000. **288**(5468): p. 1026-1029.
7. Han, J., S.W. Turner, and H.G. Craighead, *Entropic trapping and escape of long DNA molecules at submicron size constriction.* Physical Review Letters, 1999. **83**(8): p. 1688-1691.
8. Han, J.Y. and H.G. Craighead, *Characterization and optimization of an entropic trap for DNA separation.* Analytical Chemistry, 2002. **74**(2): p. 394-401.
9. Fu, J.P., P. Mao, and J. Han, *Artificial molecular sieves and filters: a new paradigm for biomolecule separation.* Trends in Biotechnology, 2008. **26**(6): p. 311-320.

10. Fu, J.P., J. Yoo, and J.Y. Han, *Molecular sieving in periodic free-energy landscapes created by patterned nanofilter arrays.* Physical Review Letters, 2006. **97**(1).
11. Storm, A.J., et al., *Fabrication of solid-state nanopores with single-nanometre precision.* Nature Materials, 2003. **2**(8): p. 537-540.
12. Storm, A.J., et al., *Translocation of double-strand DNA through a silicon oxide nanopore.* Physical Review E, 2005. **71**(5).
13. Storm, A.J., et al., *Fast DNA translocation through a solid-state nanopore.* Nano Letters, 2005. **5**(7): p. 1193-1197.
14. McAlpine, M.C., et al., *Highly ordered nanowire arrays on plastic substrates for ultrasensitive flexible chemical sensors.* Nature Materials, 2007. **6**(5): p. 379-384.
15. Zheng, G., F. Patolsky, and C.M. Lieber, *Large-scale, multiplexed electrical detection of proteins and viruses by ultrasensitive nanowire sensor arrays.* Abstracts of Papers American Chemical Society, 2005. **230**: p. U306-U307.
16. Zheng, G., F. Patolsky, and C.M. Lieber, *Nanowire biosensors: A tool for medicine and life science.* Nanomedicine-Nanotechnology Biology and Medicine, 2006. **2**(4): p. 277.
17. Zheng, G.F., et al., *Multiplexed electrical detection of cancer markers with nanowire sensor arrays.* Nature Biotechnology, 2005. **23**(10): p. 1294-1301.
18. Zheng, G.F., F. Patolsky, and C.M. Lieber, *Large-scale, multiplexed electrical detection of proteins and viruses by ultrasensitive nanowire sensor arrays.* Abstracts of Papers of the American Chemical Society, 2005. **230**: p. U306-U307.
19. Zheng, G.F., F. Patolsky, and C.M. Lieber, *General and powerful platform for large-scale, label-free, parallel electrical detection of biomolecules by*

ultrasensitive nanowire transistor arrays. Abstracts of Papers of the American Chemical Society, 2006. **231**.

20. Foquet, M., et al., *DNA fragment sizing by single molecule detection in submicrometer-sized closed fluidic channels.* Analytical Chemistry, 2002. **74**(6): p. 1415-1422.
21. Liang, X.G., et al., *Single sub-20 nm wide, centimeter-long nanofluidic channel fabricated by novel nanoimprint Mold fabrication and direct imprinting.* Nano Letters, 2007. **7**: p. 3774-3780.
22. Riehn, R., R.H. Austin, and J.C. Sturm, *A nanofluidic railroad switch for DNA.* Nano Letters, 2006. **6**(9): p. 1973-1976.
23. Riehn, R., et al., *Restriction mapping in nanofluidic devices.* Proceedings of the National Academy of Sciences of the United States of America, 2005. **102**(29): p. 10012-10016.
24. Inglis, D.W., et al., *Determining blood cell size using microfluidic hydrodynamics.* Journal of Immunological Methods, 2008. **329**: p. 151-156.
25. Dittrich, P.S. and P. Schwille, *An integrated microfluidic system for reaction, high-sensitivity detection, and sorting of fluorescent cells and particles.* Analytical Chemistry, 2003. **75**(21): p. 5767-5774.
26. Han, J.Y., J.P. Fu, and R.B. Schoch, *Molecular sieving using nanofilters: Past, present and future.* Lab on a Chip, 2008. **8**(1): p. 23-33.
27. Cabodi, M., et al., *Continuous separation of biomolecules by the laterally asymmetric diffusion array with out-of-plane sample injection.* Electrophoresis, 2002. **23**(20): p. 3496-3503.
28. Craighead, H., *Future lab-on-a-chip technologies for interrogating individual molecules.* Nature, 2006. **442**: p. 387-393.

29. Brochard, F. and P.G. Degennes, *DYNAMICS OF CONFINED POLYMER-CHAINS.* Journal of Chemical Physics, 1977. **67**(1): p. 52-56.

30. Daoud, M. and P.G. Degennes, *STATISTICS OF MACROMOLECULAR SOLUTIONS TRAPPED IN SMALL PORES.* Journal De Physique, 1977. **38**(1): p. 85-93.

31. Clayton, J., *Go with the microflow.* Nature Methods, 2005. **2**(8): p. 621-627.

32. Janasek, D., J. Franzke, and A. Manz, *Scaling and the design of miniaturized chemical-analysis systems.* Nature, 2006. **442**(7101): p. 374-380.

33. Yager, P., et al., *Microfluidic diagnostic technologies for global public health.* Nature, 2006. **442**(7101): p. 412-418.

34. Chan, E.Y., et al., *DNA mapping technology based on microfluidic stretching and single-molecule detection of motif tags.* Biophysical Journal, 2003. **84**(2): p. 302A-302A.

35. Chan, E.Y., et al., *DNA mapping using microfluidic stretching and single-molecule detection of fluorescent site-specific tags.* Genome Research, 2004. **14**(6): p. 1137-1146.

36. Foquet, M., et al., *Improved fabrication of zero-mode waveguides for single-molecule detection.* Journal of Applied Physics, 2008. **103**(3).

37. Korlach, J., et al., *Selective aluminum passivation for targeted immobilization of single DNA polymerase molecules in zero-mode waveguide nanostructures.* Proceedings of the National Academy of Sciences of the United States of America, 2008. **105**: p. 1176-1181.

38. Larson, J.W., et al., *Single DNA molecule stretching in sudden mixed shear and elongational microflows.* Lab on a Chip, 2006. **6**: p. 1187-1199.

39. Lundquist, P.M., et al., *Parallel confocal detection of single molecules in real time.* Optics Letters, 2008. **33**(9): p. 1026-1028.

40. Phillips, K.M., et al., *Application of single molecule technology to rapidly map long DNA and study the conformation of stretched DNA.* Nucleic Acids Research, 2005. **33**(18): p. 5829-5837.
41. Smith, D.E., et al., *The bacteriophage phi 29 portal motor can package DNA against a large internal force.* Nature, 2001. **413**(6857): p. 748-752.
42. Jun, S. and B. Mulder, *Entropy-driven spatial organization of highly confined polymers: Lessons for the bacterial chromosome.* Proceedings of the National Academy of Sciences of the United States of America, 2006. **103**(33): p. 12388-12393.
43. Arnold, A. and S. Jun, *Time scale of entropic segregation of flexible polymers in confinement: Implications for chromosome segregation in filamentous bacteria.* Physical Review E, 2007. **76**.
44. Moffitt, J.R., et al., *Recent advances in optical tweezers.* Annual Review of Biochemistry, 2008. **77**: p. 205-228.
45. Smith, S.B., L. Finzi, and C. Bustamante, *DIRECT MECHANICAL MEASUREMENTS OF THE ELASTICITY OF SINGLE DNA-MOLECULES BY USING MAGNETIC BEADS.* Science, 1992. **258**(5085): p. 1122-1126.
46. Perkins, T.T., D.E. Smith, and S. Chu, *Single polymer dynamics in an elongational flow.* Science, 1997. **276**(5321): p. 2016-2021.
47. Bird, R.B., *NON-NEWTONIAN BEHAVIOR OF POLYMERIC LIQUIDS.* Physica A, 1983. **118**(1-3): p. 3-16.
48. Bakajin, O.B., et al., *Electrohydrodynamic stretching of DNA in confined environments.* Physical Review Letters, 1998. **80**(12): p. 2737-2740.
49. Balducci, A., et al., *Double-stranded DNA diffusion in slitlike nanochannels.* Macromolecules, 2006. **39**: p. 6273-6281.

50. Hsieh, C.C., A. Balducci, and P.S. Doyle, *An experimental study of DNA rotational relaxation time in nanoslits.* Macromolecules, 2007. **40**: p. 5196-5205.

51. Randall, G.C. and P.S. Doyle, *DNA deformation in electric fields: DNA driven past a cylindrical obstruction.* Macromolecules, 2005. **38**(6): p. 2410-2418.

52. Randall, G.C. and P.S. Doyle, *Collision of a DNA polymer with a small obstacle.* Macromolecules, 2006. **39**(22): p. 7734-7745.

53. Stigter, D., *Wall effects on DNA stretch and relaxation.* Biophysical Chemistry, 2002. **101**: p. 447-459.

54. Woo, N.J., E.S.G. Shaqfeh, and B. Khomami, *Effect of confinement on dynamics and rheology of dilute DNA solutions. I. Entropic spring force under confinement and a numerical algorithm.* Journal of Rheology, 2004. **48**(2): p. 281-298.

55. Woo, N.J., E.S.G. Shaqfeh, and B. Khomami, *The effect of confinement on dynamics and rheology of dilute deoxyribose nucleic acid solutions. II. Effective rheology and single chain dynamics.* Journal of Rheology, 2004. **48**(2): p. 299-318.

56. Hagita, K., S. Koseki, and H. Takano, *Relaxation of a polymer chain confined in a slit.* Journal of the Physical Society of Japan, 1999. **68**(6): p. 2144-2145.

57. Usta, O.B., A.J.C. Ladd, and J.E. Butler, *Lattice-Boltzmann simulations of the dynamics of polymer solutions in periodic and confined geometries.* Journal of Chemical Physics, 2005. **122**.

58. Strychalski, E. and S. Levy, Macromolecules, 2008. **In Press**.

59. Bonthuis, D., et al., PRL, 2008. **101**: p. 108303.

60. deGennes, P.-G., *Scaling Concepts in Polymer Physics*. 1979, Ithaca, NY: Cornell University Press.

61. Jo, K., et al., *A single-molecule barcoding system using nanoslits for DNA analysis.* Proceedings of the National Academy of Sciences of the United States of America, 2007. **104**(8): p. 2673-2678.

62. Odijk, T., *Scaling theory of DNA confined in nanochannels and nanoslits.* Physical Review E, 2008. **77**(6).

63. Chou, C.F., et al., *Sorting by diffusion: An asymmetric obstacle course for continuous molecular separation.* Proceedings of the National Academy of Sciences of the United States of America, 1999. **96**(24): p. 13762-13765.

64. Chou, C.F., et al., *Rectified Brownian motion: Continuous sorting of macromolecules in a microfabricated array.* Biophysical Journal, 1999. **76**(1): p. A399-A399.

65. Huang, L.R., et al., *Continuous particle separation through deterministic lateral displacement.* Science, 2004. **304**(5673): p. 987-990.

66. Cabodi, M., S.W.P. Turner, and H.G. Craighead, *Entropic recoil separation of long DNA molecules.* Analytical Chemistry, 2002. **74**(20): p. 5169-5174.

67. Turner, S.W.P., M. Cabodi, and H.G. Craighead, *Confinement-induced entropic recoil of single DNA molecules in a nanofluidic structure.* Physical Review Letters, 2002. **88**(12).

68. Cao, H., et al., *Fabrication of 10 nm enclosed nanofluidic channels.* Applied Physics Letters, 2002. **81**(1): p. 174-176.

69. Cao, H., et al., *Gradient nanostructures for interfacing microfluidics and nanofluidics.* Applied Physics Letters, 2002. **81**(16): p. 3058-3060.

70. Tegenfeldt, J.O., et al., *The dynamics of genomic-length DNA molecules in 100-nm channels.* Proceedings of the National Academy of Sciences of the United States of America, 2004. **101**(30): p. 10979-10983.

71. Reccius, C.H., et al., *Conformation, length, and speed measurements of electrodynamically stretched DNA in nanochannels.* Biophysical Journal, 2008. **95**(1): p. 273-286.

72. Reisner, W., et al., *Statics and dynamics of single DNA molecules confined in nanochannels.* Physical Review Letters, 2005. **94**(19).

73. Odijk, T., *DNA confined in nanochannels: Hairpin tightening by entropic depletion.* Journal of Chemical Physics, 2006. **125**(20).

74. Reisner, W., et al., *Nanoconfinement-enhanced conformational response of single DNA molecules to changes in ionic environment.* Physical Review Letters, 2007. **99**(5).

75. Reccius, C.H., et al., *Compression and free expansion of single DNA molecules in nanochannels.* Physical Review Letters, 2005. **95**(26).

CHAPTER 2
CONCEPTUAL FOUNDATIONS FOR DNA IN NANOCHANNELS

2.1 Introduction

Nanofluidic channel based devices can be used to elongate and observe DNA, enabling fragment length measurements on single molecules. By taking such measurements, sequence information can be inferred in a relatively short period of time. It is possible, for example, to identify eight fragment lengths in a mixture of λ bacteriophage DNA and its HindIII digest by individually interrogating a total of 15,000 molecules over a period of two minutes [1]. Using conventional gel electrophoresis techniques to perform the same measurement would take at least 30 times as long and would require orders of magnitude more sample. Furthermore, for identification of DNA molecules with lengths even greater than λ-DNA, pulsed gel electrophoresis is required. While typical pulsed gel times are on the order of 24 hours, the run time for a nanochannel device performing the equivalent of a pulsed gel measurement remains on the order of minutes.

This chapter is devoted to explaining the physics behind manipulation and observation of single DNA molecules in nanochannels, and ultimately to exploring the fundamental performance limiting factors. In order to do this, we take a somewhat circuitous, but necessary, route. We start by establishing a mathematical model for a DNA molecule in free solution. While this model is based on only a few simple assumptions, it predicts both the static conformations and the dynamics of unconstrained DNA reasonably well. Second, before discussing how the behavior of DNA changes when it is inserted into a nanochannel, we review the physics of electrolyte solutions inside nanoscale channels. A variety of electrokinetic effects

occur in nanoscale channels which, it turns out, can have a significant effect on DNA motion. In the final part of this chapter, we build upon the models for DNA in free solution, adapting them so that they can be used to describe molecules confined inside nanochannels. We learn that these models are widely used in the literature for performing analysis of nanochannel based DNA length measurements, and we use them to assist in determining the performance limiting factors of such a device.

2.2 Mathematical Models for DNA Molecules in Free Solution

2.2.1 Pertinent Chemical and Physical Features of Double Stranded DNA

The DNA molecules discussed in this thesis are long and flexible linear polymers which have unique chemical, mechanical and electronic properties. A cartoon of double stranded DNA (dsDNA) is shown in Figure 1a. Basic knowledge of DNA structure by the reader is assumed. Only a few of the essential features are mentioned here and for a more detailed description one can refer to any number of articles [2, 3]. Briefly, the dsDNA molecule is composed of two strands, each of which is built from a series of nucleic acid bases. In aqueous solution, the hydrophobic nitrogenous bases are found in the interior of a dsDNA molecule and the hydrophilic sugar phosphate backbone on the outer surface. The dsDNA has a cross sectional diameter of $2nm$ and a length which is proportional to the number of basepairs in the molecule. The contour length can be calculated by $L_C = (\#Basepairs) \times 0.34nm$, where $0.34nm$ is the inter-basepair spacing. The segment of DNA depicted in the cartoon is 27 base pairs in length.

While short pieces of DNA are stiff, the work presented in this thesis is concerned with very long molecules which should be viewed as highly flexible. A unit called the

persistence length, l_P, is defined as the distance between two points along the backbone over which the tangents of the backbone at those two points are uncorrelated. If the condition $L_C >> l_P$ is met, we consider the molecule to be flexible. For double stranded DNA $l_P \approx 50nm$, and the contour lengths of our investigated DNA molecules are in the range of $1-100\mu m$. This corresponds to a range of few kilobasepairs (kbp) to a few hundred kbp. Given that a $20\mu m$ DNA molecule has a length to width ratio of 10,000 to 1, it is easy to imagine why it is very flexible. In solution, such a molecule would look something like the cartoon in Figure 1b. The reason for this spherical conformation is not obvious, but the remainder of this section is devoted to statistical mechanical arguments which show from first principles why this is the case.

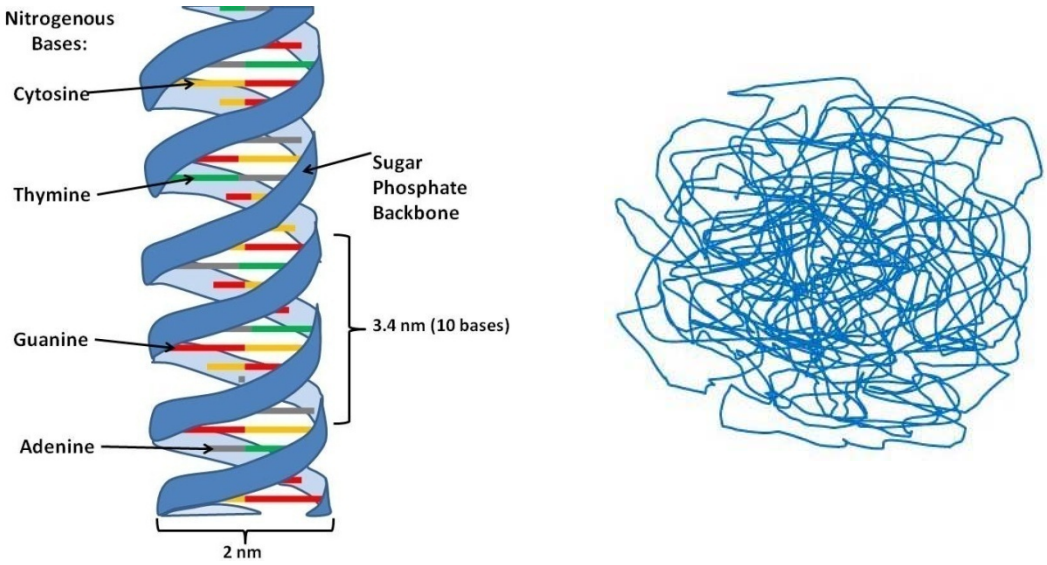

Figure 1 Cartoons of DNA molecules. **A)** Close up of a double stranded DNA molecule. At this level, properties such as the chemical composition of the backbone and the nitrogenous bases are visible. The width of the DNA, $2nm$, and the interbase spacing, $0.34nm$, can also be distinguished. On such a small scale DNA molecules appear relatively stiff. **B)** Depiction of a "long" ($L_C >> l_P$) DNA molecule in free solution. The molecule is most likely to assume some random, spherical conformation.

The mathematical models presented here have great utility, and so they are described in detail. Using the models, it is possible to predict many important characteristics of DNA in solution. For example the scaling of sphere size with contour length, the density of monomers at a given distance from the center, and the spring-like resistance to stretching or compression can all be calculated. In short, such models are needed in order to make sense of the behavior of long DNA molecules in free solution, and ultimately those confined to nanoscale channels.

2.2.2 Ideal Polymer Model (Random Walk on a Lattice)

As we have just seen, a DNA molecule has a relatively complicated chemical structure with the potential for interactions between neighboring and non-neighboring base pairs and some inherent stiffness. It is at first surprising, therefore, to learn that several models exist which account for none of these things, yet still do a reasonable job at predicting global properties of the polymer. We assume the DNA molecule can be modeled as a generic flexible polymer chain composed of a large number, N, of monomers each of length a with a contour length $L_C = N \cdot a$. It should be noted that in this model, the monomer length, a, is not equal to the spacing between basepairs. It is, rather, comparable to the persistence length.

In order to calculate statistical properties of the polymer, we begin by looking at a snapshot of the chain in some instant of time. For simplicity in developing the model, we imagine that such a chain sits on a two dimensional square lattice in some random configuration. Later we can extend the argument to three dimensions and to a lattice of arbitrary geometry. The lattice spacing is defined to be the same as the length of each monomer. In order to determine how the chain should be placed on this lattice we use a random walk approach [4]. Suppose that in placing the chain on this surface,

we place the end of the first monomer at the origin, and allow it to point in one of four directions, so that its other end touches one of the four nearest neighbor lattice points. For the next step in the random walk, monomer number two starts on the same lattice point as the end of monomer number one, and is also allowed to point in any one of four directions. Since this is an ideal chain model, it may even land back on the origin, ignoring the fact that in reality two monomers cannot overlap. We continue placing the remaining $N-2$ monomers on the lattice in this manner. When finished, the randomly generated conformation is said to begin at the origin and end at the position $\vec{R}$, where $\vec{R}=\sum_n \vec{a}_n$ and $\vec{a}_n$ is a vector of length a which represents the n^{th} step of the random walk. On a lattice of arbitrary geometry there are z nearest neighbors to each lattice point, and thus z possible steps for the polymer to take, each of which carries equal statistical weight (for the $2D$ square lattice, $z=4$). The total number of possible conformations for the chain on that lattice is given by the partition function, $Z=\sum_{\vec{R}}\Omega_N\left(\vec{R}\right)=z^N$, where $\Omega_N\left(\vec{R}\right)$ is the number of microstates corresponding to the observable $\vec{R}$.

We consider the vector, $\vec{R}$, which points from the origin to the last monomer, where, again, the origin is the location of the first monomer. We would like to determine the average distance between the first and last monomer. Clearly, the average value $\left\langle \vec{R} \right\rangle$ is zero, so we compute the mean square.

$$\vec{R}^2=\left\langle \vec{r}^{\,2}\right\rangle=\sum_{nm}\left\langle a_n\cdot a_m\right\rangle=\sum_n\left\langle a_n^{\,2}\right\rangle=Na^2 \qquad \text{Equation 1}$$

The $\vec{a}_n$ vectors are uncorrelated in their orientation, therefore in the calculation above, the sum of the cross products between different $\vec{a}_n$ is zero. The above expression holds for three dimensions as well as two. The probability distribution function for $\vec{R}$

can also be calculated. Derivations can be found in any standard treatment of the random walk [5], and here we just state the result. For the 3-D case,

$$P\left(\vec{R},N\right)=\left(\frac{3}{2\pi Na^2}\right)^{3/2}\exp\left(-\frac{3\vec{R}^2}{2Na^2}\right) \qquad \text{Equation 2}$$

Thus the probability distribution of $\vec{R}$ is a Gaussian about $\left\langle \vec{R} \right\rangle = 0$. From statistical mechanics, we know that in the canonical ensemble $P\left(\vec{R},N\right)=\Omega_N\left(\vec{R}\right)/\left(\sum_R \Omega_N\left(\vec{R}\right)\right)$. We rearrange this to obtain an expression for the number of microstates as a function of $\vec{R}$ for the polymer of constant monomer number N.

$$\Omega_N\left(\vec{R}\right)=\frac{P\left(\vec{R},N\right)}{\left(\sum_R \Omega_N\left(\vec{R}\right)\right)}=\left(\left(\frac{3}{2\pi Na^2}\right)^{3/2}\Big/\left(\sum_R \Omega_N\left(\vec{R}\right)\right)\right)\cdot\exp\left(-\frac{3\vec{R}^2}{2Na^2}\right) \qquad \text{Equation 3}$$

It is now possible to calculate the entropy as a function of $\vec{R}$ using the equation $S\left(\vec{R}\right)=-k_B\ln\left[\Omega\left(\vec{R}\right)\right]$. The result is

$$S\left(\vec{R}\right)=S(0)-\frac{k_B 3\vec{R}^2}{2Na^2} \qquad \text{Equation 4}$$

where the log of the prefactors have been absorbed into the constant $S(0)$. Given an expression for the entropy, we can calculate the conformational free energy of the polymer as a function of $\vec{R}$.

$$F(r)=F_I-TS(r)=F_I+\frac{3k_BT\cdot\vec{R}^2}{2Na^2} \qquad \text{Equation 5}$$

The elastic restoring force is the derivative of free energy with respect to end to end distance, R.

Here we make a comment regarding the calculated radius, and the radius measured by experiment. Besides calculating the end to end distance between the first and the last monomer, as is done above, it is also possible to define a quantity called the radius of gyration, R_G, where

$$R_G^2 = \frac{1}{2N^2}\sum_{n=1}^{N}\sum_{m=1}^{N}\left\langle \left(R_n - R_m\right)^2 \right\rangle \qquad \text{Equation 6}$$

This is the mean square of the separation distance between all possible pairs of monomers in the chain. Technically, the radius of gyration, and not the end to end distance, is most often measured directly by experiment. However, there is a simple relation between the two $\left\langle {R_G}^2 \right\rangle = \left\langle R^2 \right\rangle / 6$, as shown in [6]. For the purpose of evaluating basic scaling laws for isolated polymers we will continue to work with the mean square end to end distance $\left\langle R^2 \right\rangle$, but clearly it is easy to convert from one to the other.

2.2.3 Self-Avoiding Polymer Models

In reality, the ideal polymer model described above fails for DNA in an electrolyte solution. Experimental results for a real chain in aqueous solution indicate that radius of gyration does not scale in accordance with Equation **1**. Rather, $R \propto N^{y}$, where y is between 0.55 and 0.6 depending on the measurement technique used. The reason for this is that the ideal polymer model does not take into account volume exclusion (i.e. two monomers cannot exist in the same place at the same time).

While the mathematical properties of simple random walks are trivial, those of the self avoiding walk (SAW) are complex. Therefore we describe a shortcut for calculating the scaling of $\left\langle R^2 \right\rangle$ with molecular parameters such as N, v, and a. This clever derivation was first described by Flory.

We start with a chain in the conformation of sphere with an unknown radius, R, and an internal monomer concentration $c_{\text{int}} \cong N/R^3$. Due to monomer-monomer interactions, there is a repulsive energy in the chain given by $F_{rep} \cong k_B T \upsilon c_{\text{int}}^2 R^3 = k_B T \upsilon N^2/R^3$ where υ is the excluded volume parameter. This parameter roughly corresponds to the volume of space occupied by a monomer and we use an estimate of $\upsilon = wa^2$ as argued by [7]. The repulsive energy increases in magnitude for smaller R, thus accounting for the polymer's tendancy to swell as a result of excluded volume interactions. However, as R increases, the entropy of the chain decreases, resulting in an increase in the elastic free energy term of Equation **5**. The full conformational free energy expression is given by the sum of the repulsive and elastic energy terms.

$$F = F_{rep} + F_{el} \cong k_B T\left(\upsilon \frac{N^2}{R^3} + \frac{R^2}{Na^2}\right) \qquad \text{Equation 7}$$

The total free energy has a minimum at

$$R = \left(\upsilon a^2 N^3\right)^{1/5} \qquad \text{Equation 8}$$

Thus we find that the scaling exponent of radius with polymer length is $y = 3/5$. It is important to note that while the Flory calculation gives an accurate result for the equilibrium radius, this derivation benefits from the remarkable cancellation of two errors. Both the entropic spring term and the volume exclusion term overestimate the energies. Thus, while the Flory approach can safely determine R, caution should be exercised if using this approach for the calculation of dynamical polymer properties. More can be found on this topic in the book by deGenne's [4].

2.3 Electrolyte Solutions in Nanochannels

In order to understand the behavior of single DNA molecules in nanochannels, it is necessary to first describe the chemical properties of the nanochannel/buffer system. For single-molecule optical detection experiments, nanochannels are fabricated as trenches in fused silica, and are capped with a second fused silica wafer, resulting in four silicon dioxide channel walls. As in any micro/nano-fluidic device, the chemical properties of the walls in aqueous solution play an important role in determining the behavior of the device. Fortunately, these properties have been extensively studied for silicon dioxide substrates in various types and concentrations of electrolyte solutions. The resulting electric potentials and ionic distributions are also well understood and are explained in the literature [8]. In this section, the relevant pieces are reviewed.

2.3.1 Electrolyte Properties

We begin with the basic properties of electrolyte solutions. They are formed by the dissolution of electrolytes in a solvent; commonly acids, bases, or salts in water. The components of an electrolyte compound may strongly or weakly dissociate, depending on their thermodynamic properties in the solvent. The degree of dissociation for a given compound can be calculated using tabulated values. For the general reaction $A_xB_y \leftrightarrow xA + yB$, the dissociation constant is defined as $K_d = [A]^x[B]^y / [A_xB_y]$ where terms in brackets represent concentration in molarity. In this way, given a known initial concentration of electrolyte, the concentration of charged ions resulting from the electrolyte dissociation can be determined.

For acids or bases in aqueous solution, the acid or base dissociation constant K_a or K_b can be used to predict the concentrations of H^+ and OH^- ions as well as that of the conjugate acids and bases. For the acid dissociation reaction

$AH + H_2O \leftrightarrow A^- + H_3O^+$, AH is the acid and A^- is the conjugate base. The acid dissociation constant is defined as $K_a = [H_3O^+][A^-]/[AH]$. Commonly for acids and bases the quantities $pH = -\log_{10}[H^+]$, $pK_a = -\log_{10}[K_a]$, and $pK_b = -\log_{10}[K_b]$, are used for convenience.

Rearranging the equation for K_a, and taking the negative logarithm of both sides, results in $pH = pK_a - \log[HA/A^-]$ which is the Henderson-Hasselbalch equation. Given a known $[HA]$, pK_a and pH, it is possible to calculate the concentration of conjugate base ions (or conjugate acid ions if we are talking about a base). This is important for determining solution characteristics such as ionic strength or ionic screening length, concepts which are discussed further below. It should be noted that both monoprotic and polyprotic acids and bases are possible, and in the case of polyprotic acids and bases, multiple pK_a and pK_b values are available in the literature.

In order to characterize the electrical properties of a solution, a quantity called ionic strength is defined as $\Gamma/2 = (1/2)\sum_i z_i^2[c_i]$, where z_i is the valence and c_i is the concentration of the ith ionic species. While the desired concentration of dissociated salt ions is often in the mM range, it is important to bear in mind that the dissociation of water into hydroxide and hydronium ions sets the lower limit on the possible concentration of charged species in aqueous solution at $10^{-7} M$.

2.3.2 Surface Charge

Prior to immersion in an aqueous solution, the silicon dioxide surfaces of the channel walls are terminated with uncharged silanol groups. In a solution, however, a fraction of these groups ionizes. Given a known pK_a for the surface group, and a known

solution pH, the probability of deprotonation can be determined using the Henderson-Hasselbalch equation. For the case of silicon dioxide, the silanol groups on the surface have $pK_a = 5$. If the buffered solution is $pH = 8.3$, as is often the case, then 99% of the surface sites are ionized. An estimated surface density of between 5×10^{14} [9] and 32×10^{14} [10] sites per cm^2, results in a surface charge density of roughly $-100 \mu C / cm^2$. Given this surface charge, if the capacitance of the buffer/solution interface is known, it should be possible to calculate the difference in electric potential between the buffer and bulk solution. In the next section, we develop the concept of the double layer, which could be used to estimate that capacitance.

2.3.3 Double Layer

This surface charge results in an electric field in the solution, an accumulation of oppositely charged ions (counter-ions), and a depletion of like charged ions (co-ions) near the wall. The plate of charge on the surface together with the diffuse region of charge in solution near the surface is referred to as the electric double layer. Numerous models exist to describe the double layer in detail. A version of the Gouy-Chapman-Stern (GCS) model is depicted in Figure 2, and shows a negatively charged surface in contact with an ionic solution. Solvated counter-ions exist in high concentration near the charged surface. Due to solvation, they are not able to directly contact the wall material but can be located as close as the diameter of one water molecule from the wall. Depending on surface and ion chemistry, some ions may specifically adsorb to the surface. Often the energy of specific adsorption is enough to disrupt the solvation layer, allowing ions to directly contact the surface.

The layer of specifically adsorbed ions and the solvated ions nearest to the surface is referred to as the Stern layer. For the most part, this compact layer of ions can be considered immobile. Beyond the Stern layer is a layer of counter-ions and co-ions which are not packed tightly enough to be held in place. This mobile layer of ions, called the diffuse layer, is responsible for various electrokinetic effects. We therefore describe both the electric potential and the ionic distribution as a function of distance from the surface.

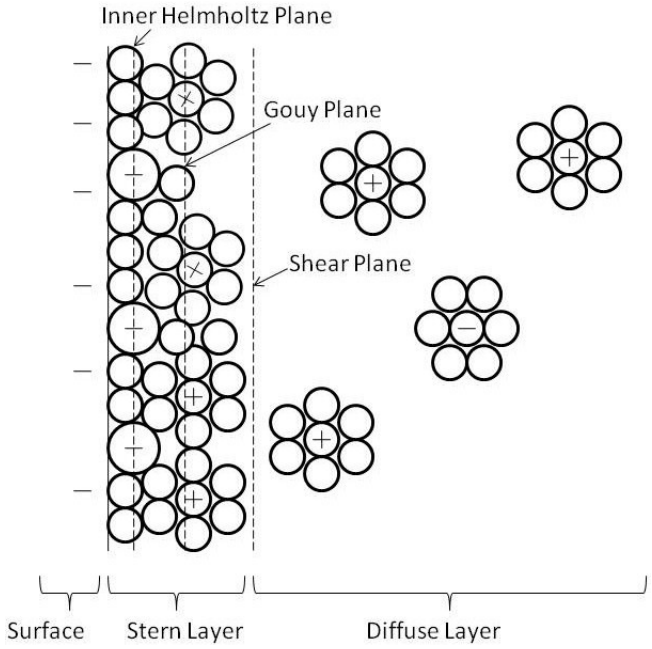

Figure 2. Modified Gouy-Chapman-Stern model of the electric double layer near a negatively charged suurface. Water molecules (empty circles) adsorb to the surface or to ions in solution. Specifically adsorbed anions (large circles with negative sign) and cations (not shown contacting wall) may lie at the inner Helmholtz plane. Hydrated cations (circles with positive signs surrounded by water molecules) may lie at the Gouy plane or in the diffuse layer. The potential at the shear plane is called the zeta potential.

2.3.4 Calculation of Local Ion Concentration and Electrostatic Potential in the Diffuse Layer

In this double layer model, the interface between the Stern and diffuse layers is called the shear plane, at which location the no-slip boundary conditions are applied when solving for potential and ion distributions. As mentioned above, the electric potential at the shear plane is referred to as the zeta potential, ζ. Assuming, for the moment, that the value of ζ can be determined, it is possible to calculate the potential at any point in the diffuse layer. We use the Poisson-Boltzmann equation, which is obtained by starting with the Poisson equation, and rewriting the charge density using Boltzmann statistics.

$$\nabla^2\psi(y) = \frac{-\rho_e}{\varepsilon} = \frac{-1}{\varepsilon}\sum_i c_{0,i} e z_i \exp\left(-\frac{e z_i}{k_B T}\psi(y)\right) \qquad \text{Equation 9}$$

where y is the distance between point in solution and the shear plane, $\Psi(y)$ is the electric potential at y, e is the charge of a proton, $c_{0,i}$ is the bulk concentration of the i^{th} ionic species, z is the valence of the i^{th} ionic species, and ε is the dielectric constant of the fluid. Analytical solutions for this equation are available only for certain geometries and under limited buffer conditions. Presently, we obtain an approximation for electric potential near a single infinite plate. For the case of a symmetric electrolyte, Equation **9** becomes $\nabla^2\psi = (2c_0 ez/\varepsilon)\cdot\sinh(ez\psi/k_B T)$. Applying the boundary conditions $\Psi(0) = \zeta$ and $\Psi(\infty) = 0$, the solution is:

$$\Psi(y) = \frac{2k_B T}{ze}\ln\left[\frac{1+\tanh(\zeta ze/4k_B T)\exp(-y/\lambda_D)}{1-\tanh(\zeta ze/4k_B T)\exp(-y/\lambda_D)}\right] \qquad \text{Equation 10}$$

where F is Faraday's constant, R is the molar gas constant, T is the temperature in degrees Kelvin, and λ_D is the Debye length, which characterizes the length scale over which a charged surface is screened by ions in solution, and is given by:

$$\lambda_D = \sqrt{\frac{\varepsilon RT}{2F^2(\Gamma/2)}} \qquad \text{Equation 11}$$

2.3.5 Zeta Potential

The potential at the shear plane directly affects a number of electrokinetic phenomena. Electroosmosis, particle electrophoresis, and streaming potential are all interpreted in terms of the zeta potential. It is therefore important to understand how it may be affected by solution properties. An abundance of experimental work has led to the following scaling relations:

$$\zeta \sim \lambda_D \qquad \zeta << 2k_BT/e \approx 50mV \qquad \text{Equation 12}$$

$$\zeta \sim \log(\lambda_D) \qquad \zeta >> 2k_BT/e \approx 50mV \qquad \text{Equation 13}$$

for λ_D varying with indifferent (non specifically adsorbing) counterion concentration . These two relations are used in the next section. Dependencies of ζ on pH, temperature, counterion valency and counterion size, and the possibility of specific adsorption have also been shown, as described in ref [8], though they will not be explored in this chapter.

2.3.6 Properties of TBE Buffer Used in Experimental Sections

DNA nanochannel experiments in the literature have been performed under a variety of buffer conditions. While, traditionally, high ionic strength buffers (5X and 1X TBE) have been used, recently several reports have investigated the effect of low ionic strength buffers on DNA extension in both nanoslit and nanochannel devices [11]. Much debate exists as to the proper interpretation of results, and so this represents an interesting area of investigation for the theory of confined polymers.

Table 1. Ionic strength, debye screening length, and zeta potential at the fused silica/ electrolyte shear plane for each of the five buffers. All values for ionic strength and debye screening length are calculated using theoretical models. The value for zeta potential of silica in 1X buffer was measured experimentally in the literature [12]. Values for zeta potential at other ionic strengths are extrapolated using Equations 12 and 13.

As-mixed Component	5X with beta	1X with beta	0.5X with beta	0.05X with beta	0.005X with beta
Ionic Strength	0.15 M	0.031 M	0.016 M	0.0031 M	0.0003 M
Debye Screening Length	0.78 nm	1.8 nm	2.5 nm	5.5 nm	17 nm
Fused Silica Zeta Potential	-21 mV	-40 mV	-48 mV	--	--

The most notable effects of high ionic strength are the suppression of electroosmosis relative to electrophoresis of DNA, and the short Debye screening lengths. These conditions serve to simplify both the experimental procedure of manipulating DNA in channels, and the theoretical interpretation of results in terms of polymer models, by allowing molecules to be modeled as uncharged cylinders. The experiments described in Chapters 3, 4 and 5 of this thesis were all performed under high ionic strength conditions (5X TBE with 4% β). While the proposed experiment of the Chapter 6 will almost certainly require low ionic strength conditions, for the purpose of developing confined polymer models we limit our discussion to the high ionic strength regime.

2.4 Model for DNA in Nanofluidic Channels

In section 2.1 we used polymer models to describe the conformation and dynamics of DNA molecules in free solution. Now, we will see that if the same molecules are inserted into long, narrow nanochannels, their behavior changes dramatically. For example, it was shown that an unconstrained molecule assumes a spherical shape, with an end to end radius that scales with the number of monomers as $R \propto N^{3/5}$. Now, however, we force the molecule to enter a channel which has a diameter much smaller than the free solution R. The result is that the molecule is tightly confined in two dimensions, but elongates very far in the third dimension, the direction of the channel axis [4].

Furthermore, the average separation distance between the first and the last monomer has different functional dependence on the total number of monomers. This separation distance, which we now call L_z, is essentially the extent to which the molecule stretches along the channel axis. Instead of $R \propto N^{3/5}$ we now have $L_z \propto N$. This has important implications for nanochannel based DNA length measurements. If, for example, a hybridized probe is bound at some position along the molecule, the linear scaling of extension length with monomer number allows for a one to one mapping between the spatial position along the polymer, and the position within the genome.

In addition to the scaling of L_z with N, extension length has a number of other dependencies, such as with channel diameter, the Debye screening length, and the DNA persistence length. In order to explain those dependencies, we now build upon the DNA free-solution polymer model to generate a model which is applicable in confined environments.

2.4.1 deGenne's Blob Model for Linear Polymers in Cylindrical Confinement

Here we review the statistical properties of single molecules confined to channels such that the following conditions are met: $R > D > l_P$ [4]. The reasons for these conditions are straightforward. First, the channel diameter must be smaller than the molecule's free solution radius of gyration. If it is not, the molecule will not need to deform in order to enter. Second, the local bending of the molecule must occur over a distance shorter than the channel diameter. If this condition is met, the DNA molecule may be modeled as a series of blobs lined up along the axis of the channel. This model, first proposed by deGennes' has proven to be valid for double stranded DNA molecules with lengths of a few kilobases or longer, in channels ranging from roughly one-hundred to several hundred nanometers in diameter. It is therefore the model of choice for the remainder of this chapter.

Figure 3 depicts a confined DNA molecule in the blob model picture. In the model, the molecule partitions into a series of blobs, each with a diameter equal to the channel diameter, D. The monomers within each blob act very much like they would inside a small sphere in free solution, and so the number of monomers per blob must satisfy the relation $D = ag^{3/5}$. This is the same as Equation **8** with the variable for the total number of monomers in the molecule, N, replaced by one for the number of monomers per small blob, g. The number of blobs is given by N/g, so that the full scaling law for the equilibrium extension length of the molecule along the direction of the channel axis is

$$L_Z = \frac{N}{g} \cdot D = N \cdot a \frac{g^{3/5}}{g} = Na \cdot g^{-2/5} = Na \cdot (a/D)^{2/3} = L_C \frac{(L_p w)^{1/3}}{D^{2/3}} \qquad \text{Equation 14}$$

Following deGennes' argument that the confined blobs lose their ability to diffuse in three dimensions, the free energy cost for confinement of a single blob is of order $k_B T$, and the free energy of confinement for the full length molecule is $k_B T$ times the number of blobs.

$$F_{conf} = k_B T \cdot \frac{N}{g} = k_B T \cdot N \cdot \left(\frac{a}{D}\right)^{5/3} \qquad \text{Equation 15}$$

As is evident, the energy cost associated with confinement goes up with decreasing channel size. Because of this, in situations where the degree of confinement is not uniform along the length of the molecule, a free energy gradient exists. This results in an entropically induced force on the molecule. Such a force acts only on the portion of the molecule which can "feel" the nonuniform degree of confinement by testing the space via diffusive motion. Specific examples of non-uniform-confinement induced forces are described in later chapters. For the remainder of the present chapter, we focus on the dynamics of molecules undergoing thermal agitation only.

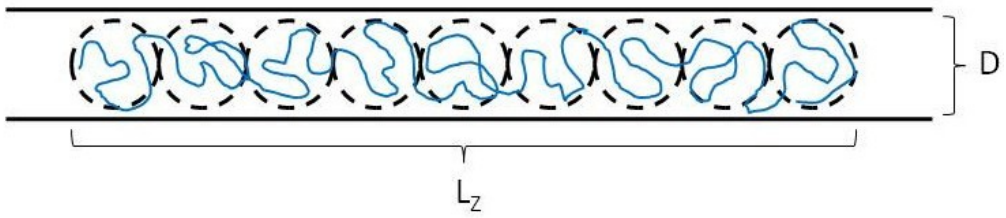

Figure 3. Cartoon of a confined DNA molecule (Blue) in nanochannel of diameter, D. Volume exclusion effects cause the molecule to elongate along the direction of the channel axis, with an extension length given by Lz. According to the deGennes' model, the molecule is viewed as a series of noninterpenetrating spherical blobs (Black Dashed Outlines). Each blob has a diameter equal to the channel diameter.

2.4.2 Thermally Induced Motion of DNA Molecules in Nanochannels

Polymer segments within each blob act as if they are part of a large sphere in free solution. Monomers can feel one another's presence through hydrodynamic interactions (i.e. propogation of momentum through the solvent). However, over a distance larger than the channel diameter, hydrodynamic interactions are quickly damped by the channel walls. Therefore monomers belonging to different blobs and separated by a distance greater than D are hydrodynamically screened from one another. The friction , then, scales linearly with the extended length of the molecule. The expression $\xi = 6\pi\eta L_z$, where η is the viscosity of the solvent, is derived in an article by Brochard and deGennes [13]. Thus, friction increases for longer molecules and for smaller diameter channels. We will use this expression for the friction momentarily.

Thermal agitation of the blobs cause fluctuations in the end to end extension length of the confined DNA molecule. When a strand experiences such random extensions or compressions about its equilibrium length, it responds like a spring by resisting that extension or compression. Given a channel with a constant diameter D, we can use Equation 14 and 15 to obtain an expression for the spring constant. After rewriting Equation 14 to solve for D and substituting this expression for D in Equation 15, we obtain

$$F_{conf} = k_B T \cdot N \cdot \left(\frac{L_Z}{L_C}\right)^{5/2} \qquad \text{Equation 16}$$

Using the fact that the spring constant is the curvature of the free energy function,

$$k = \frac{\partial^2 F_{conf}}{\partial L_z^2} = \left(\frac{5}{2}\right)\cdot\left(\frac{3}{2}\right)\cdot k_B T \cdot N \cdot \frac{L_z^{1/2}}{L_C^{5/2}}$$

$$= \left(\frac{15}{4}\right)\cdot k_B T \cdot N \cdot \frac{1}{L_C^{5/2}} \frac{L_C^{1/2}(pw)^{1/6}}{D^{1/3}}$$

$$= \left(\frac{15}{4}\right) \cdot k_B T \cdot N \cdot \frac{(pw)^{1/6}}{N^2 \cdot a \cdot (pw)^{1/2} \cdot D^{1/3}}$$

$$= \left(\frac{15}{4}\right) \cdot \frac{k_B T}{L_C} \left(\frac{1}{pwD}\right)^{1/3}$$

Equations 17

We can use this expression for k in Hook's Law, the standard equation for the force exerted by a spring $f_{spring} = -kx$ where x is the displacement from equilibrium. It should be noted that an extended molecule in a channel only has some relation to a true Hookian spring. While the expression for instantaneous force as a function of displacement is identical, the typical equations of motion are not. As described, thermal agitation causes the molecule to randomly expand or compress to some length other than its equilibrium extension length. However, because the ratio of inertial forces to viscous forces in these systems is so low (i.e. Reynolds number less than 1), the contracting or expanding DNA molecule cannot accumulate momentum during the return to equilibrium. Therefore, a plot of the extension length versus time is not sinusoidal. This is evident in the time trace of Figure 4a.

What sense can be made of the spring-like nature of the molecule, and of its apparently random fluctuations in extension? In fact, over a short period of time, the measured lengths from a series of snapshots of the molecule are correlated [14]. After a thermally induced extension, there is a mean relaxation time, τ, over which the molecule returns to its equilibrium length. For the lowest vibrational mode, this is given by $\tau = \xi / k$.

$$\tau \cong \frac{8\pi}{5} \frac{\eta L^2}{k_B T} \frac{(pw)^{2/3}}{D^{1/3}}$$

Equation 11

This is an important fact to consider. It means that in order to obtain a series of statistically independent length measurements, we must wait a minimum time, τ, between each measurement.

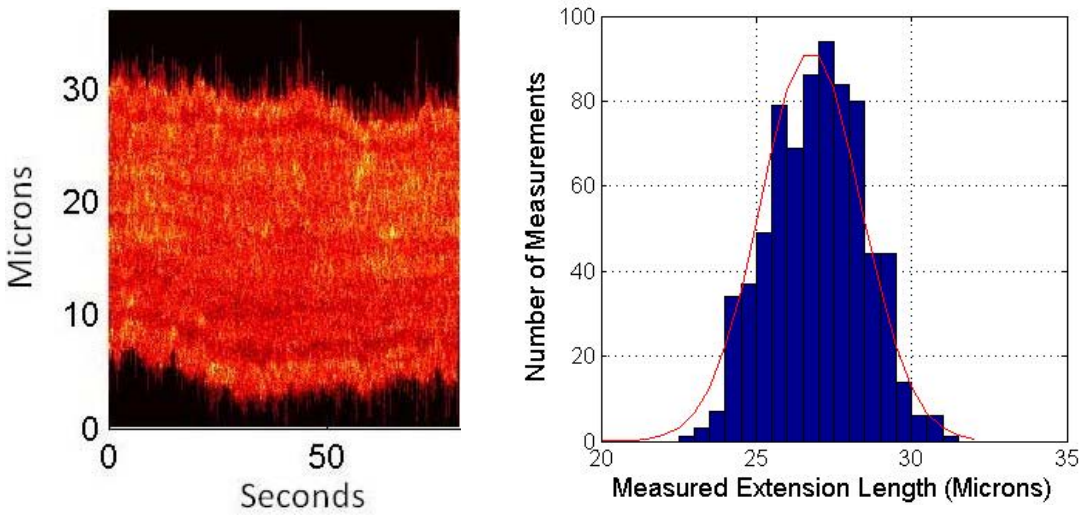

Figure 4. A) Time trace showing extension length in channel over 80 sec. The relaxation time for this molecule is approximately 10sec. While some correlation exists among nearby frames, the extension length does not evolve through time as it would for a classical spring. **B)** Histogram of lengths measured over the same time trace. As the number of measurements increases, the distribution is approaches a Gaussian about the mean value $L_Z = 26.7 \mu m$.

Further evidence of the spring-like nature of the molecule can be seen by plotting the measured extension lengths in a histogram. The result is a Gaussian distribution of lengths centered on the mean extension length, with a standard distribution, σ, that can be calculated using statistical mechanics. The change in free energy associated with a thermally induced expansion or compression of the molecule can be calculated using as $\delta F_{conf}(L_z) = F_{conf}(L_z) - F_{conf}(L_E)$. In the canonical ensemble, the probability

of observing the molecule in a given extended state is $P(L_Z) \propto \exp\left(-\delta F_{conf}(L_z)/k_B T\right)$. The width of the Gaussian curve in Figure 4b is the square root of the variance, with the variance given by

$$\left\langle \delta L_Z^2 \right\rangle = \frac{k_B T}{k} = \frac{4}{15} L_C [pwD]^{1/3} \qquad \text{Equation 19}$$

We have established expressions for both the average extension length, L_z, and its standard deviation. Assuming, for the moment, that the dominant contribution to the error of a single length measurement is thermal agitation of the molecule, we define the resolving power of the system to be $R = L_z/\sigma_t$. Using Equation 14 and 19 yields

$$R \cong \frac{15}{4}\sqrt{L_C}\,\frac{(pw)^{1/6}}{D^{5/6}} \qquad \text{Equation 12}$$

The resolution improves for longer molecules. This is an interesting result because the resolution for length measurements using gel electrophoresis scales in the opposite way, causing analysis of longer molecules to be more costly and time-consuming. This is further evidence that the first marketable nanochannel devices may be those that address the kilobase to megabase DNA length regime.

2.5 Conclusion: Chapter 2 Summary and Relation to Subsequent Chapters

In this chapter we have presented mathematical models which describe the conformation and motion of DNA in nanofluidic channels. We began by introducing models for self avoiding polymers in free solution. We then discussed electrolyte solutions in nanochannels, reviewing surface charge and mobile ion distributions. Finally, we modified free solution models for DNA in order to describe the same DNA molecules in highly confining nanochannel environments. The analysis led to a determination of the factors contributing to DNA length measurement resolution. This

theoretical framework provides the reader with a basic knowledge of the physics and challenges associated with DNA in nanochannels, and prepares the reader to critically evaluate the remaining chapters of the thesis. Here we describe the relation of theory covered in this chapter to each of the remaining chapters.

As mentioned in the Introduction, Chapter 3 is a published review of single molecule detection and manipulation using nanofluidic structures. While the first part of this review focuses on the use of nanostructures for tailoring a diffraction limited focal volume, the second part discusses the use of nanofabricated slits and cavities for manipulating DNA molecules. The DNA models presented in Chapter 2 are the base for understanding the many different experiments performed on confined molecules, that are summarized in Chapter 3.

The original experiment presented in Chapter 4 describes the force experienced by a molecule straddling the interface between a microchannel and a nanochannel, and the resulting motion. While blob theory is not used explicitly in this paper, it is necessary to have an understanding of equilibrium extension length for a confined molecule, as well as the effect that confinement has on conformational free energy. The experiment presented in Chapter 5, also, does not explicitly use a blob theory expression, however the concepts of excluded volume interactions, equilibrium extension length, and free energy of confinement are again critical. During data analysis, both of the experiments described in these chapters benefitted from an understanding of length measurement error. Furthermore, both the experiments in Chapters 4 and 5 could be built upon by future researchers simply by varying parameters such as channel diameter or ionic strength, as is evident by an

understanding of the models described in Chapter 2. This would likely result in valuable data, adding to our understanding of the physics of confined polymers.

Finally, the device and experiment described in Chapters 6 and 7 relies heavily on the concepts of ion distributions and charge screening in nanochannels, the groundwork for which has been developed in Chapter 2.

REFERENCES

1. Reccius, C.H., et al., *Conformation, length, and speed measurements of electrodynamically stretched DNA in nanochannels.* Biophysical Journal, 2008. **95**(1): p. 273-286.
2. Watson, J.D. and F.H.C. Crick, *MOLECULAR STRUCTURE OF NUCLEIC ACIDS - A STRUCTURE FOR DEOXYRIBOSE NUCLEIC ACID.* Nature, 1953. **171**(4356): p. 737-738.
3. Wing, R., et al., *CRYSTAL-STRUCTURE ANALYSIS OF A COMPLETE TURN OF B-DNA.* Nature, 1980. **287**(5784): p. 755-758.
4. deGennes, P.-G., *Scaling Concepts in Polymer Physics*. 1979, Ithaca, NY: Cornell University Press.
5. Doi, M., *Introduction to Polymer Physics*. 2001, Oxford: Clarendon Press.
6. Doi, M. and S.F. Edwards, *The Theory of Polymer Dynamics*. 1986, Clarendon Press: Oxford.
7. Onsager, L., *THE EFFECTS OF SHAPE ON THE INTERACTION OF COLLOIDAL PARTICLES.* Annals of the New York Academy of Sciences, 1949. **51**(4): p. 627-659.
8. Kirby, B.J. and E.F. Hasselbrink, *Zeta potential of microfluidic substrates: 1. Theory, experimental techniques, and effects on separations.* Electrophoresis, 2004. **25**(2): p. 187-202.
9. Revil, A., P.A. Pezard, and P.W.J. Glover, *Streaming potential in porous media 1. Theory of the zeta potential.* Journal of Geophysical Research-Solid Earth, 1999. **104**(B9): p. 20021-20031.

10. Scales, P.J., et al., *ELECTROKINETICS OF THE SILICA SOLUTION INTERFACE - A FLAT-PLATE STREAMING POTENTIAL STUDY.* Langmuir, 1992. **8**(3): p. 965-974.
11. Reisner, W., et al., *Nanoconfinement-enhanced conformational response of single DNA molecules to changes in ionic environment.* Physical Review Letters, 2007. **99**(5).
12. Hsieh, S.S., H.C. Lin, and C.Y. Lin, *Electroosmotic flow velocity measurements in a square microchannel.* Colloid and Polymer Science, 2006. **284**(11): p. 1275-1286.
13. Brochard, F. and P.G. Degennes, *DYNAMICS OF CONFINED POLYMER-CHAINS.* Journal of Chemical Physics, 1977. **67**(1): p. 52-56.
14. Tegenfeldt, J.O., et al., *The dynamics of genomic-length DNA molecules in 100-nm channels.* Proceedings of the National Academy of Sciences of the United States of America, 2004. **101**(30): p. 10979-10983.

CHAPTER 3
NANOFLUIDIC STRUCTURES FOR SINGLE BIO-MOLECULE FLUORESCENT DETECTION*

***Published Journal Article: Biopolymers 2007, Volume 85, Issue 2, pg 131**

J. T. Mannion and H. G. Craighead

School of Applied and Engineering Physics

Cornell University, Ithaca, NY

Fluid-filled nanofabricated cavities can be used to increase the spatial resolution of single molecule confocal microscopy based techniques by creating smaller and more uniformly illuminated probe volumes. Such structures may also be used to temporarily stretch single macromolecules, permitting the resolution of molecular details that would otherwise be beyond the capabilities of a diffraction limited system.

Introduction.

A variety of techniques are being explored to detect, manipulate, and identify individual biological molecules. While analytical methods such as fluorescence correlation spectroscopy (FCS) (1) and fluorescence recover after photobleaching (FRAP) can be used with diffraction limited optical systems (2), there exist several approaches for beating the diffraction limit. Total internal reflection fluorescent microscopy (TIRF) (3) and near field scanning optical microscopy (NSOM) (4,5) rely on decaying evanescent waves to create a sub-diffraction limited focal volume. Two-

photon excited fluorescence is also available as a method for shrinking illumination volume and increasing signal to noise (6,7), and can be used non-invasively on living organisms (8).

Nanofabricated, fluid-filled structures have been used to decrease illumination volume, both increasing signal to noise and the working concentration at which single molecule experiments may be run (9). Such devices consist of a series of channels, apertures or cavities of other shapes with dimensions on the order of ten to several hundred nanometers. For the cases in which these features are smaller than the wavelengths of the light source used for detection, they can direct and confine light more precisely than can be done using diffraction limited optics. Specifically, they have been used for single molecule measurements regarding binding kinetics (10), diffusion of molecules confined to lipid membranes (11), detection of multiple fluorescent labels in a heterogeneous solution (12,13), and DNA fragment sizing (14). The technologies which perform these tasks fall into one of two categories, namely they are either “zero mode wave-guides” or “sub-micrometer channels”.

Additionally, nanofluidic structures are of particular use in the analysis of biological polymers. When a cavity is smaller than the free solution diameter of a polymer, the nanostructure can be used to constrain the molecule in one or two spatial dimensions. The resulting entropically mediated forces cause the molecule to extend in the unconstrained dimensions. Given the polymeric properties of and interest in genomic DNA, these molecules are prime candidates for such manipulation and analysis. The second half of this review discusses ways in which nanofluidic structures can be used to measure the mechanical properties of single DNA molecules (15-18) and perform sequence analysis (19-22). As with the structures that are used to confine light, the

devices that perform these tasks can be placed into one of two categories. They are either “nanoslits”, which allow a DNA strand to exist in a quasi two dimensional plane, or they are called “nanochannels” and confine the polymer to a line.

Nanofluidic structures for modifying sample illumination.

In order to obtain single molecule occupancies in a diffraction limited focal volume, dilute concentrations are needed, a requirement which may be undesirable or even prohibitive depending on the sample and experiment (9,10). The kinetics of many

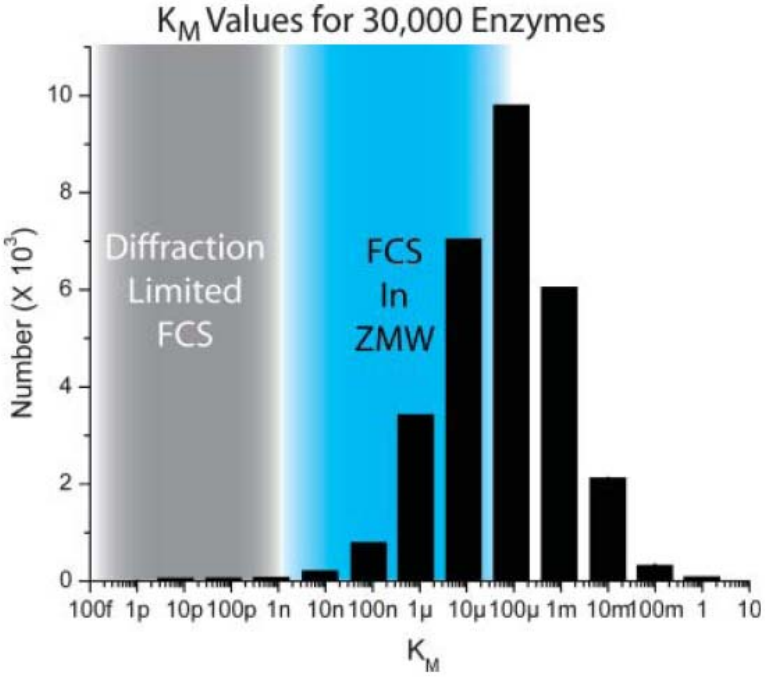

Figure 1. A Histogram of K_M values for 30,000 enzymes taken from the Brenda Database (www.brenda.uni-koeln.de). The effective concentration ranges for diffraction limited and zero-mode waveguide FCS are shown in grey and blue, respectively. Kinetics for the vast majority of enzymes are out of reach for diffraction limited FCS. FCS is not yet a viable tool above the 100 μM regime. Figure reprinted with permission (10).

enzymes, for example, can only be studied at physiologically relevant concentrations (Figure 1). Smaller probe volumes allow single molecule occupancy at higher concentrations and also provide the benefit of reduced background noise from Raman scattering of solvent molecules and fluorescent impurities.

Zero Mode Waveguides

Circular apertures, fabricated in a thin layer of aluminum on a glass cover slip, provide a reduced focal volume and allow for single molecule detection at concentrations as high as $200\mu M$ (9). These structures, called zero-mode waveguides (ZMW), exhibit a cut-off wavelength $\lambda_c = 1.7d$, where d is the ZMW diameter, above which no propagating guided modes exist in the metallic system. Light of wavelengths longer than λ_c decays exponentially along the length of the aperture, and is confined in the transverse plane by the walls of the hole. For the smallest ZMWs the depth of decay is 10 or 20 nm and $V_{eff} < 10^{-20} L$, or 10 zeptoliters. This is more than four orders of magnitude smaller than a diffraction limited probe volume.

Such apertures were first used to monitor the synthesis of double stranded DNA by polymerase enzymes fixed to the bottom of a ZMW (figure 2), an assay which represents a promising approach for single molecule sequencing (23-25), and as mentioned, have applications for measuring binding kinetics. The oligomerization of a λ-repressor protein, for example, occurs at concentrations ranging from $10nM$ to $100\mu M$ and its multiple kinetic binding constants can be precisely determined using a zero-mode waveguide (10).

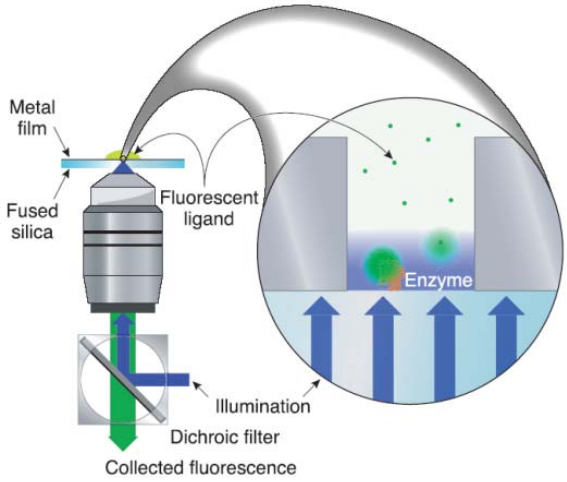

Figure 2. Use of a ZMW with a confocal microscopy setup. In one scenario, fluorescently labeled analyte molecules interact with an enzyme bound to the bottom of aperture. Figure reprinted with permission (9).

Another application is in the study of lipid membranes, an area in which there are many topics of interest. Membrane bound receptor binding kinetics, lipid domain dynamics, and membrane bound ion channel behavior, for example, may all be studied using fluorescent detection (7,26,27). In addition to offering roughly an order of magnitude shallower illumination depth than does TIRF microscopy, zero-mode waveguides provide high spatial resolution in the transverse plane. Apertures as small as 50 nm can be used to investigate lipid diffusion and binding kinetics for a receptor on a liquid-disordered phase membrane (11). While not all membranes will penetrate into the hole (some gel phase membranes will not (11,28)) the more flexible membranes will protrude far enough that they interact with the observation volume (figure 3). Information regarding the shape of the membrane within the aperture can be gained through measuring the diffusion of fluorescent molecules constrained to membrane, and the binding affinities of molecules for membrane bound receptors can

also be determined. It is even possible to investigate living cell membranes (29). Work currently being done in our lab includes investigating the effects of microtubules and actin filaments on cell membrane penetration.

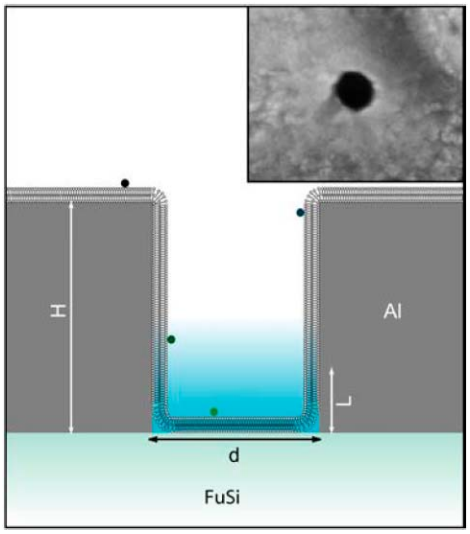

Figure 3. Lipid bilayer membranes are thought to coat the surface of the zero mode waveguides. The structures are characterized by a diameter, typically between 50 and 200 nm; a height, ~ 100 nm; and a characteristic evanescent decay length that ranges from 15 nm for small structures to more than 35 nm for larger ones. These experiments used fluorescently labeled lipid DHPE-Oregon Green and tetanus toxin-Alexa488 as fluorescent probes. The fluorophores are only excited and detected when near the bottom of the structure, in the evanescent field, providing a focal volume on the order of a few tens of zeptoliters. The zero mode waveguides are illuminated from the bottom by a microscope in epi-illumination mode. (Inset) Scanning electron micrograph of a zero-mode waveguide. Figure reprinted with permission (11).

Submicrometer Channels

Having the option to adjust flow rate through the detection region, enables the balance of competing factors such as throughput and detection efficiency. Submicrometer-

sized fluidic channels allow this while maintaining focal volume restriction (30). Such channels can be fabricated on fused silica wafers using metal oxide semiconductor (MOS) compatible processes, allowing for manufacturing scalability and permitting visible wavelength spectroscopy with low autofluorescence as compared to borosilicate or pyrex glass. A focused laser beam aligned to the channel results in an effective probe size with a length defined by the diffraction limit, but a width and

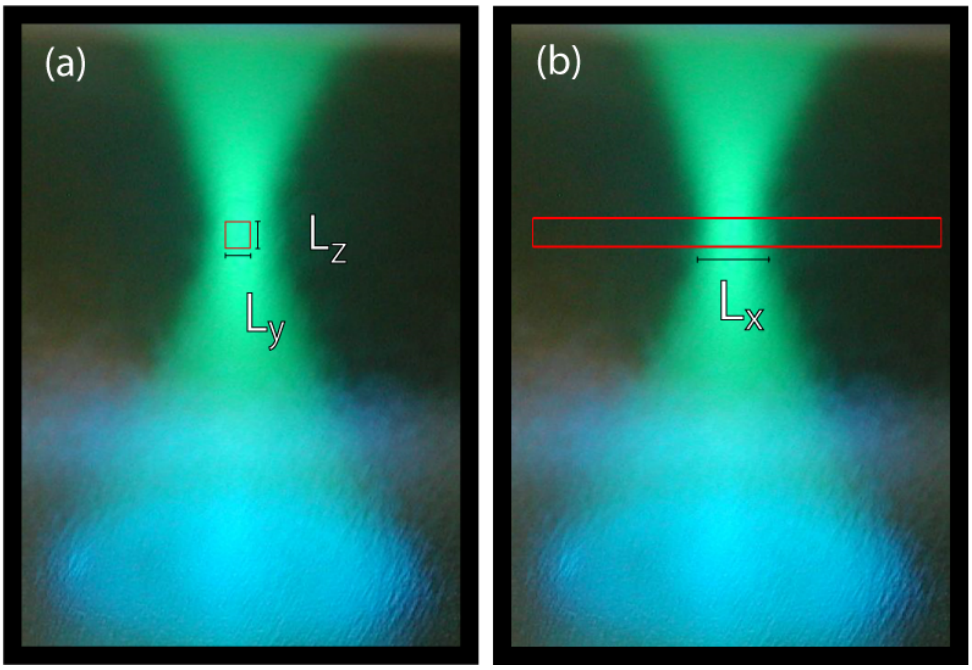

Figure 4. Artist's rendition of a gaussian beam focused on a channel with a cross section smaller than the spot size of the beam. Analyte flows inside of the channel (outlined in red) along the x-direction. **(a)** Cross sectional view of channel (red square). The width and height of channel, given by L_y and L_z, define the effective focal volume in two dimensions. Note that analyte is restricted to the brightest part of the spot in these two dimensions. **(b)** Side view of channel (partially outlined by red rectangle). The length of channel which is illuminated in this dimension is determined by the size of the diffraction limited spot.

height defined by the channel walls (figure 4). It is also worth noting that, for a diffraction limited spot in free solution, the majority of fluorophores are detected while traveling along the weakly illuminated edges of the observation volume, and confining molecular passage to the center of the illumination volume (figure 4) is a convenient way to minimize these low signal to noise events.

To identify multiple target molecules in a heterogeneous mixture, a set of distinguishable labels with high binding specificity must be available. Several choices are available for use with sub-microfluidic channels. Quantum dots are an excellent fluorophore due to their broad excitation and narrow emission spectrum and their high quantum yield, and can easily be incorporated into an assay (31). Dendrimer-like nucleic acid labels can be engineered to substantially increase the number of distinguishable probes in a set, starting with just two fluorophores, and may be designed to have a high affinity for any number of target molecules (13). In order to take advantage of such a versatile set of labels, two laser beams of different wavelengths can be focused on a channel enabling discrimination on the basis of both number and energy of photons collected in a signaling event (figure 5). Going a step further, separating the two spots by a distance as small as several microns along the channel, allows for single molecule mobility measurements (12).

New methods for DNA fragment sizing are constantly being sought, and sub-micron size channels offer one possible solution. In one of the most well cited works of this area, Foquet et al. analyze composition, molar fraction, mobility, and overall concentration, for a mixture of nine DNA fragments (14). Single DNA molecules can be electrophoretically driven through a detection region at speeds as high as 5 mm/s

and each spend as little as a few ms in the focal volume. Fragment sizing can be performed using only 76 fg of DNA (figure 6). This compares favorably with analysis of the same sample by gel electrophoresis, which requires 50ng of sample. Most notable is the large dynamic range in detection sensitivity. While efficient separation of both 30 kbp and 600 bp DNA is difficult to achieve on a single gel, sensitivity for an entire spectrum of fragment sizes is excellent using Foquet's approach.

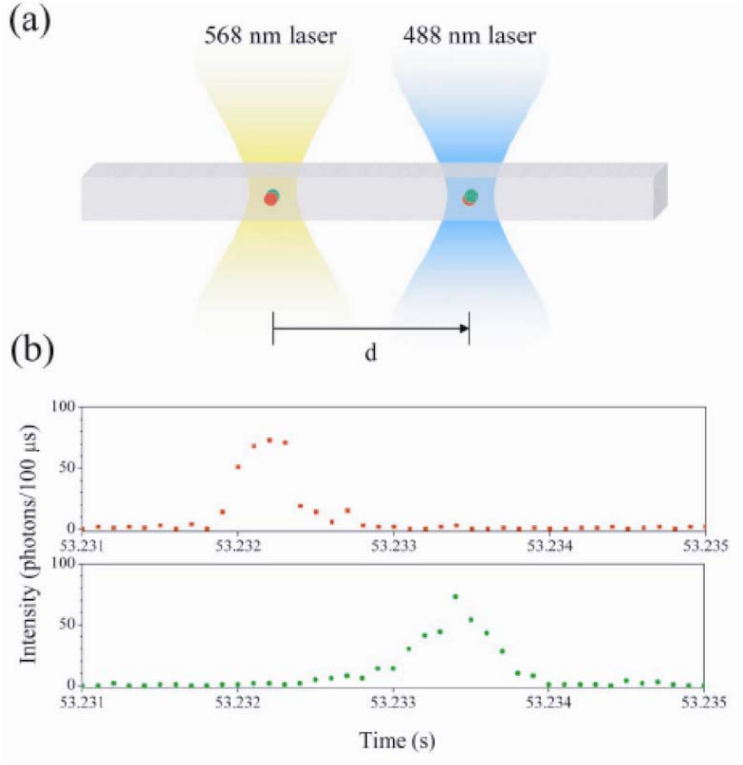

Figure 5. (a) Schematic of a sub-micrometer fluidic channel with two focused laser beams separated by a distance, d. Molecules with different color fluorophores flow through the channel and are detected. **(b)** Photon burst data collected from two separate detectors, one aligned to each of the two laser spots. Figure reprinted with permission (12).

Nanofluidic structures for directly altering the state of target molecules.

The conformation and mechanical properties of linear biological macromolecules, such as DNA, are important in their function. For DNA, structural properties govern actions such as packaging into chromatin and bacteriophage heads (32,33). To elucidate mechanical properties, optically trapped or magnetically responsive beads can be conjugated to a single DNA strand, enabling controlled stretching and twisting of the molecule (34,35). By fixing one end of a fluorescently labeled DNA strand in an elongational flow, it is also possible to observe inhomogenous hydrodynamic stretching, which is a theoretically interesting phenomenon (36,37). A single DNA strand may be visualized as interacts with pillars in a microfluidic slit (38-40), or as it escapes from a deep well into a thin slit, and it is hoped that the knowledge gained from such studies will lead to faster methods of lab-on-chip DNA sorting (41-47). Finally, sequence information may even be obtained from stretched molecules through restriction site mapping or motif mapping using hybridized probes (19,20,48).

Nanoslits

Confining a polymer to motion in two dimensions has been an experimentally difficult task to achieve, but has remained a topic of great interest in polymer physics (49). Though scanning probe techniques can accurately measure the contour of a molecule fixed to a surface, these contours correspond to projections of a 3-D molecule onto an x-y plane, rather than true 2-D states (50). A creative method for experimentally realizing quasi-2-dimensional diffusion was reported by Maier and Radler who collected comprehensive evidence for static scaling laws and Monte Carlo simulations of both statics and dynamics of 2D polymer chains (49). While they used a lipid bilayer to confine the DNA, alternative methods of confinement also have utility.

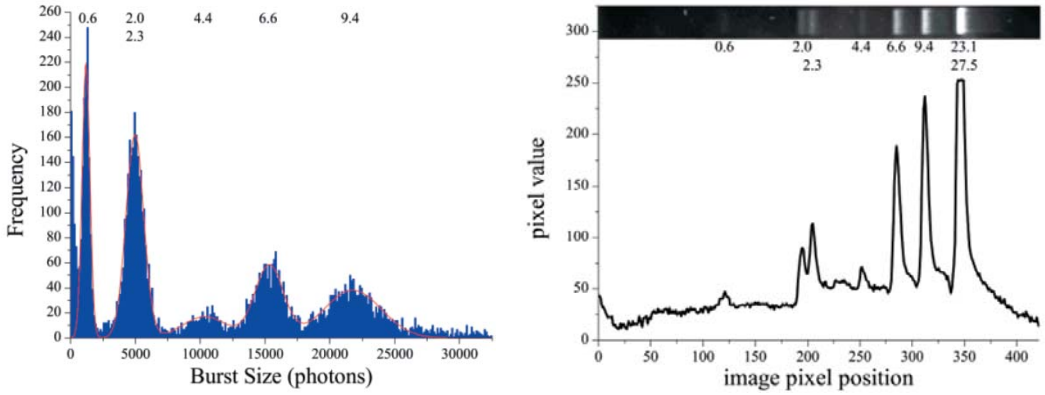

Figure 6. (Left) Section of a photon burst histogram showing the 0.6-kb fragment resolved over the background. The larger peaks were also visible but are not shown here. (**Right)** Image and line scan through the center of the image of the same sample, as obtained by gel electrophoresis. Figures reprinted with permission (14).

In addition to stretching via hydrodynamic forces, channels, planar slits, and pillar arrays, fabricated into glass or silicon wafers, can also be used to study the mechanical dynamics of a DNA molecule by employing entropic forces that arise due to confinement. To describe the origin of the confinement induced forces that enable single molecule control and visualization, it is useful to compare the size of a DNA strand with the dimensions of nanofabricated structures. A λ – bacteria-phage DNA molecule (48.6 kbp), for example, exists in free solution as a coiled sphere with a radius of less than $1\mu m$, but is $16\mu m$ in length when fully stretched. While pulling on the ends of a polymer is an obvious way to stretch it, nanofluidic methods employ an alternative approach causing elongation in one dimension, through compression in another. Compare the extent of the molecule in the three states depicted (figure 7) to diffraction limited spatial resolution in optical microscopy and it is possible to see the utility of confinement.

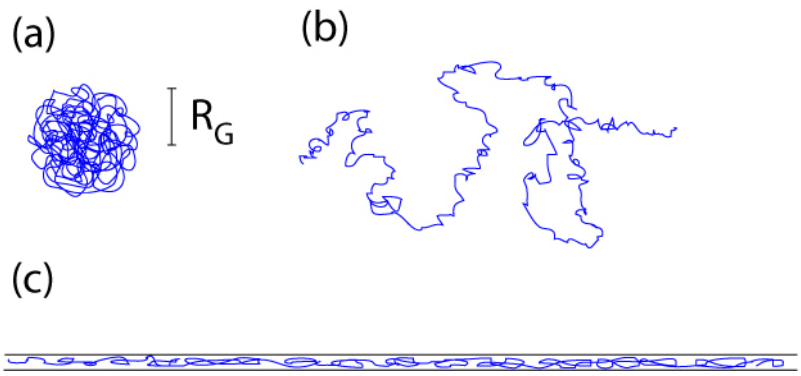

Figure 7. Cartoon of a DNA molecule **(a)** unconfined in free solution (R_G = radius of gyration), **(b)** confined in one dimension as in a nanoslit (depth of slit $<< R_G$), **(c)** confined in a nanochannel (diameter $<< R_G$). The three contours have been drawn roughly to scale relative to one another. Note that for diffraction limited optical detection of a λ – phage DNA strand, spatial resolution is smaller than, but on the order of R_G .

Using a thin slit geometry, it is possible to measure the transient stretching and subsequent relaxation for electrophoretically driven DNA molecules interacting with microfabricated posts (figure 8) (18). The effects of confinement are manifest in the stretching and relaxation dynamics.

As an alternative to hooking a molecule around posts, elongational fluid flow may be generated in a planar environment to efficiently stretch DNA. Using a labeling scheme analogous to the one in a genomic mapping technique called multicolor fluorescence in situ hybridization (FISH) (51), molecules can be hydrodynamically

stretched in a microfluidic device and detected with high throughput (figure 9). Such a device can be used to map 8 bp target sites on the 185.1 kb-long bacterial artificial chromosome BAC 12M9 with an accuracy of +- 2.1 kb (20). Thousands of molecules can be driven past the detectors in a matter of minutes, and summing the resulting fluorescent burst traces results in a physical map of target motifs. This suggests a promising technique for rapid genetic fingerprinting of non-amplified samples.

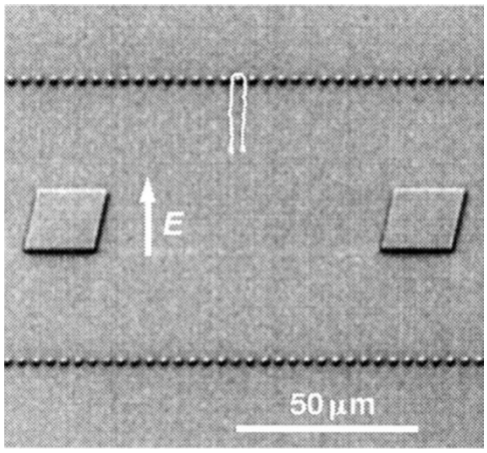

Figure 8. Scanning electron micrograph of a thin slit microfabricated array. A cartoon DNA molecule it shown hooked over a post in a symmetric U shape – the configuration in which extension was measured. Figure reprinted with permission (74).

Nanochannels

For long molecules and channel diameters ranging from tens to hundreds of *nm*, confinement induced stretching results in uniform elongation along the molecule and a simple linear relationship between contour length and projected length along the channel axis (17). Thus, given proper calibration, it is straightforward to determine absolute length for a range of fragment sizes. Furthermore, the flexibility of the

polymer and the presence of thermal agitation work in favor of high resolution length measurements. Consider that for an ensemble of identically sized DNA molecules, all having been elongated and fixed to a surface by the same process, there exists a distribution of stretched lengths. Because they are fixed, to obtain statistically independent measurements of the extended length, multiple molecules must be observed. DNA in a nanochannel fluctuates rapidly however, allowing many independent measurements to be made on a single molecule. For the above reasons, a genomic length DNA molecule can be extended and observed in a nanofluidic channel, and its length can be determined with high accuracy.

A general dependence of resolving power, R, on length, L, and channel diameter, D, (eq. 1) demonstrates that while resolution decreases for shorter molecules, this effect may be offset by shrinking channel size (17).

$$R \propto \frac{\sqrt{L}}{D^{5/6}} \qquad \textbf{Eq 1.}$$

Because of this, efforts to fabricate smaller channels have dominated the field of nanofluidics. Among the patterning methods used are electron-beam lithography (52,53), and nanoimprint lithography (54), both of which have been combined with novel methods for shrinking and sealing channels (55-63). Non-lithographic approaches to patterning, such as focused ion beam (FIB) machining and electrospinning sacrificial polymers have also been used (64-66). With some effort, working fluidic channels as small as $10-20nm$ in diameter have been made (54). In our lab, we are investigating the use of novel sacrificial materials for sub-$20nm$ slits and channels. As cavity dimensions approach 10's of nm and less, the scaling law described above begins to break down for double stranded DNA. In this regime of

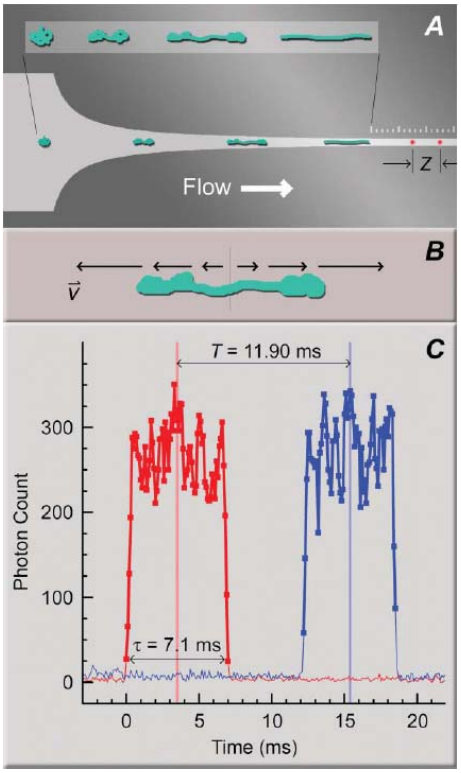

Figure 9. (A) Depiction of a device which hydrodynamically stretches and detects DNA molecules. Laser spots are separated by a distance, z, along the detection channel. Note that the main utility of the slit depth used here is to create allow quasi-2D shear flow, and to confine molecules to the focal plane, as opposed to inducing contour deformation. The green shapes represent DNA molecules in various stretched states. (**B)** Diagram depicting fluid velocity relative to the center of a DNA molecule. (**C)** Data generated by detection of intercalating dye on the backbone of a single DNA molecule. Though not depicted here, one can envision a third laser spot of a different color exciting fluorescence from hybridized probe molecules. Figure reprinted with permission (21).

smaller channels, there is still much work to be done modeling DNA dynamics. A good initial effort has been made for channels down to $25nm$ in diameter (figure 10) (16).

As a consequence of real time length measurements, DNA molecules can be visualized as they undergo digestion by restriction enzymes, (figure 11) (19). After an enzymatic cofactor enters the nanochannel, fragments are cut by the already present enzymes and drift apart allowing for immediate length measurements. Furthermore, because fragment order is maintained this method provides direct knowledge of cut position.

If global confinement results in a uniform decrease in entropy across the length of a DNA strand, then it is expected that unevenly localized confinement creates a gradient in free energy. As evidence of this, DNA molecules straddling the interface between two nanofabricated regions spontaneously retract into the region which offers more accessible configuration space to the polymer (69). This “entropic recoil” effect causes a center of mass motion and is distinct from entropic elasticity. It can be used in conjunction with an electrophoretic driving force (figure 12) as a method for identifying knots and folds, selectively straightening folded molecules (70), and sorting molecules according to size (71).

While it is hard to imagine a method for tightly compacting DNA in three dimensions using conventional techniques, it can be achieved using pore-like constriction within a nanochannel (15). A molecule can be electrophoretically driven against a constriction, highly compressing it (figure 13). Analysis of the ensuing expansion provides new

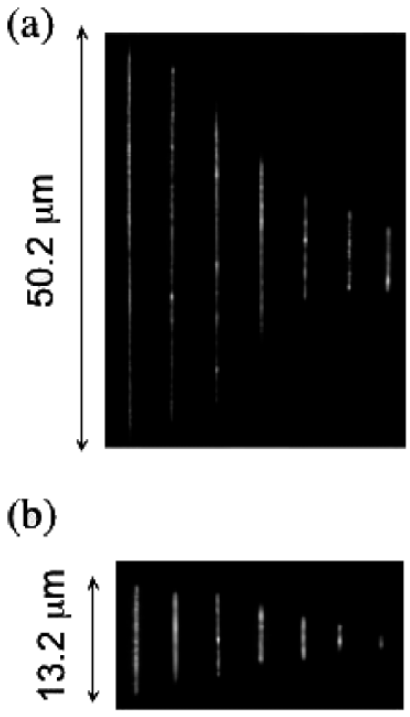

Figure 10. (a) Averaged intensity of selected T2 DNA molecules in 30×40 nm, 60×80 nm, 80×80 nm, 140×130 nm, 230×150 nm, 300×440 nm, and 440×440 nm channels (left to right). **(b)** Averaged intensity of selected λ-DNA molecules in the same channels. Figure reprinted with permission (16).

data with which to test polymer models and may have direct biophysical relevance with regard to DNA compaction into bacteriophage heads. Also of biological relevance are other protein-DNA interactions such as promoter binding. Because elongation within a channel depends on polymer flexibility, interactions which are known to induce strain can be studied (67,68).

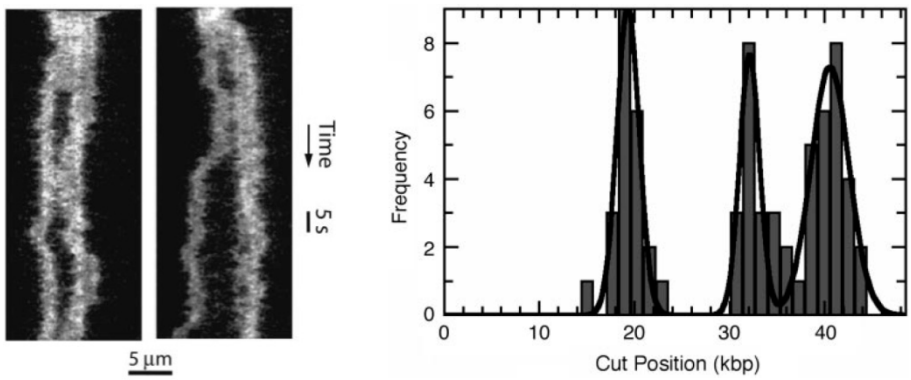

Figure 11. (Left) Intensity trace of DNA molecule in a nanochannel as it is cut with a restriction enzyme. The horizontal dimension in this figure corresponds to a trace along the axis of the channel, and the vertical dimension corresponds to the trace through time. **(Right)** The absolute cut position of 29 molecules with two and three cuts. The line is fit to the histogram by using the sum of three Gaussian distributions. Figure reprinted with permission (19).

The combination of nanostructures which achieve both focal volume confinement and confinement induced single molecule manipulation.

For this review, we have separated nanofluidic devices into one of two classes. This was to clarify the intended, and thus far, actual uses of each type of structure. This categorization, however, is a flexible one. One could imagine that confinement would play a role for a long DNA molecule attempting to access the illumination volume at the bottom of a nanoaperture. Or that a small labeled protein detected in a 50 nm diameter channel would experience a tightly confined focal volume but feel no deforming forces. One shortcoming of the devices that have used channel confinement for decreasing focal volume to date is, regardless of the channel diameter, resolution along the axial length is determined by a diffraction limited spot.

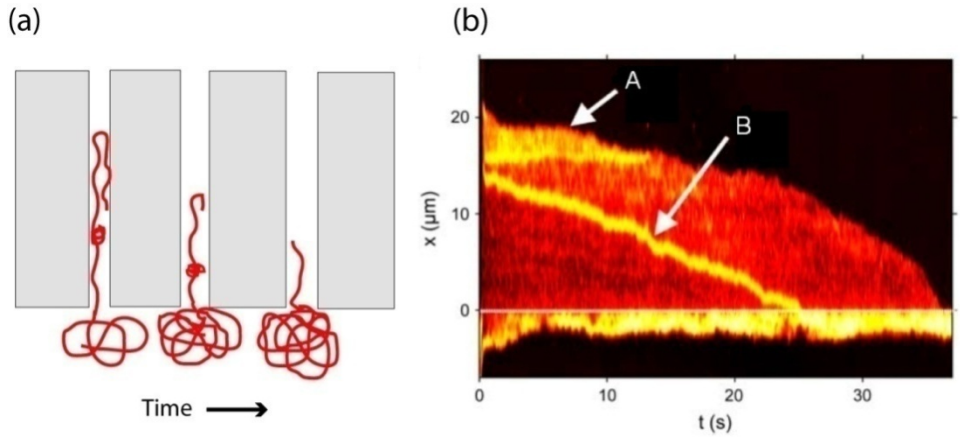

Figure 12. (a) A cartoon of a DNA molecule undergoing a combination of "recoil" and "unfolding" after being partly inserted into a nanochannel. The three drawings correspond to the shape of the molecule at three different instances in time **(b)** Intensity trace showing a molecule which simultaneously contracts and unfolds (arrow A) as it recoils from a nanochannel. This image also shows the rare case of a knot in the strand (arrow B) that does not unfold. Because any loose folds would straighten out during the recoil process, this part of the molecule must be entangled. Figures reprinted with permission (70).

One idea to address this is to fabricate slits in a thin metal film which lies just above the surface of a channel. This has been an active area of research and so far the results have been promising (48,72,73). Focusing light on the slits creates a near field point source with a resolution that depends on the slit width (figure 14). One drawback in the results obtained so far is that in the best cases only a small percentage of the incident light propagated to a point where it could interact with the sample inside of the channel. It has been suggested that this, as well as other shortcomings, could be overcome by further shrinking the fluidic channel. Thus, while there is promise for such a device, there is still much work to be done.

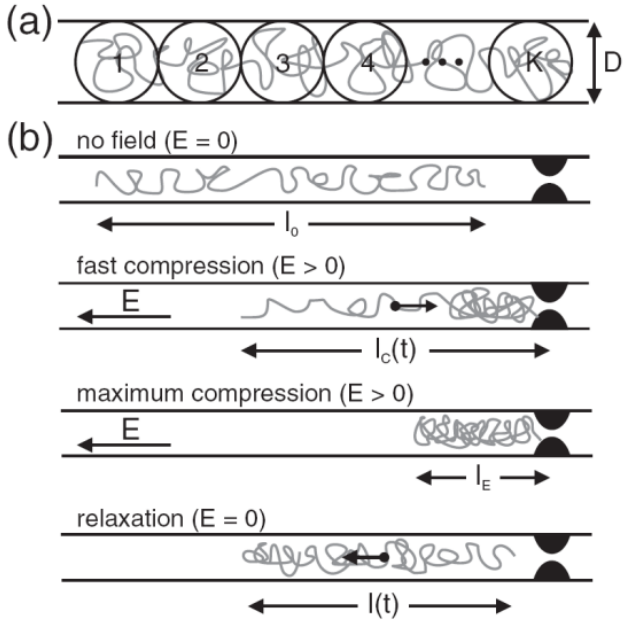

Figure 13. (a) de Gennes' **"**Blob" model of confined DNA in a channel of diameter D describing the molecule as a series of self avoiding sheres. **(b)** Experimental stages of compressing a molecule at a constriction. Figure reprinted with permission (15).

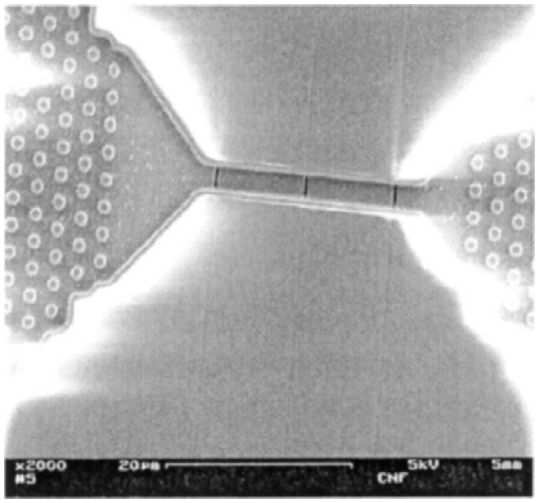

Figure 14. Scanning electron microscope image of three 100 nm wide slits and hydrodynamic channels nanofabricated into an etched quartz structure. Figure reprinted with permission (72).

Conclusion

Nanofluidic devices offer unique opportunities for probing the behavior of single biological molecules with improved resolution and sensitivity. They have been successfully employed in a number of biologically relevant experiments. Measurements for both FCS and other single molecule analysis techniques can be improved by using nanostructures to tailor the properties of a detection volume. Stretching and real-time manipulation of long DNA molecules can also be performed, showing marked improvements over previous methods for stretching and affixing molecules to surfaces for fluorescence based detection.

While prospects for novel devices are continuously being explored, there are a large number of biologically relevant experiments yet to be done using the current generation of devices. Some topics of research in our lab include detailed studies of the effect of actin filaments and microtubules on invagination of living cells into zero-mode waveguides, the use of sub-100nm channels for reliable stretching of DNA and high-throughput genetic mapping, photon counting based fragment sizing of rare DNA species, and single molecule detection of mixed analytes using molecular beacon probes in sub-100nm diameter channels.

The authors would like to thank Joshua D. Cross, Jose M. Moran-Mirabal, and Benjamin R. Cipriany for their critical evaluations.

REFERENCES

1. Medina, M. A. and P. Schwille. 2002. Fluorescence correlation spectroscopy for the detection and study of single molecules in Biology. Bioessays 24:758-764.
2. Axelrod, D., D. E. Koppel, J. Schlessinger, E. Elson, and W. W. Webb. 1976. Mobility Measurement By Analysis Of Fluorescence Photobleaching Recovery Kinetics. Biophysical Journal 16:1055-1069.
3. Axelrod, D., T. P. Burghardt, and N. L. Thompson. 1984. Total Internal-Reflection Fluorescence. Annual Review Of Biophysics And Bioengineering 13:247-268.
4. Trautman, J. K., J. J. Macklin, L. E. Brus, and E. Betzig. 1994. Near-Field Spectroscopy Of Single Molecules At Room-Temperature. Nature 369:40-42.
5. Xie, X. S. and R. C. Dunn. 1994. Probing Single-Molecule Dynamics. Science 265:361-364.
6. Mertz, J., C. Xu, and W. W. Webb. 1995. Single-molecule detection by two-photon-excited fluorescence. Optics Letters 20:2532-2534.
7. Webb, W. W. 2006. Commentary on the pleasures of solving impossible problems of experimental physiology. Annual Review Of Physiology 68:1-28.
8. Berland, K. M., P. T. C. So, and E. Gratton. 1995. 2-Photon Fluorescence Correlation Spectroscopy - Method And Application To The Intracellular Environment. Biophysical Journal 68:694-701.
9. Levene, M. J., J. Korlach, S. W. Turner, M. Foquet, H. G. Craighead, and W. W. Webb. 2003. Zero-mode waveguides for single-molecule analysis at high concentrations. Science 299:682-686.
10. Samiee, K. T., M. Foquet, L. Guo, E. C. Cox, and H. G. Craighead. 2005. lambda-repressor oligomerization kinetics at high concentrations using

fluorescence correlation spectroscopy in zero-mode waveguides. Biophysical Journal 88:2145-2153.

11. Samiee, K. T., J. M. Moran-Mirabal, Y. K. Cheung, and H. G. Craighead. 2006. Zero mode waveguides for single-molecule spectroscopy on lipid membranes. Biophysical Journal 90:3288-3299.
12. Stavis, S. M., J. B. Edel, Y. G. Li, K. T. Samiee, D. Luo, and H. G. Craighead. 2005. Single-molecule mobility and spectral measurements in submicrometer fluidic channels. Journal Of Applied Physics 98.
13. Stavis, S. M., J. B. Edel, Y. G. Li, K. T. Samiee, D. Luo, and H. G. Craighead. 2005. Detection and identification of nucleic acid engineered fluorescent labels in submicrometre fluidic channels. Nanotechnology 16:S314-S323.
14. Foquet, M., J. Korlach, W. Zipfel, W. W. Webb, and H. G. Craighead. 2002. DNA fragment sizing by single molecule detection in submicrometer-sized closed fluidic channels. Analytical Chemistry 74:1415-1422.
15. Reccius, C. H., J. T. Mannion, J. D. Cross, and H. G. Craighead. 2005. Compression and free expansion of single DNA molecules in nanochannels. Physical Review Letters 95.
16. Reisner, W., K. J. Morton, R. Riehn, Y. M. Wang, Z. N. Yu, M. Rosen, J. C. Sturm, S. Y. Chou, E. Frey, and R. H. Austin. 2005. Statics and dynamics of single DNA molecules confined in nanochannels. Physical Review Letters 94.

17. Tegenfeldt, J. O., C. Prinz, H. Cao, S. Chou, W. W. Reisner, R. Riehn, Y. M. Wang, E. C. Cox, J. C. Sturm, P. Silberzan, and R. H. Austin. 2004. The dynamics of genomic-length DNA molecules in 100-nm channels. Proceedings Of The National Academy Of Sciences Of The United States Of America 101:10979-10983.

18. Bakajin, O. B., T. A. J. Duke, C. F. Chou, S. S. Chan, R. H. Austin, and E. C. Cox. 1998. Electrohydrodynamic stretching of DNA in confined environments. Physical Review Letters 80:2737-2740.

19. Riehn, R., M. C. Lu, Y. M. Wang, S. F. Lim, E. C. Cox, and R. H. Austin. 2005. Restriction mapping in nanofluidic devices. Proceedings Of The National Academy Of Sciences Of The United States Of America 102:10012-10016.

20. Chan, E. Y., N. M. Goncalves, R. A. Haeusler, A. J. Hatch, J. W. Larson, A. M. Maletta, G. R. Yantz, E. D. Carstea, M. Fuchs, G. G. Wong, S. R. Gullans, and R. Gilmanshin. 2004. DNA mapping using microfluidic stretching and single-molecule detection of fluorescent site-specific tags. Genome Research 14:1137-1146.

21. Larson, J. W., G. R. Yantz, Q. Zhong, R. Charnas, C. M. D'Antoni, M. V. Gallo, K. A. Gillis, L. A. Neely, K. M. Phillips, G. G. Wong, S. R. Gullans, and R. Gilmanshin. 2006. Single DNA molecule stretching in sudden mixed shear and elongational microflows. Lab On A Chip 6:1187-1199.

22. Phillips, K. M., J. W. Larson, G. R. Yantz, C. M. D'Antoni, M. V. Gallo, K. A. Gillis, N. M. Goncalves, L. A. Neely, S. R. Gullans, and R. Gilmanshin. 2005. Application of single molecule technology to rapidly map long DNA and study the conformation of stretched DNA. Nucleic Acids Research 33:5829-5837.

23. Braslavsky, I., B. Hebert, E. Kartalov, and S. R. Quake. 2003. Sequence information can be obtained from single DNA molecules. Proceedings Of The National Academy Of Sciences Of The United States Of America 100:3960-3964.

24. Korlach, J., M. Levene, M. Foquet, S. W. Turner, H. G. Craighead, and W. W. Webb. 2003. Single molecule DNA sequence profiling in zero-mode

waveguides using gamma-phosphate linked nucleotide analogs. Biophysical Journal 84:141A-141A.

25. Korlach, J., M. Levene, S. W. Turner, H. G. Craighead, and W. W. Webb. 2002. Single molecule analysis of DNA polymerase activity using zero-mode waveguides. Biophysical Journal 82:507A-507A.

26. Kahya, N. and P. Schwille. 2006. Fluorescence correlation studies of lipid domains in model membranes (Review). Molecular Membrane Biology 23:29-39.

27. Sako, Y. and T. Yanagida. 2003. Single-molecule visualization in cell biology. Nature Cell Biology:SS1-SS5.

28. Wenger, J., H. Rigneault, J. Dintinger, D. Marguet, and P. F. Lenne. 2006. Single-fluorophore diffusion in a lipid membrane over a subwavelength aperture. Journal Of Biological Physics 32:SN1-SN4.

29. Edel, J. B., M. Wu, B. Baird, and H. G. Craighead. 2005. High spatial resolution observation of single molecule dynamics in living cell membranes using zero mode waveguides. Biophysical Journal 88:195A-195A.

30. Foquet, M., J. Korlach, W. R. Zipfel, W. W. Webb, and H. G. Craighead. 2004. Focal volume confinement by submicrometer-sized fluidic channels. Analytical Chemistry 76:1618-1626.

31. Stavis, S. M., J. B. Edel, K. T. Samiee, and H. G. Craighead. 2005. Single molecule studies of quantum dot conjugates in a submicrometer fluidic channel. Lab On A Chip 5:337-343.

32. Riemer, S. C. and V. A. Bloomfield. 1978. Packaging Of Dna In Bacteriophage Heads - Some Considerations On Energetics. Biopolymers 17:785-794.

33. Smith, D. E., S. J. Tans, S. B. Smith, S. Grimes, D. L. Anderson, and C. Bustamante. 2001. The bacteriophage phi 29 portal motor can package DNA against a large internal force. Nature 413:748-752.

34. Bustamante, C., S. B. Smith, J. Liphardt, and D. Smith. 2000. Single-molecule studies of DNA mechanics. Current Opinion In Structural Biology 10:279-285.

35. Smith, S. B., L. Finzi, and C. Bustamante. 1992. Direct Mechanical Measurements Of The Elasticity Of Single Dna-Molecules By Using Magnetic Beads. Science 258:1122-1126.

36. Perkins, T. T., D. E. Smith, and S. Chu. 1997. Single polymer dynamics in an elongational flow. Science 276:2016-2021.

37. Larson, R. G., T. T. Perkins, D. E. Smith, and S. Chu. 1997. Hydrodynamics of a DNA molecule in a flow field. Physical Review E 55:1794-1797.

38. Minc, N., P. Bokov, K. B. Zeldovich, C. Futterer, J. L. Viovy, and K. D. Dorfman. 2005. Motion of single long DNA molecules through arrays of magnetic columns. Electrophoresis 26:362-375.

39. Randall, G. C. 2006. Collision of a DNA Polymer with a Small Obstacle. Macromolecules.

40. Randall, G. C. and P. S. Doyle. 2004. Electrophoretic collision of a DNA molecule with an insulating post. Physical Review Letters 93.

41. Fu, J. P., J. Yoo, and J. Y. Han. 2006. Molecular sieving in periodic free-energy landscapes created by patterned nanofilter arrays. Physical Review Letters 97.

42. Kaji, N., Y. Tezuka, Y. Takamura, M. Ueda, T. Nishimoto, H. Nakanishi, Y. Horiike, and Y. Baba. 2004. Separation of long DNA molecules by quartz nanopillar chips under a direct current electric field. Analytical Chemistry 76:15-22.

43. Lin, Y. W., M. F. Huang, and H. T. Chang. 2005. Nanomaterials and chip-based nanostructures for capillary electrophoretic separations of DNA. Electrophoresis 26:320-330.

44. Han, J. Y. and H. G. Craighead. 2002. Characterization and optimization of an entropic trap for DNA separation. Analytical Chemistry 74:394-401.

45. Han, J. and H. G. Craighead. 2000. Separation of long DNA molecules in a microfabricated entropic trap array. Science 288:1026-1029.

46. Huang, L. R., E. C. Cox, R. H. Austin, and J. C. Sturm. 2003. Tilted Brownian ratchet for DNA analysis. Analytical Chemistry 75:6963-6967.

47. Cabodi, M., Y. F. Chen, S. W. P. Turner, H. G. Craighead, and R. H. Austin. 2002. Continuous separation of biomolecules by the laterally asymmetric diffusion array with out-of-plane sample injection. Electrophoresis 23:3496-3503.

48. Austin, R. H., J. O. Tegenfeldt, H. Cao, S. Y. Chou, and E. C. Cox. 2002. Scanning the controls: Genomics and nanotechnology. Ieee Transactions On Nanotechnology 1:12-18.

49. Maier, B. and J. O. Radler. 1999. Conformation and self-diffusion of single DNA molecules confined to two dimensions. Physical Review Letters 82:1911-1914.

50. Anselmi, C., P. DeSantis, and A. Scipioni. 2005. Nanoscale mechanical and dynamical properties of DNA single molecules. Biophysical Chemistry 113:209-221.

51. Herrick, J. and A. Bensimon. 1999. Imaging of single DNA molecule: Applications to high-resolution genomic studies. Chromosome Research 7:409-423.

52. Riehn, R., R. H. Austin, and J. C. Sturm. 2006. A nanofluidic railroad switch for DNA. Nano Letters 6:1973-1976.

53. Riehn, R. and R. H. Austin. 2006. Wetting micro- and nanofluidic devices using supercritical water. Analytical Chemistry 78:5933-5934.

54. Cao, H., Z. N. Yu, J. Wang, J. O. Tegenfeldt, R. H. Austin, E. Chen, W. Wu, and S. Y. Chou. 2002. Fabrication of 10 nm enclosed nanofluidic channels. Applied Physics Letters 81:174-176.

55. Harnett, C. K., K. M. Satyalakshmi, G. W. Coates, and H. G. Craighead. 2002. Direct electron-beam patterning of surface coatings and sacrificial layers for micro-total analysis systems. Journal Of Photopolymer Science And Technology 15:493-496.

56. Harnett, C. K., G. W. Coates, and H. G. Craighead. 2001. Heat-depolymerizable polycarbonates as electron beam patternable sacrificial layers for nanofluidics. Journal Of Vacuum Science & Technology B 19:2842-2845.

57. Turner, S. W., A. M. Perez, A. Lopez, and H. G. Craighead. 1998. Monolithic nanofluid sieving structures for DNA manipulation. Journal Of Vacuum Science & Technology B 16:3835-3840.

58. Han, A. P., N. F. de Rooij, and U. Staufer. 2006. Design and fabrication of nanofluidic devices by surface micromachining. Nanotechnology 17:2498-2503.

59. Dumond, J. J., H. Y. Low, and I. Rodriguez. 2006. Isolated, sealed nanofluidic channels formed by combinatorial-mould nanoimprint lithography. Nanotechnology 17:1975-1980.

60. Zeng, H. J., Z. L. Wang, and A. D. Feinerman. 2006. Fabrication of micro/nano fluidic channels with sacrificial galvanic coupled metals. Nanotechnology 17:3183-3188.

61. Kang, S. M., B. Park, I. S. Nam, C. H. Lim, H. Ju, and S. B. Lee. 2006. Fabrication of on-chip nanofluidic channels by using sacrificial photoresist ternplated SiO2 sputter deposition. Journal Of The Korean Physical Society 48:883-887.

62. Li, W. L., J. O. Tegenfeldt, L. Chen, R. H. Austin, S. Y. Chou, P. A. Kohl, J. Krotine, and J. C. Sturm. 2003. Sacrificial polymers for nanofluidic channels in biological applications. Nanotechnology 14:578-583.

63. Melechko, A. V., T. E. McKnight, M. A. Guillorn, V. I. Merkulov, B. Ilic, M. J. Doktycz, D. H. Lowndes, and M. L. Simpson. 2003. Vertically aligned carbon nanofibers as sacrificial templates for nanofluidic structures. Applied Physics Letters 82:976-978.

64. Campbell, L. C., M. J. Wilkinson, A. Manz, P. Camilleri, and C. J. Humphreys. 2004. Electrophoretic manipulation of single DNA molecules in nanofabricated capillaries. Lab On A Chip 4:225-229.

65. Verbridge, S. S., J. B. Edel, S. M. Stavis, J. M. Moran-Mirabal, S. D. Allen, G. Coates, and H. G. Craighead. 2005. Suspended glass nanochannels coupled with microstructures for single molecule detection. Journal Of Applied Physics 97.

66. Czaplewski, D. A., J. Kameoka, R. Mathers, G. W. Coates, and H. G. Craighead. 2003. Nanofluidic channels with elliptical cross sections formed using a nonlithographic process. Applied Physics Letters 83:4836-4838.

67. Wang, Y. M., J. O. Tegenfeldt, W. Reisner, R. Riehn, X. J. Guan, L. Guo, I. Golding, E. C. Cox, J. Sturm, and R. H. Austin. 2005. Single-molecule studies of repressor-DNA interactions show long-range interactions. Proceedings Of The National Academy Of Sciences Of The United States Of America 102:9796-9801.

68. Wang, Y. M., J. O. Tegenfeldt, J. Sturm, and R. H. Austin. 2005. Long-range interactions between transcription factors. Nanotechnology 16:1993-1999.

69. Turner, S. W. P., M. Cabodi, and H. G. Craighead. 2002. Confinement-induced entropic recoil of single DNA molecules in a nanofluidic structure. Physical Review Letters 88.

70. Mannion, J. T., C. H. Reccius, J. D. Cross, and H. G. Craighead. 2006. Conformational analysis of single DNA molecules undergoing entropically induced motion in nanochannels. Biophysical Journal 90:4538-4545.

71. Cabodi, M., S. W. P. Turner, and H. G. Craighead. 2002. Entropic recoil separation of long DNA molecules. Analytical Chemistry 74:5169-5174.

72. Tegenfeldt, J. O., O. Bakajin, C. F. Chou, S. S. Chan, R. Austin, W. Fann, L. Liou, E. Chan, T. Duke, and E. C. Cox. 2001. Near-field scanner for moving molecules. Physical Review Letters 86:1378-1381.

73. Tegenfeldt, J. O., C. Prinz, H. Cao, R. L. Huang, R. H. Austin, S. Y. Chou, E. C. Cox, and J. C. Sturm. 2004. Micro- and nanofluidics for DNA analysis. Analytical And Bioanalytical Chemistry 378:1678-1692.

74. Bustamante, C. 1991. Direct Observation And Manipulation Of Single Dna-Molecules Using Fluorescence Microscopy. Annual Review Of Biophysics And Biophysical Chemistry 20:415-446.

CHAPTER 4

CONFORMATIONAL ANALYSIS OF SINGLE DNA MOLECULES UNDERGOING ENTROPICALLY INDUCED MOTION IN NANOCHANNELS*

***Previously published article: Biophysical Journal 2006, Volume 90, Issue 12, pg. 4538**

J. T. Mannion, C. H. Reccius, J. D. Cross and H. G. Craighead

School of Applied and Engineering Physics, Cornell University, Ithaca, NY 14853

We have used the interface between a nanochannel and a microchannel as a tool for applying controlled forces on a DNA molecule. A molecule, with a radius of gyration larger than the nanochannel width, that straddles such an interface is subject to an essentially constant entropic force, which can be balanced against other forces such as the electrophoretic force from an applied electric field. By controlling the applied field we can position the molecule as desired and observe the conformation of the molecule as it stretches, relaxes and recoils from the nanochannel. We quantify and present models for the molecular motion in response to the entropic, electrophoretic, and frictional forces acting on it. By determining the magnitude of the drag coefficients for DNA molecules in the nanostructure, we are able to estimate the confinement induced recoil force. Finally, we demonstrate that we can use a controlled applied field and the entropic interfacial forces to unfold molecules, which can then be manipulated and positioned in their simple extended morphology.

Introduction

The dynamics of DNA in nanochannels is a relevant topic considering the current efforts toward the development of micro- and nanofluidic devices for biomolecular analysis. In previous years, such devices have been studied for their ability to isolate, manipulate and investigate single biomolecules. Among the technologies tested have been entropic trap arrays (1-4), micro- and nanopillar arrays (5-9), nanopores (10-14) and nanochannels (15-18). Each has shown promise as either a tool for the analysis of statistical mechanical properties of long biopolymers or as a tool for sorting biomolecules according to their length. For example, the contour lengths of molecules that were driven into a 100 nm channel have been measured by Tegenfeldt et al. (16). They were able to determine the length of a single λ-DNA strand to within 400 bp in 1 min. Using nanochannels it is also possible to observe the action of an enzyme on a single DNA molecule and consequently map its restriction sites (17).

It has been demonstrated that DNA molecules inserted partly into a nanopillar array with an applied electric field experienced a confinement-induced entropic force, causing them to recoil from the array, when the field was turned off (8). This effect, termed entropic recoil, was used to sort two DNA populations of different lengths with a resolution of 11% by length (7). The resolution of pillar arrays is blurred by the fact that DNA molecules entering the array at a distinct point may enter the array diagonally, wrap around pillars or even form sideways loops. All these different conformations probably have different friction and lead to different recoil times. We have therefore investigated entropic recoil from nanochannels, a geometry which allows only one direction of insertion. Nanochannels also simplify the optical analysis

(17) and allow a better comparison to well known theoretical models like de Gennes' blob model for confined polymers (19).

Here, for the first time, we investigate the motion and conformation of single DNA molecules in $100nm$ channels while they are manipulated with both electric fields and confinement induced entropic forces. Figure 1A illustrates the recoil experiment. In addition to the basic recoil process we investigate several new types of motion in nanochannels. Sometimes as shown in Figure 1B, when a molecule is electrophoretically driven into a nanochannel, its leading end is folded over on itself. We show that in our experiments the looped DNA strands can be unfolded by the recoil process. Note that folding of DNA has already been observed as quantized resistance changes during DNA translocation through artificial nanopores (12,20). The term "folded DNA" just refers to a transient loop formation and should not be confused with protein folding, for example.

The entropic recoil force was shown to be mathematically distinct from an elastic restoring force (8). A molecule undergoing entropic recoil speeds up over time. In contrast, one expects that the contraction due to entropic elasticity would slow down over time. Here we cause molecules to undergo either elastic contraction or entropic recoil. Figure 1C illustrates the contraction of a stretched molecule inside a nanochannel. As shown in Figure 1D, we also demonstrate that under certain initial conditions it is possible for a molecule to undergo both the contraction and entropic recoil processes simultaneously.

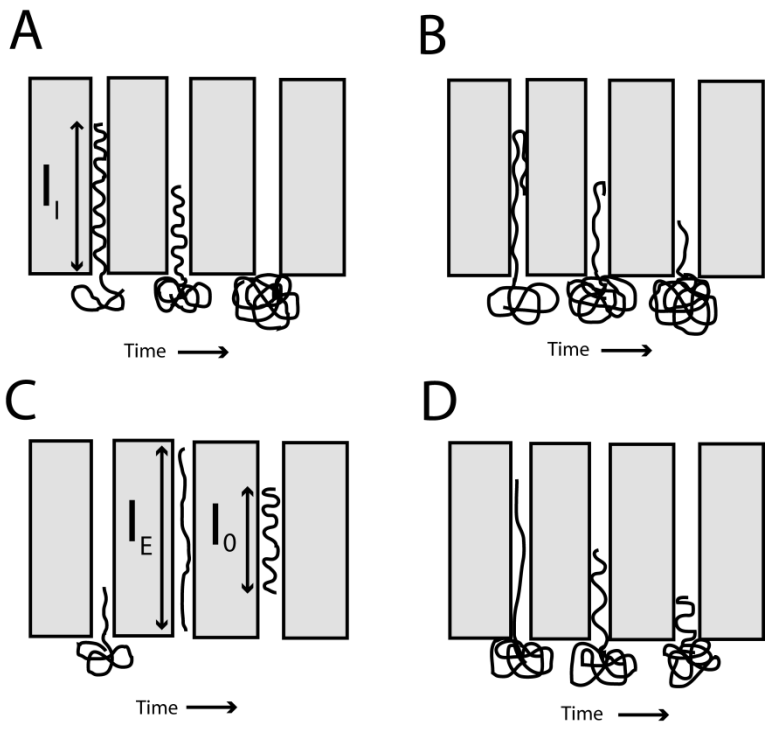

Figure 1. Types of Motion and Conformations Studied. Relaxed DNA molecules in nanochannels have an equilibrium extension length. **(A)** Extraction of a relaxed strand from a nanochannel. The entropic force driving the extraction is due to the difference in configuration space on either side of the nanochannel/microchannel interface. This process of self extraction, which only occurs for molecules straddling the interface, is called a recoil process. **(B)** In some cases molecules are inserted in the nanochannels with their leading end folded over on itself, creating a loop. During the recoil process these molecules unfold, which means the looped section of DNA straightens. **(C)** A molecule electrophoretically driven into the nanochannel stretches as the entropic and electric forces pull on the molecule in opposite directions. After the molecule has entirely entered the nanochannel, the electric field is switched off and it is allowed to relax to its equilibrium extension length l_0. **(D)** If a molecule is partially driven into a nanochannel and immediately allowed to recoil, it will show a combination of unstretching and recoiling.

A basic theory (8) can be derived by neglecting the self-avoidance effects of the persistent DNA. A molecule at the interface has the entropy per unit length s_I inside the nanochannel and entropy per unit length s_M in the microchannel. Thus the entropy is $S = l_I s_I + l_M s_M$ where l_I and l_M are the lengths in the two regions. The length of the molecule which resides in the microchannel can be rewritten as $l_M = l_0 - l_I$ where l_0 is the full extended length of the DNA strand in the nanochannel. The entropic force $f = dF / dl_I = T(s_I - s_M)$ results from the free energy $F = U - TS$ and is found to be independent of the inserted length l_I inside the nanochannel. The molecule retraction at velocity $v = dl_I / dt$ is only hindered by the hydrodynamic drag force $f_D = \rho l_I v$ inside a confined environment (21). Here ρ is the hydrodynamic drag per unit extended length in the nanochannel. Solving the resulting differential equation $f = \rho l_I dl_I / dt$ under the condition $l_I(t_0) = 0$ leads to:

$$l_I(t) = \sqrt{-\frac{f}{\rho}(t - t_0)} \qquad (1)$$

where t_0 is the time of complete extraction.

Materials and Methods

Device Fabrication. Devices were patterned on a mirror-polished fused silica wafer with a thickness of $500\mu m$ (MarkOptics, Santa Ana, CA) using a combination of electron beam and optical lithography. Initially, a layer of gold, $25nm$ thick, was evaporated onto poly(methyl-methacrylate) electron-beam resist to help draw current during the electron-beam process. Negative patterns of the nanochannel regions were exposed using a JBX-9300FS electron beam lithography system (JEOL, Peabody, MA). After removal of gold and PMMA development, the patterns were transferred to

a Cr mask by evaporation and liftoff. Microchannel patterns were then added to the mask using optical lithography and the same lift off process. Both micro- and nanochannels were etched simultaneously using a Plasmalab 80Plus REI (Oxford Instruments, Eynsham, UK) with a CHF_3/O_2 mixture at 50 Watts for 20 min. Access holes were created by alumina powder blasting from the backside of the wafer. Finally a $170\mu m$ fused silica cover wafer (MarkOptics) was touch bonded and annealed at 1050°C to the device wafer, enclosing the channels. Nanoports (Upchurch Scientific, Oak Habor, WA) were sealed to the access holes forming buffer reservoirs. A schematic of the completed device can be seen in Figure 2. Several electron micrographs of the nanostructures before bonding are shown in Figure 3.

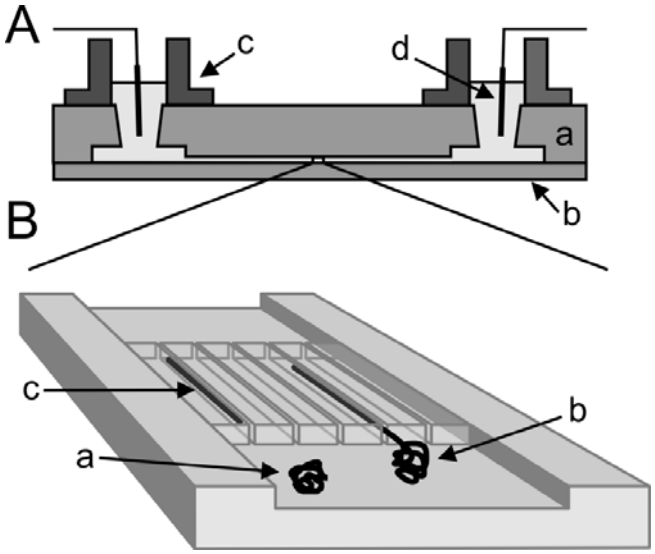

Figure 2. Schematic of the nanochannel array device. **(A)** Cross section of device consisting of two bonded fused silica wafers (a, b) with the upper one containing the structure. The microchannel was contacted from the top of the device and fluid reservoirs (c) were attached. Electrical connections to the channel were made by platinum electrodes (d). **(B)** Close-up of the nanochannel array in the upper wafer. DNA molecules have been drawn in the loading zone (a), as they enter a nanochannel (b), and in an elongated equilibrium conformation in a nanochannel (c).

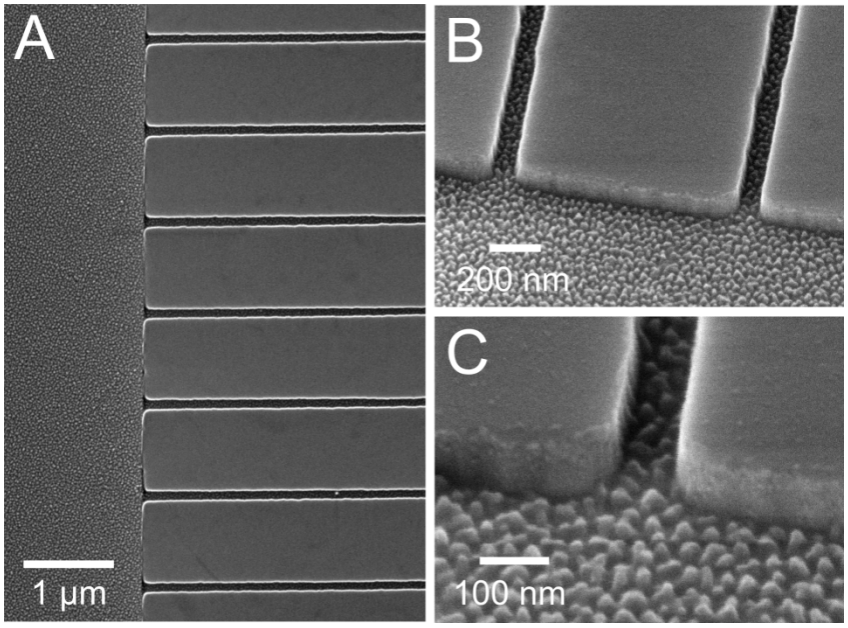

Figure 3. Electron micrograph of nanochannel array etched into $500\mu m$ fused silica wafer. **(A)** Top down view showing the interface between the microchannel and the array of nanochannels. Both were etched $100nm$ deep. **(B)** Entrance to two nanochannels. The channels are $90nm$ wide. The wall separating the two channels is $910nm$ wide. **(C)** Closer view of a nanochannel entrance. Floor roughness is $10 - 20nm$ and is attributed to the etching process.

DNA and Buffer Preparation. T4-bacteriophage DNA molecules (Wako, Richmond, VA) were stained with the bis-intercalating dye YOYO-1 (Molecular Probes, Eugene, OR) and used at a concentration of $6\mu g / ml$. The contour length of single T4-DNA (169kbp) can be calculated from the base pair spacing of $0.34nm$ to $L_{T4} = 57.4\mu m$. But recent studies have shown that the dye TOTO-1, which is similar to YOYO-1, increases the contour length L_{T4} by 30-35% at a dye to base pair ratio of 1:4 (21,22). Thus at our dye ratio of 1:5 L_{T4} is expected to rise by 23% to $70.7\mu m$. Although in the past, the persistence length of the DNA was assumed to increased from $51nm$

when stained (21,22), recent investigations indicate that staining reduces the persistence length to $12nm$ (23). The two protonated amino and two protonated imino groups of YOYO-1 also decrease the average charge of the negative DNA backbone. Given our buffer concentrations, we assume a counter ion shielding of 60% (24,25) and calculate a charge per unit length of $\lambda = 1.1e_0 / nm$. As changes in the properties are all less than an order of magnitude, we expect that the behavior of unstained DNA would be similar to the observed dynamics of the DNA/dye complex. The buffer consisted of 445 mM Tris-borate and 10 mM EDTA (5xTBE, pH 8.3, Sigma, St. Louis, MO) with 5% (v/v) β-mercaptoethanol (Sigma) as an antiphotobleaching agent and 2.5% (w/w) poly(n-vinylpyrrolidone) (PVP, MW 10,000, Sigma) to reduce both electroosmotic flow and unspecific binding of DNA to channel walls (18,26,27). Electrical contact was made with platinum electrodes inserted into the reservoirs.

Microscopy. The individual molecules were observed with an IX70 inverted microscope (Olympus, Melville, NY), which was equipped with a 100x/0.93 NA oil immersion objective (Olympus) and illuminated by a 100W mercury arc lamp. An XF100 filter set (Omega Optical, Brattleboro, VT) was used for fluorescence imaging. Images were acquired using an ICCD-350F camera (Videoscope, Dulles, VA) connected to a DVD-Recorder at a rate of 29.97 frames per second. DNA molecule movement was extracted from the videos by using a combination of thresholding and morphological algorithms programmed in MATLAB (The Mathworks, Natick, MA).

Experimental Protocol. DNA molecules were driven from the reservoirs into the microchannel with a bias of 30V. In order to drive a molecule from the microchannel

into a nanochannel, a 3V bias was always applied. This bias resulted in $E = 21V/cm$ in nanochannels and $E = 2V/cm$ in the loading channel. Any further manipulations within the nanochannel were conducted under electric fields of either $21V/cm$ or $3.5V/cm$. Three types of experiments were conducted for each molecule that we observed. First, the molecules were driven entirely into the nanochannel, and the field was then switched off. Their relaxation to equilibrium extension length in the nanochannel was studied. Once they had contracted, they were slowly driven back down the nanochannel until a small portion of the molecule had reached the microchannel. At this point the field was again switched off and the molecules were observed to undergo a pure recoil process. Finally, after exiting the nanochannel, molecules were driven back in electrophoretically. This time, however, the field was switched off before the DNA strands had completely entered the nanochannel. As a result, they were observed to both recoil and unstretch simultaneously.

Results and Discussion

For each molecule, three basic investigations were performed: stretching with ensuing relaxation, relaxed recoil and stretched recoil. An example of a complete experimental time course can be seen in Figure 4 as a color coded intensity graph. The plot shows the normalized intensity along the channel axis plotted against time.

Molecule Relaxation. We investigated the relaxation of stretched molecules in a nanochannel. The DNA strands were electrophoretically driven from the microchannel into a nanochannel. Stretching was due to the electric force pulling the molecules into the nanochannel against a resistance at the entrance. The resistance at

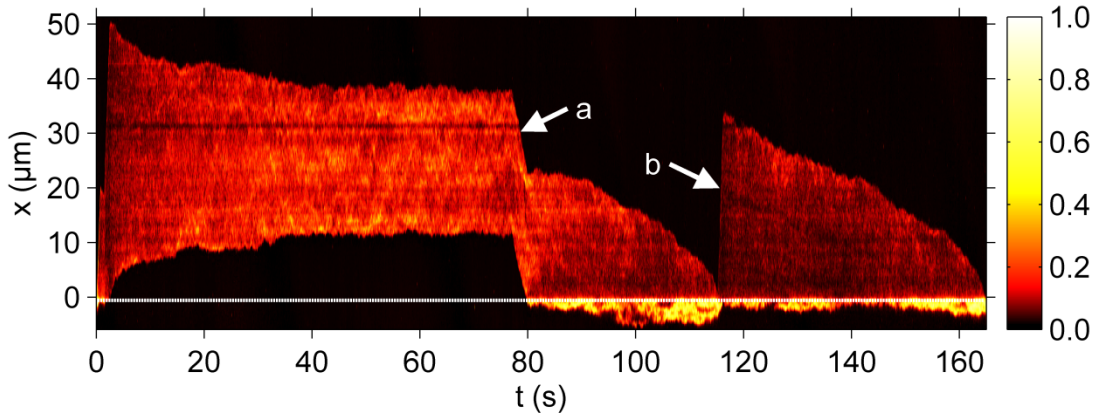

Figure 4. Intensity time trace of the three basic manipulations performed with a single T4 DNA molecule. The plot shows the normalized intensity along the channel (x-axis) versus the time t (dotted line = channel entrance). At $t = 0$ the molecule is stretched while being driven with 21 V/cm from the microchannel (x<0) into the nanochannel (x>0). It is then allowed to sit in the nanochannel and contract until it reaches its equilibrium length. At $t = 77s$ a 0.5 V/cm pulse moves the molecule to the channel entrance (a). A small part straddles the interface and the molecule begins to recoil from the nanochannel into the microchannel. At $t = 115s$, DNA is driven partially into channel with a $21V/cm$ pulse (b). When the field is turned off, it begins to both contract and recoil simultaneously. The difference between the profiles of the different molecule retraction processes can clearly be seen.

the entrance is probably due to the entropic interface force and friction for molecules encountering the entrance edges. Note that this method of stretching is completely different than those previously used such as hooking around pillars (21) or stretching by microbead techniques (28). Upon fully entering a nanochannel, a molecule begins to relax and finally reaches its equilibrium extension length inside the channel.

Though the dynamics of this contraction in nanochannels has not yet been modeled, as far as the authors are aware, DNA contraction in nanoslits was tested by Bakajin et al. (21) and treated numerically by Stigter (24). We assume that the end to end length l of a contracting molecule in a nanochannel can be roughly characterized with an exponential fitting function:

$$l(t) = l_0 + (l_E - l_0)\exp\left(-\frac{t}{\tau}\right) \qquad (2)$$

Here l_0 is the equilibrium length in the channel, l_E the measured initial extended length, and τ is the time constant of contraction. The contraction of several T4 DNA strands was fit with this function fixing l_E to the measured length at $t = 0$. The results were $l_0 = 26.4 \pm 2.6 \mu m$ and $\tau = 9.3 \pm 3.4 s$ with n = 8, where n is the number of measurements. The ratio of extension was $l_E / l_0 = 1.5 \pm 0.1$. The equilibrium extended length of λ-DNA molecules in $100 nm$ channels was measured to be $8 \mu m$ by Tegenfeldt et al (16). They also found that the extended length l_0 scales linearly with the contour length L which leads to an expected length of $28 \mu m$ for a T4 molecule. This is in close agreement with our measured value. An example of one of these fits is plotted in Figure 5. In all experiments molecules drifted at $0.6 \mu m / s$ inside the nanochannels. This was compensated for either mathematically or with an electric field offset of $0.4 V / cm$. The origin of the drift might be an electrochemical or osmotic gradient due to different DNA or dye concentrations in the fluid reservoirs.

Relaxed Recoil. After the molecules had completely relaxed to their equilibrium length inside the nanochannels, they were driven electrophoretically to the entrance of

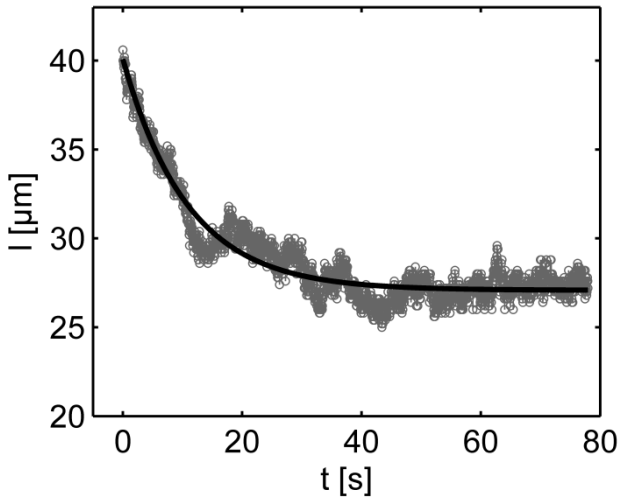

Figure 5. Plot of end to end length l versus time t for a contracting T4 molecule in a nanochannel. The molecule was stretched out by driving it electrophoretically into the channel. At $t = 0$ the field was turned off and the molecule began to contract. In order to quantify this, the function in Eq. 2 was fit to the data. Setting l_E to $40\mu m$, which is the measurement value at $t = 0$, results in $l_0 = 27.08 \pm 0.02\mu m$, $\tau = 10.9 \pm 0.1s$, and $l_E / l_0 = 1.5$.

the channels. Once the tip of the molecule was straddling the interface, the voltage was turned off and the molecules were observed to completely recoil from the nanochannel. Because molecules were allowed to reach equilibrium before beginning to recoil, this process was driven purely by the entropic recoil force and unaffected by elastic restoration. The insertion length of the molecules in the nanochannel plotted versus time shows a square root behavior which was fitted by Eq. 1. The results for the ratio of the entropic force to the drag coefficient f/ρ were $6.1 \pm 0.8\mu m^2 / s$ (n = 23) and $10.2 \pm 2.2\mu m^2 / s$ (n = 18) for molecules recoiling from the two sides of the nanochannel array. The ambient drift, responsible for the difference between the two values, can be compensated for by averaging the two, resulting in a corrected value of

$8.1 \pm 1.2 \mu m^2 / s$. In addition, a set of experiments with an electrical offset correction resulted in $f/\rho = 8.9 \pm 1.3 \mu m^2 / s$ (n = 14). Figure 6 shows this set of experiments as well as a fit to all of the curves. The theory accurately describes the data. Our values for f/ρ are three times higher than the value of $3.1 \mu m^2 / s$ determined by Turner et. al (8) for DNA recoil from nanopillar arrays. This is probably due to an increased entropic force f due the higher confinement in 100nm nanochannels compared to nanopillar arrays with 125nm spacing.

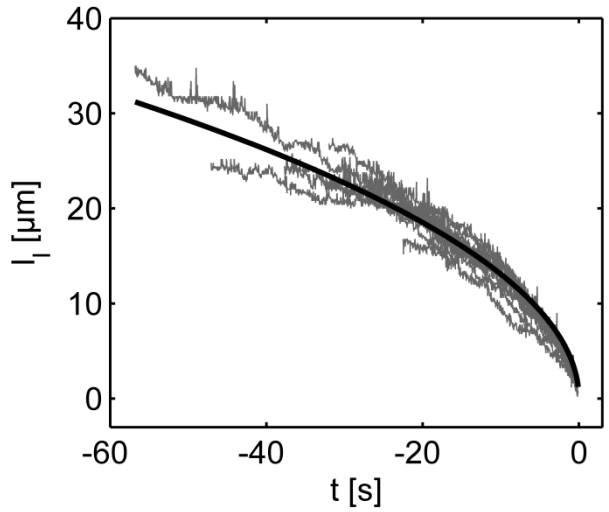

Figure 6. Plot of insertion length l_I over time t for 14 T4 DNA molecules recoiling from the nanochannel. All curves are fit together with Eq. 1. From this fit, the ratio of the entropic force to the drag coefficient was determined to be $f / \rho = 8.57 \pm 0.01 \mu m^2 / s$.

Stretched Recoil. As in the stretching experiments, molecules were electrophoretically driven from the microchannel into the nanochannels. But this time the strands were only inserted partly before the field was switched off. Under these circumstances the molecules were stretched during their entrance but were not given

the opportunity to contract before the recoil process had begun. A combined contraction and recoil was observed. A comparison between one of these combined processes and a pure recoil process can be seen in Figure 4. The difference between the two can clearly be distinguished.

In order to formulate a recoil theory that accommodates contracting, we introduce a stretching factor $\gamma(t)$, which describes the degree to which the inserted part of the molecule is stretched compared to the equilibrium extension inside our nanochannels. As in Eq. 2, we assume an exponential dependence on the time t:

$$\gamma(t) = 1 + (\gamma_0 - 1)\exp\left(-\frac{t}{\tau}\right) \qquad (3)$$

with the contraction time constant τ and the initial stretching factor $\gamma_0 = \gamma(0)$ at the beginning of the recoil. Therefore we may write, for the insertion length l_I of a molecule that begins to both recoil and contract at the instant the electric field is turned off,

$$l_I(t) = \gamma(t) \cdot \sqrt{-\frac{f}{\rho}(t - t_0)} \qquad (4)$$

which is the model that we have used to fit the data. The model treats contraction and recoiling as decoupled processes, which is a valid assumption for recoil events that last much longer than the contraction time constant τ. Figure 7 compares a stretched recoil process, with a relaxed recoil for the same molecule, in the same channel. Each has been fit using the appropriate model. As a result we obtain $f/\rho = 10.0 \pm 1.4 \mu m^2/s$ for an offset corrected set of experiments (n = 13), which is close to the value we obtained for relaxed recoil experiments. This indicates that the modified recoil model, which accounts for the entropic force as well as the stretching, is a good first approximation.

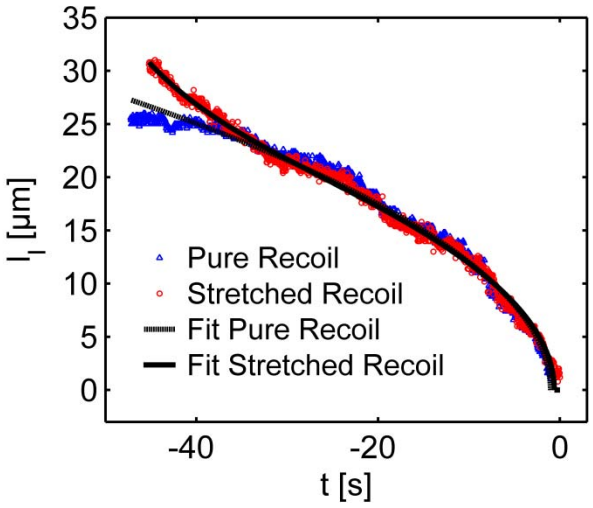

Figure 7. Demonstration of the difference between a process driven purely by the entropic recoil force and a process driven by both entropic recoil and entropic contraction. The insertion length l_I is plotted against time t. Both experiments are done with the same molecule. The curves were fit with the appropriate model (Eq. 1 or Eq. 3). As a result we obtain $f/\rho = 8.05 \pm 0.02 \mu m^2/s$ for the pure recoil event and $f/\rho = 7.50 \pm 0.04 \mu m^2/s$ for the combined process. The strand was stretched by 18% in the combined process and relaxed with a time constant of $\tau = 8.7 \pm 0.4 s$.

DNA Unfolding by Recoil. The technique of plotting normalized fluorescence intensity along the channel axis over time (17) is a powerful tool for investigating the unfolding behavior of DNA molecules. This is important for us as many of the recoil experiments showed a folded conformation upon entry, two examples of which are shown in Figure. 8. Folded portions of DNA molecules are brighter than unfolded portions in the time trace plots. The possibility that the brighter portion of the molecule has simply been compressed can be ruled out by observing its evolution through time. We would expect compressed regions to decompress and reach equilibrium with the rest of the molecule over a period of time on par with the

timescale of the observed contraction processes. Instead, the border between the bright and the dim sections does not become less defined through time. Only the observed lengths of the bright and dim portions change during the recoil process. Finally, when a certain threshold is reached the molecule suddenly becomes uniform in intensity and slightly longer. This event may correspond to the final act in an unfolding process where the energy required to bend the end of the DNA molecule is released. Note that molecules which appeared to be folded were discarded from all pure recoil and stretch-recoil measurements.

From a theoretical point of view, folded DNA molecules should be more stretched than unfolded ones due to volume exclusion effects. This implies that, for a molecule with an unfolded equilibrium extension length of l_0, the observed length will be greater than $l_0/2$ when it is folded in half. Therefore the folded configuration is entropically unfavorable in comparison with the straight configuration, so that given enough time any folded molecules should spontaneously unfold. For molecules with a significant degree of folding (more than several microns), there were no observable decreases in length of the folded segment of the molecule during our experiments. We therefore assume that spontaneous unfolding must occur over a much larger timescale than that of the unfolding process which we induce using the recoil force.

DNA Friction Determination. In order to determine hydrodynamic drag of DNA in the nanochannels, molecules were repeatedly driven by an electric field of $E = 21V/cm$ in both directions. Figure 9 shows a portion of two time traces demonstrating molecules driven in both directions. Folded molecules could easily be distinguished, and only unfolded molecules were used for velocity measurements.

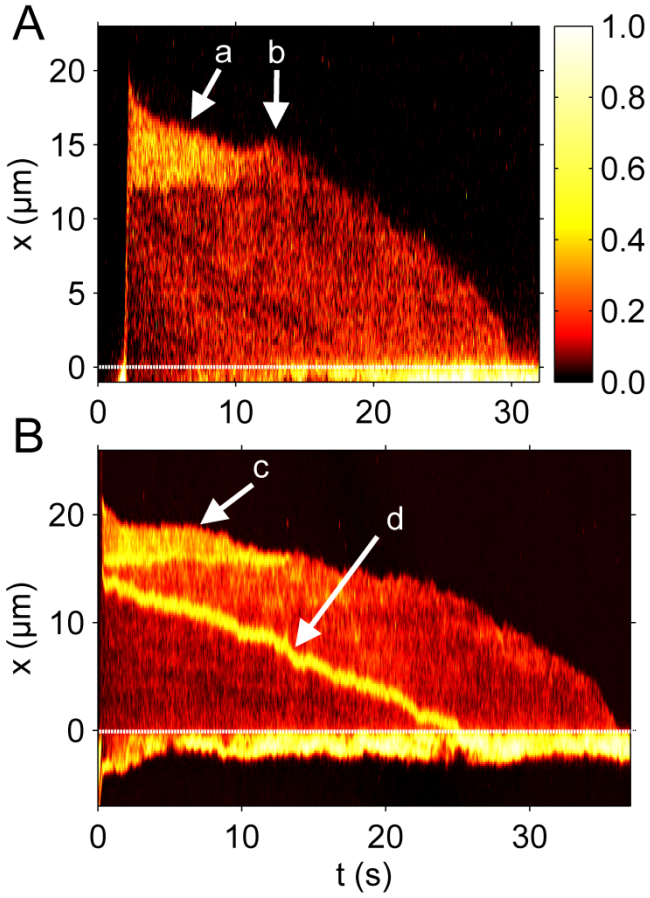

Figure 8. Intensity time traces of different types of molecule folding during recoil processes. (dotted lines = channel entrance) (**A)** A T4 DNA molecule is driven into nanochannel with a 21V/cm pulse. It immediately begins to contract and recoil. In this case however, the front end is looped (a) and unfolds over time. The molecule straightens when the folded end finally flops open (b). **(B)** Similiar to the molecule in Figure (A), this molecule contracts, recoils, and unfolds (c) simultaneously. It also shows the rare case of a knot (d) in the middle of the strand which does not unfold. Since any loose folds would straighten out during the recoil process, this part of the molecule must be entangled.

Velocities were measured by a linear fit of the molecule position versus time. Figure 10 displays the distribution of the measurement values as well as two Gaussian fits, one for each direction. The average velocity of all measurements was $v = 38.7 \pm 2.1 \mu m/s$, which corresponds to a mobility of $\mu = v/E = 1.8 \pm 0.1 \times 10^{-4} cm^2 V^{-1} s^{-1}$. This value is slightly higher than $\mu = 0.6 - 1.1 \times 10^{-4} cm^2 V^{-1} s^{-1}$ measured for λ-DNA in silicon/PDMS nanochannels (29). In these measurements an overall linear relation between velocity and electric field was measured. This linearity was also confirmed for DNA translocation through nanopores at high electric fields of the order of $10^5 V/cm$ (20). This is in agreement with theoretical models of confined polymers (30) and confined DNA (21) which predict hydrodynamic friction coefficients that are dependent on channel diameter and viscosity but not on the electric field.

The hydrodynamic friction force on a molecule is $f_{fric} = gv$ with the viscous drag coefficient g. As the channel diameter is on the order of the persistence length b, most of the hydrodynamic interactions between molecule segments are screened (21). Thus, the drag coefficient is assumed to be $g = \xi L$ with the friction coefficient per unit length ξ and the contour length L. For a non-accelerating DNA strand of charge q and charge per unit contour length λ the friction force and the electrical force $f_{elec} = qE = \lambda LE$ are in equilibrium. Therefore, the friction coefficient per unit contour length is $\xi = \lambda E/v$. Assuming a charge per unit length of $\lambda = 1.1 e_0/nm$ we calculate a friction coefficient of $\xi = 10.0 \pm 0.6\, fNs/\mu m^2$. This is five times higher than the pure hydrodynamic friction coefficient $\xi = 2\pi\eta/\ln(D/w) = 2.1\, fNs/\mu m^2$ of a solid tube with the DNA diameter $w = 2nm$ inside another PVP solution filled tube with diameter $D = (100nm \times 90nm)^{1/2} = 95nm$. The calculation is a lower bound as it neglects the average DNA segment tilt in the channel as well as frictional interactions

with the channel walls. Additionally, although electroosmotic backflow was minimized by the dynamic PVP coating, it may not have been completely eliminated. Future studies with different surface coatings may isolate the relative contributions of hydrodynamic friction, DNA-wall interactions, and electroosmotic backflow to the overall friction. The friction coefficient can be converted to drag per unit extended length ρ by scaling ξ with the previously determined extended length l_0. The result is $\rho = \xi L / l_0 = 26.7 \pm 3.0\, fNs/\mu m^2$.

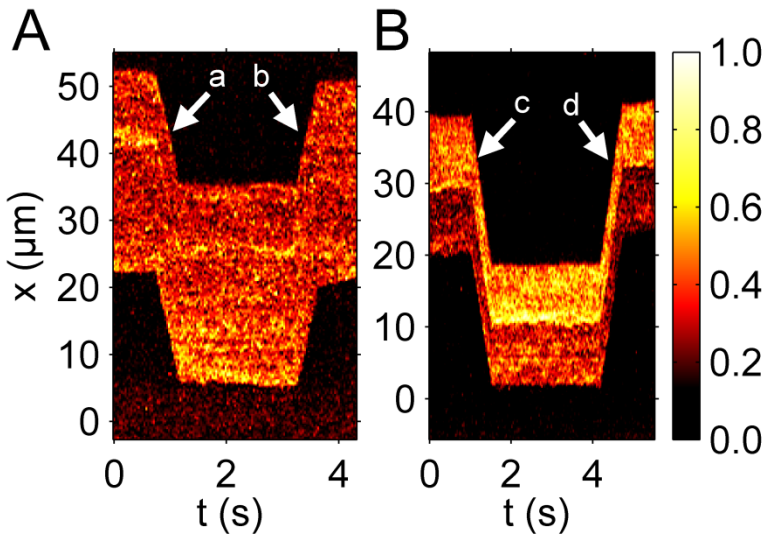

Figure 9. Intensity time traces for two T4 DNA molecules driven electrophoretically within a nanochannel. The molecules have already completely relaxed and do not change their extended length. **(A)** Straightened molecule. First the molecule is driven downward (a) and then upward (b) by 21 V/cm pulses. **(B)** Molecule with the upper end folded. This molecule is also driven downwards (c) and then upwards (d). The response was the same as in (A). No unfolding was observed.

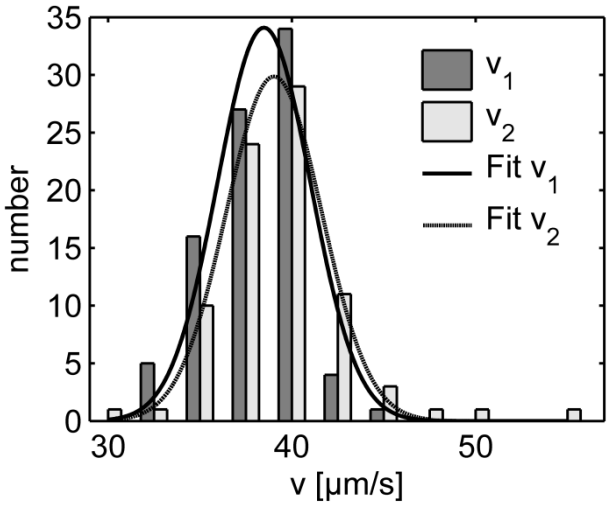

Figure 10. Histogram showing the distribution of velocities that were obtained for molecules driven through nanochannels under an electric field of 21V/cm in both directions. The distributions for the two directions are fit with Gaussians. The results are $v_1 = 38.5 \pm 2.5 \mu m/s$ and $v_2 = 39.0 \pm 2.6 \mu m/s$, which are equal to within the measurement error.

Calculation of Entropic Recoil Force. From the determined drag coefficient ρ and the fitted ratio of the entropic force to the drag coefficient f/ρ, we calculate an entropic force of $f = 217 \pm 40\, fN$. Note that this force is specific for DNA molecules at the interface between a nanochannel and the microchannel in our device. To obtain a theoretical estimate for comparison with the measured entropic recoil force, we calculated the free energy difference between a DNA strand in a 100nm channel and in free solution. This was done using Schaefer's polymer model for persistent polymers (31). Inside the nanochannel, this model was combined with de Gennes' "blob"-model (19) as has been described elsewhere in detail (15,16,32). Dividing the free energy change by half the extended length, which is approximately the distance

the center of mass moves during recoil, leads to an estimate for the entropic recoil force of $50\,fN$. The difference between the measured and estimated values for force might be due to the uncertainty of the shielding of the DNA backbone charge which influences the calculation of the drag. A better theoretical estimate might also be achieved by using more sophisticated numerical polymer model such as the worm like chain model, though such a calculation would require numerical simulations. Note also that our approach attributes the free energy change to the difference in configuration space accessible to a molecule, and assumes that electrical interaction between DNA and the walls is negligible. This is a valid assumption considering that the Debye screening length at the buffer concentration used is less than $1nm$.

Conclusion

We have demonstrated several ways of manipulating single DNA molecules in nanochannels. The entropic force was used to stretch molecules, to retract molecules from the nanochannels, and to straighten folded strands. In the case of molecule retraction, we were able to demonstrate the difference between those processes driven purely by the entropic recoil force and those processes for which elastic restoration also plays a role. Both kinds of molecule retraction could be interpreted quantitatively. By combining the results with friction measurements we were able to estimate the entropic force acting on DNA molecules at the entrance to our nanochannels.

This work is relevant for both the statistical physics and the applied biophysics fields. From a statistical mechanics perspective, further insight into the nature of the entropic force might be gained by investigating single molecule retraction from nanochannels of different widths. Stretching and relaxation experiments using molecules of

different sizes could lead to a better understanding of the elastic forces for DNA strands, as theory suggests that longer polymer molecules have smaller spring constants (33). As we have shown, elongation of molecules in nanochannels enables researchers to optically visualize molecule folding. Further studies in this area may lead to a better understanding of DNA packaging into bacteriophage heads or chromatin (34), which is an important topic in biology. Devices combining nanochannels with nanopore-like constrictions will give us the opportunity to combine optical and electrical DNA investigations. The entropically driven process of DNA recoil from nanopatterned geometries has already proven its potential to separate DNA by length (7). Our work will lead to an improved device geometry in order to achieve higher separation resolution for DNA molecules in the kilobase to megabase pair range.

Acknowledgment

This work was supported in parts by the National Human Genome Research Institute, as well as the Nanobiotechnology Center (NBTC), which is funded by the STC Program of the National Science Foundation under Agreement No. ECS-9876771 and the New York State Office of Science, Technology and Academic Research (NYSTAR). Device fabrication was performed in parts at the Cornell NanoScale Science and Technology Facility (CNF) with the assistance of Rob Ilic. CNF is a member of the National Nanotechnology Infrastructure Network, which is supported by the National Science Foundation, as well as in the Cornell Center for Materials Research (CCMR).

REFERENCES

1. Han, J. and H. G. Craighead. 2000. Separation of long DNA molecules in a microfabricated entropic trap array. Science 288:1026-1029.
2. Han, J. Y. and H. G. Craighead. 2002. Characterization and optimization of an entropic trap for DNA separation. Anal. Chem. 74:394-401.
3. Slater, G. W., Y. Gratton, M. Kenward, L. McCormick, and F. Tessier. 2003. Deformation, stretching, and relaxation of single-polymer chains: Fundamentals and examples. Soft Mater. 1:365-391.
4. Tessier, F., J. Labrie, and G. W. Slater. 2002. Electrophoretic separation of long polyelectrolytes in submolecular-size constrictions: A Monte Carlo study. Macromolecules 35:4791-4800.
5. Huang, L. R., J. O. Tegenfeldt, J. J. Kraeft, J. C. Sturm, R. H. Austin, and E. C. Cox. 2002. A DNA prism for high-speed continuous fractionation of large DNA molecules. Nat. Biotechnol. 20:1048-1051.
6. Kaji, N., Y. Tezuka, Y. Takamura, M. Ueda, T. Nishimoto, H. Nakanishi, Y. Horiike, and Y. Baba. 2004. Separation of long DNA molecules by quartz nanopillar chips under a direct current electric field. Anal. Chem, 76:15-22.
7. Cabodi, M., S. W. P. Turner, and H. G. Craighead. 2002. Entropic recoil separation of long DNA molecules. Anal. Chem. 74:5169-5174.
8. Turner, S. W. P., M. Cabodi, and H. G. Craighead. 2002. Confinement-induced entropic recoil of single DNA molecules in a nanofluidic structure. Phys. Rev. Lett. 88:128103.
9. Bakajin, O., T. A. J. Duke, J. Tegenfeldt, C. F. Chou, S. S. Chan, R. H. Austin, and E. C. Cox. 2001. Separation of 100-kilobase DNA molecules in 10 seconds. Anal. Chem. 73:6053-6056.

10. Chang, H., F. Kosari, G. Andreadakis, M. A. Alam, G. Vasmatzis, and R. Bashir. 2004. DNA-mediated fluctuations in ionic current through silicon oxide nanopore channels. Nano Lett. 4:1551-1556.

11. Heng, J. B., C. Ho, T. Kim, R. Timp, A. Aksimentiev, Y. V. Grinkova, S. Sligar, K. Schulten, and G. Timp. 2004. Sizing DNA using a nanometer-diameter pore. Biophys. J. 87:2905-2911.

12. Li, J. L., M. Gershow, D. Stein, E. Brandin, and J. A. Golovchenko. 2003. DNA molecules and configurations in a solid-state nanopore microscope. Nat. Mater. 2:611-615.

13. Storm, A. J., C. Storm, J. H. Chen, H. Zandbergen, J. F. Joanny, and C. Dekker. 2005. Fast DNA translocation through a solid-state nanopore. Nano Lett. 5:1193-1197.

14. Li, J., D. Stein, C. McMullan, D. Branton, M. J. Aziz, and J. A. Golovchenko. 2001. Ion-beam sculpting at nanometre length scales. Nature 412:166-169.

15. Reisner, W., K. J. Morton, R. Riehn, Y. M. Wang, Z. N. Yu, M. Rosen, J. C. Sturm, S. Y. Chou, E. Frey, and R. H. Austin. 2005. Statics and dynamics of single DNA molecules confined in nanochannels. Phys. Rev. Lett. 94:196101.

16. Tegenfeldt, J. O., C. Prinz, H. Cao, S. Chou, W. W. Reisner, R. Riehn, Y. M. Wang, E. C. Cox, J. C. Sturm, P. Silberzan, and R. H. Austin. 2004. The dynamics of genomic-length DNA molecules in 100-nm channels. Proc. Natl. Acad. Sci. USA 101:10979-10983.

17. Riehn, R., M. C. Lu, Y. M. Wang, S. F. Lim, E. C. Cox, and R. H. Austin. 2005. Restriction mapping in nanofluidic devices. Proc. Natl. Acad. Sci. USA 102:10012-10016.

18. Ueda, M., T. Hayama, Y. Takamura, Y. Horiike, T. Dotera, and Y. Baba. 2004. Electrophoresis of long deoxyribonucleic acid in curved channels: The effect of channel width on migration dynamics. J. Appl. Phys. 96:2937-2944.

19. de Gennes, P. G. 1979. Scaling Concepts in Polymer Physics. Ithaca, NY: Cornell Univ. Press.

20. Chen, P., J. J. Gu, E. Brandin, Y. R. Kim, Q. Wang, and D. Branton. 2004. Probing single DNA molecule transport using fabricated nanopores. Nano Lett. 4:2293-2298.

21. Bakajin, O. B., T. A. J. Duke, C. F. Chou, S. S. Chan, R. H. Austin, and E. C. Cox. 1998. Electrohydrodynamic stretching of DNA in confined environments. Phys. Rev. Lett. 80:2737-2740.

22. Perkins, T. T., D. E. Smith, R. G. Larson, and S. Chu. 1995. Stretching of a single tethered polymer in a uniform-flow. Science 268:83-87.

23. Sischka, A., K. Toensing, R. Eckel, S. D. Wilking, N. Sewald, R. Ros, and D. Anselmetti. 2005. Molecular mechanisms and kinetics between DNA and DNA binding ligands. Biophys. J. 88:404-411.

24. Stigter, D. 2002. Wall effects on DNA stretch and relaxation. Biophys. Chem. 101:447-459.

25. Schellman, J. A. and D. Stigter. 1977. Electrical double layer, zeta potential, and electrophoretic charge of double-stranded DNA. Biopolymers 16:1415-1434.

26. Gao, Q. F. and E. S. Yeung. 1998. A matrix for DNA separation: Genotyping and sequencing using poly(vinylpyrrolidone) solution in uncoated capillaries. Anal. Chem. 70:1382-1388.

27. Kang, S. H., M. R. Shortreed, and E. S. Yeung. 2001. Real-time dynamics of single-DNA molecules undergoing adsorption and desorption at liquid-solid interfaces. Anal. Chem. 73:1091-1099.

28. Smith, S. B., L. Finzi, and C. Bustamante. 1992. Direct mechanical measurements of the elasticity of single DNA-molecules by using magnetic beads. Science 258:1122-1126.

29. Campbell, L. C., M. J. Wilkinson, A. Manz, P. Camilleri, and C. J. Humphreys. 2004. Electrophoretic manipulation of single DNA molecules in nanofabricated capillaries. Lab Chip 4:225-229.

30. Brochard, F. and P. G. de Gennes. 1977. Dynamics of confined polymer-chains. J. Chem. Phys. 67:52-56.

31. Schaefer, D. W., J. F. Joanny, and P. Pincus. 1980. Dynamics of semiflexible polymers in solution. Macromolecules:1280-1289.

32. Reccius, C. H., J. T. Mannion, J. D. Cross, and H. G. Craighead. accepted. Compression and free expansion of single DNA molecules in nanochannels. Phys. Rev. Lett.

33. Bueche, F. 1962. Physical Properties of Polymers. New York, NY: Interscience.

34. Smith, D. E., S. J. Tans, S. B. Smith, S. Grimes, D. L. Anderson, and C. Bustamante. 2001. The bacteriophage phi 29 portal motor can package DNA against a large internal force. Nature 413:748-752.

CHAPTER 5

ENTROPIC UNFOLDING OF DNA MOLECULES IN NANOFLUIDIC CHANNELS*

*Previously Published Article: Nanoletters, 2008

Stephen L. Levy, John T. Mannion*, Ji Cheng, Christian H. Reccius, and Harold G. Craighead*[§]

School of Applied and Engineering Physics, Cornell University, Ithaca, NY 14853

[§] Corresponding author. E-mail: hgc1@cornell.edu.

* These Authors contributed equally to this work.

Single DNA molecules confined to nanoscale fluidic channels extend along the channel axis in order to minimize their conformational free energy. When such molecules are forced into a nanoscale fluidic channel under the application of an external electric field, monomers near the middle of the DNA molecule may enter first, resulting in a folded configuration with less entropy than an unfolded molecule. The increased free energy of a folded molecule results in two effects: an increase in extension factor per unit length for each segment of the molecule, and a spatially localized force that causes the molecule to spontaneously unfold. The ratio of this unfolding force to hydrodynamic friction per DNA contour length is measured in nanochannels with two different diameters.

Introduction. Nanofluidic channels have shown promise for the analysis of genomic length DNA molecules. Assays for fragment length analysis[1-3], real time enzymatic restriction mapping[4], and localization of hybridized probes[5,6] have all been demonstrated. The growing interest in long single molecule DNA sequencing techniques provides good motivation for understanding the means to control and manipulate single molecules in fluidic systems[7,8]. Detailed studies of the conformation and dynamics of single molecules in nanochannels have corroborated models for self excluding polymers in confined environments. In previous experiments, thermally induced fluctuations of extension length[9], expansion after a high degree of compression[10], and contraction after a high degree of stretching[11] have all been observed in qualitative agreement with the theory. Self extraction of molecules partially inserted into nanostructures has also been observed, allowing for direct measurement of a confinement induced force[11-13]. Such studies of entropic forces resulting from confined geometries have biological importance for understanding the packaging of DNA into viral capsids[14] and bacterial chromosome segration[15], for example.

Recently, molecular dynamic (MD) simulations have been applied to study confined polymers that overlap[16]. While it is experimentally difficult to position two DNA molecules in a nanochannel so that they partially overlap, it is relatively straightforward to insert a single molecule into a nanochannel such that the front end is folded over on itself.

We have inserted and observed folded DNA molecules in nanochannels as depicted in Figure 1. Long DNA molecules are electrophoretically driven from a microfluidic region to the entrance of the smaller channel. The electric field is turned off before the

molecules enter the channel and thermal agitation causes them to undergo a number of different intramolecular conformations. When a molecule happens to be in an appropriate conformation and position relative to the channel entrance (as depicted in Figure 1a), the field is turned on and the molecule enters the channel, often with a folded front end. After the entire DNA molecule has entered the channel, the field is switched off and the dynamics of the molecule are observed. In this letter we pay particular attention to the spontaneous unfolding of the looped end which we theorize to be entropically induced. Presently, the theory of a long polymer confined in a nanochannel is reviewed, the forces on a partially folded molecule in a nanochannel are discussed, and a model describing the unfolding process through time is derived.

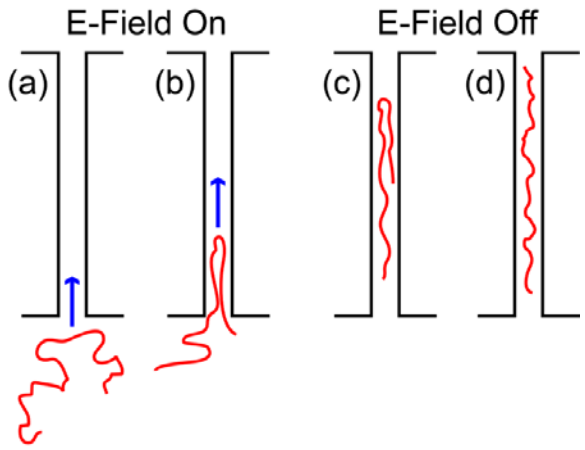

Figure 1. Overview of experimental procedure. (a) A long DNA molecule sits in a microchannel, adjacent to the entrance of a nanochannel. (b) The electric field (blue arrow) pulls the DNA into the nanochannel. Because the molecule's entrance was initiated at some point along the backbone distinct from either of the ends, it enters the channel in a folded conformation. (c) Once the electric field is turned off, the DNA strand relaxes inside the nanochannel in a high energy folded state. It gradually unfolds, thereby reducing its conformational free energy. (d) The molecule has completely unfolded within the channel, extending to its equilibrium conformation.

Theory. We consider a self-avoiding polymer with contour length C, and persistence length p. In free solution the polymer assumes a spherical conformation with a radius of gyration $R_G \propto C^{3/5}$. If confined to a long cylindrical channel of diameter D with $D << R_g$, the polymer will extend along the axis of the channel to an equilibrium length L_E. According to a theory developed by de Gennes and co-workers[17,18], the confined polymer can be thought of as a series of impenetrable and hydrodynamically uncorrelated blobs where excluded volume effects are maintained within a blob. The blob model predicts that the extension factor for a confined polymer scales according to

$$\frac{L_E}{C} \approx \frac{(pw)^{1/3}}{D^{2/3}} \qquad (1)$$

where w is the width of the molecule. At this equilibrium length the conformational free energy is at a minimum. The scaling of extension length with channel diameter has been measured for long DNA molecules in nanofabricated channels[9]. Additionally, the scaling of extension length with w has been investigated in channels[19] and nanoslits[20]. By varying the ionic strength of the buffer solution, and thus the ionic screening length and effective width of the charged DNA monomers, these experiments found that lower ionic strength caused a significant increase in extension. While the cause of this extension increase is under debate[21], these studies attribute it to volume exclusion effects[19,20].

The experiment described in this letter allows us to probe excluded volume interactions in another manner. It is conceivable that two overlapping DNA molecules in a nanochannel could each have a larger extension than they would in the absence of the other. Since extended length depends on excluded volume interactions, this extra

extension could result from the apparently smaller channel diameter each molecule sees due to the presence of the other. Our experiment with folded DNA molecules allows us to investigate this concept. We define α as the extension factor of an unfolded segment of DNA in a nanochannel, and β as the extension factor for a segment of DNA which is occupying the same space in the channel as another, independent segment of DNA. The first question we attempt to answer is whether β is greater than α.

In addition to determining the extension factors for a partially folded molecule, we investigate dynamics of our partially folded DNA molecules. We observe an entropically induced force, driven by an inhomogeneity in conformational free energy along the length of the molecule, which causes a spontaneous unfolding of initially folded molecules. Through diffusive motion, the segment of a molecule straddling the interface between the folded and unfolded regions can test the volume of space available on both sides of the interface. Because there are a greater number of accessible states for that segment in the unfolded region, it experiences a force that drives it from the folded to the unfolded region.

A simplified force diagram of a partially folded DNA molecule confined to a nanochannel is shown in Figure 2. In this diagram, the extension length of the unfolded portion of DNA is defined as $L_U = \alpha \cdot C_U$, where C_U is the contour length of the unfolded portion of the DNA. In the folded section, the contour length of the DNA is defined as C_F. The extension of the folded portion (the distance between x_2 and x_3 in the diagram) is given by $L_F = \beta \cdot C_F / 2$. The magnitude of the unfolding force is written as f_U. In order to satisfy force balance, the unfolding force acts with

equal magnitude, but opposite direction, on both the red and black points along the DNA strand.

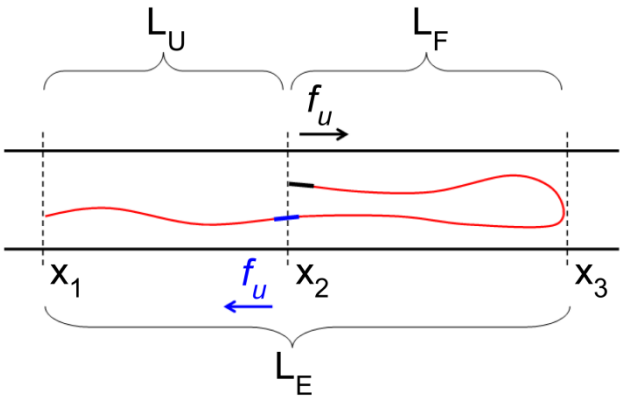

Figure 2. In this cartoon of folded DNA in a nanochannel, the local bending of the molecule is greatly minimized. The folded state is characterized by the projected length of the unfolded (L_U) and folded (L_F) portions of the molecule along the channel axis. The unfolding force, localized at the position x_2, results from the difference in free energy between conformations in which the blue segment does or does not overlap with the upper black segment. The resulting forces, $-f_U$ and f_U, acting on the upper and lower segments of the molecule, respectively are balanced by hydrodynamic frictional forces that are assumed to be proportional to the length and velocity of each segment. In our model, a contour length δC will be extended along the channel axis by an amount $\delta L = \alpha \cdot \delta C$ or $\delta L = \beta \cdot \delta C$, depending on whether the segment is part of the unfolded or folded portion of the molecule

In our model, at any instant in time, the upper and lower segments of the molecule are considered to be two unconnected molecules. Each is accelerated by f_U until it reaches a velocity at which hydrodynamic friction is large enough to resist further acceleration (assumed to happen instantaneously). Ignoring hydrodynamic

interactions (HI) between monomers, the instantaneous hydrodynamic drag on the upper portion of the molecule is given by

$$f_{hydro}^{upper} = -\frac{dx_2}{dt} \cdot \xi \cdot \frac{C_F}{2} \qquad (2)$$

where ξ is the hydrodynamic friction per unit contour length. This is probably a slight overestimate of the drag since HI should only be completely screened[23] for channels with $D < p$ while the diameter of our channels is a factor of two or three larger. For the lower segment of molecule, the portions in the unfolded and folded regions are modeled as moving together. Because we allow for a different extension factor for those two regions, however, monomers in the unfolded portion move at a velocity $\dot{x}_1$ (where a dot denotes the time derivative) while those in the folded portion move at a velocity $\dot{x}_1 \cdot \beta/\alpha$. The total frictional force acting on the lower segment is the sum of the frictions acting on the two pieces (one in the unfolded region, and one in the folded region.

$$f_{hydro}^{lower} = -\frac{dx_1}{dt} \cdot \xi \cdot \left(C_U + \frac{\beta}{\alpha} \frac{C_F}{2} \right) \qquad (3)$$

After setting the frictional terms f_{hydro}^{upper} and f_{hydro}^{lower} equal to f_U, the following difference equations are obtained:

$$dx_1 = \frac{f_U \cdot \alpha}{\xi \cdot (L_U + L_F)} dt \qquad (4)$$

$$dx_2 = \frac{-f_u \cdot \alpha \cdot \gamma}{\xi \cdot L_F} dt \qquad (5)$$

where γ is defined as the ratio of extension factors β/α. From these equations, a numerical solution can be obtained which gives the positions x_1 and x_2 as a function of time. By fitting this model to unfolding data, an estimate for the magnitude of f_U/ξ is obtained. We could have introduced additional terms in our model to account for HI between the upper and lower segments, but the shape of the unfolding data in time is well described by one free parameter (see Supplemental Information).

Experimental Section. The nanochannel devices used in this letter were fabricated on mirror-polished fused silica wafers using a combination of electron beam lithography on a JBX-9300FS system (JEOL, Peabody, MA) with a negative tone resist (ma-N 2403, Micro Resist Technology, Berlin, Germany) and optical lithography. Microchannel regions were reactive ion etched adjacent to the nanochannels for ease with DNA loading. Additional details describing the device fabrication can be found in the Supporting Information. A schematic of the completed device as well as several electron micrographs of the nanostructures before bonding can be seen in Figure 3. We fabricated two sets of nanochannels with dimensions approximately 215×155 nm (width $\times$ depth) and 150×135 nm. The depth of the nanochannels was determined using a Tencor P-10 Surface Profiler with a specified sub-nm resolution. Due to the size of the profiling tip, we measure the depth in the etched regions adjacent to the nanochannel entrance (Figure 3c) and assume that the channels are etched to the same depth. The width of the channels was determined from scanning electron microscope images (Figure 3d) to an accuracy of approximately 10%. We compute the geometric average of the nanochannel dimensions as the square root of the width times the height[22], yielding average nanochannel diameters of 183 nm and 142 nm, respectively.

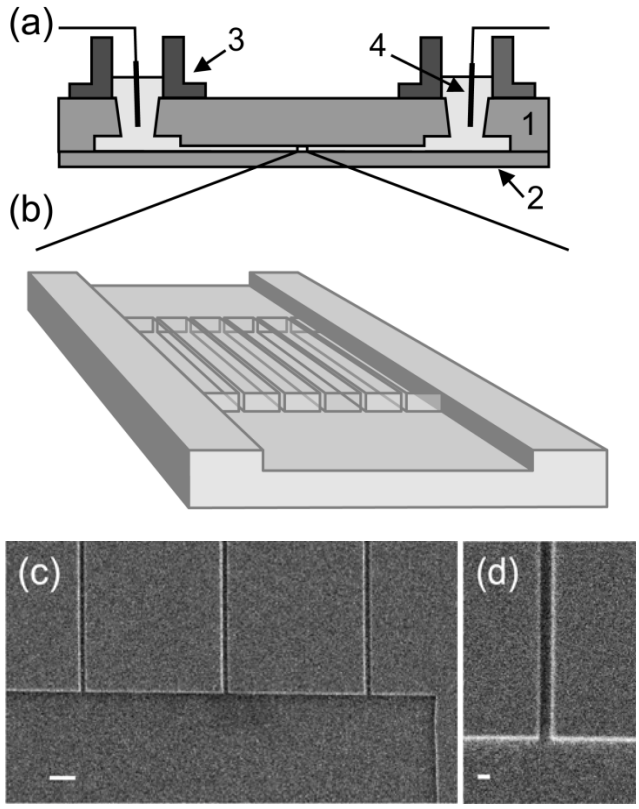

Figure 3. (a) Side view schematic representation of a fused silica substrate wafer (1) containing nanochannel arrays, which is bonded to a coverslip wafer (2). DNA molecules were loaded into fluidic reservoirs (3) and driven electrophoretically using gold electrodes (4). (b) Schematic close-up view of the nanochannel array region. Top-down scanning electron microscope image of a microchannel connected to nanochannel array (c) and magnified image of a single nanochannel (d) with dimension 150×135 nm (width $\times$ height). The scale bars are 920 nm and 195 nm in images (c) and (d), respectively.

T4-bacteriophage DNA molecules (T4GT7 DNA, *Nippon* Gene, Toyama, Japan) were stained with the bis-intercalating dye YOYO-1 (Molecular Probes, Eugene, OR). The contour length (C_{T4}) of a dyed T4-DNA molecule (165.6 kbp) has been shown to

increase by $\approx 30\,\%$[23,24] at a saturated dye to base pair ratio of 1:4. At our dye ratio of 1:5, we then expect $C_{T4} \approx 70\ \mu\text{m}$. The buffer consisted of 445 mM Tris-borate and 10 mM EDTA ($5\times$TBE, pH 8.3, Sigma, St. Louis, MO) containing 4% (v/v) β –mercaptoethanol (Sigma) to limit photobleaching. Electrical contact was made by inserting gold electrodes in the reservoirs. Individual molecules were observed with an IX71 inverted microscope (Olympus, Melville, NY), which was equipped with a 100x/1.35 NA oil immersion objective (Olympus). Images were acquired using a Cascade 512b EMCCD (Photometrics, Tucson, AZ) at 10 frames per second using custom software written in Labview (National Instruments, Austin, TX).

DNA molecules were electrophoretically driven from loading regions to near the nanochannel entrance with a potential of 40 V. A small potential (~2 V) was applied to drive T4 molecules into nanochannels, resulting in a calculated electric field $E \approx 120\ \text{V/cm}$ in nanochannels and $E \approx 10\ \text{V/cm}$ in the microchannel region. A small offset voltage (< 10 mV) was sometimes used to prevent drift of DNA molecules inside the nanochannels due to either a residual voltage or pressure differential, or chemical potential differences across the device. Several videos were recorded for each molecule. For each video, the DNA molecule was observed to enter the channel in either an unfolded or folded configuration. If folded, the molecule was recorded until after it appeared to have finished unfolding. If unfolded, the molecule was typically driven back into the microchannel and the previous steps were repeated.

DNA molecule position and folded length were extracted from each video frame using custom algorithms programmed in MATLAB (The Mathworks, Natick, MA). In each frame, the average background intensity was subtracted from the signal region and the intensity was projected over 4 pixels (= 640 nm) along the dimension perpendicular

to the channel axis. The endpoints of the DNA molecule were determined by requiring the projected intensity to be larger than a fixed value that was typically about three times larger than the background (Figure 4c). The folded region of the molecule was then found by requiring the intensity to be larger than a second threshold value using an algorithm that allowed for both turn-on and small fluctuations below this threshold (Figure 4b). The folded intensity threshold was set at approximately 1.5 times the intensity of the unfolded molecule as determined visually for each molecule. For analyzing the dynamics of unfolding molecules, we used frames acquired at least 15 s after the molecule had entered the channel (to allow the molecule to relax[11]) up until a few seconds before the molecule had completely unfolded.

Using the determination of the end points of the molecule, we construct a time trace of the intensity profile of the molecule (Figure 4a), which shows the normalized intensity along the channel axis plotted against time. Since the algorithm for determining the endpoints and folded region of the molecule considers each frame independently, there are occasional unphysical discontinuities in these measurements as a function of time due to intensity fluctuations. To correct for these, we fit both the end-to-end and folded lengths to a smoothing function and discard outliers. In the channel with average diameter of 183 nm, we analyzed the unfolding of 15 separate molecules over an average time of 54 s where the mean initial folded length was $6\ \mu\text{m}$. In the 142 nm channel, we analyzed the unfolding of 23 separate molecules over an average time of 75 s where the mean initial folded length was $10\ \mu\text{m}$.

Figure 4. (a) Time trace showing normalized fluorescent intensity projected transverse to the nanochannel axis as a function of time. (b) Projected intensity of the DNA molecule shown in (a) as a function of position along the nanochannel while folded at 15 s. Both the end-to-end (dotted line) and folded length (dashed line) were determined using the algorithms described in the text. The intensity in the folded region is approximately twice as large as in the unfolded region. (c) Intensity projection of the same molecule at 55 s. At this point the molecule is completely unfolded resulting in a roughly constant projected intensity.

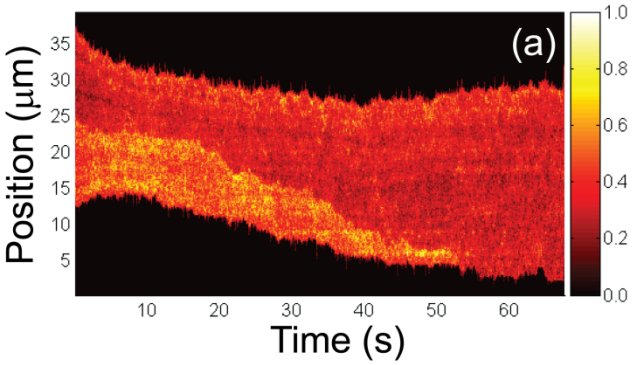
(a)
Position (μm)
35
30
25
20
15
10
5
10
20
30
40
50
60
Time (s)
1.0
0.8
0.6
0.4
0.2
0.0

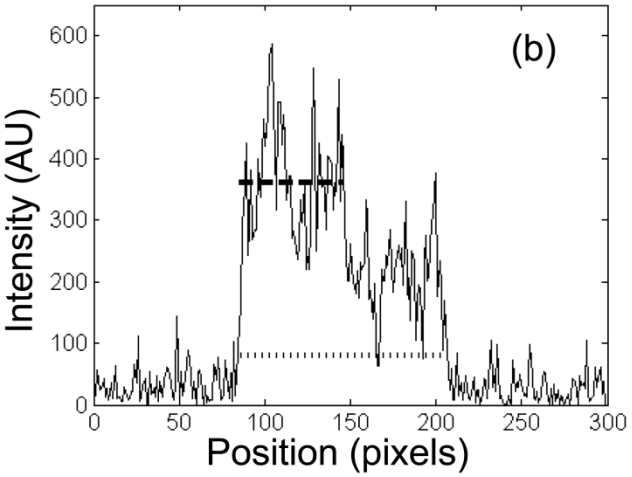
(b)
Intensity (AU)
600
500
400
300
200
100
0
0
50
100
150
200
250
300
Position (pixels)

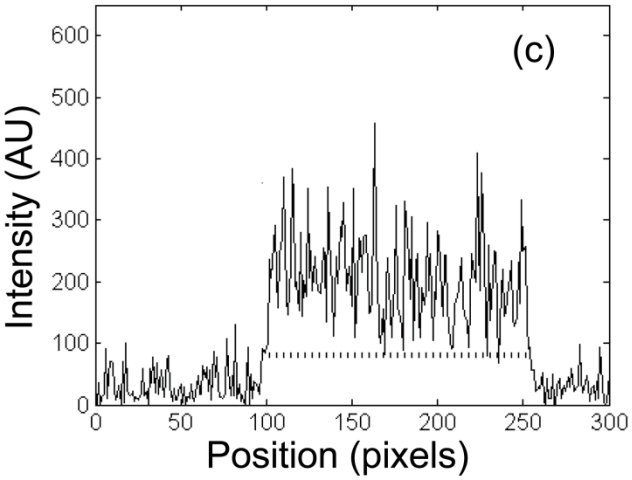
(c)
Intensity (AU)
600
500
400
300
200
100
0
0
50
100
150
200
250
300
Position (pixels)

Results and Discussion. In order to determine the difference in extension for the folded and unfolded portions of the molecule, we derive the following equation for the folded extension length normalized by the equilibrium extension length:

$$L_F / L_E = \frac{\beta}{2\alpha}(1 - L_U / L_E) \qquad (6)$$

In deriving Eq. (6), we have assumed conservation of contour length and that the extension factor of the unfolded portion of the molecule (α) is the same as the extension factor at equilibrium in the nanochannel (see Supplemental Information). We plot L_F / L_E *versus* L_U / L_E for each molecule (Figure 5) and fit the data with a linear polynomial to extract the ratio of extension factors $\gamma = \beta / \alpha$. We determine L_E using the same thresholding algorithm described in the previous section from all frames at least 5 s after the molecule has unfolded (though the value we extract for γ does not depend on L_E). We measured the extension factor ratio $\gamma = 1.36 \pm 0.14$ and 1.30 ± 0.14 in the 183 and 142 nm nanochannels, respectively, where the error is the standard deviation (SD) of the measurements. Given our model, this implies that folded regions of molecules are ≈ 30 % more extended than unfolded regions. We do not find a significant difference in the ratio of extension factors based on nanochannel dimension.

In addition to measuring the ratio of folded to unfolded extension factors, we verified that the intercept along the L_U / L_E axis is consistent with one to within $\approx 5\%$ for molecules in both diameter channels. This implies that the extension factor of the unfolded portion of the molecule is the same as the equilibrium unfolded extension factor. If, for example, the unfolded portion of the molecule was compressed during the unfolding process, we would not expect the intercept to be consistent with one.

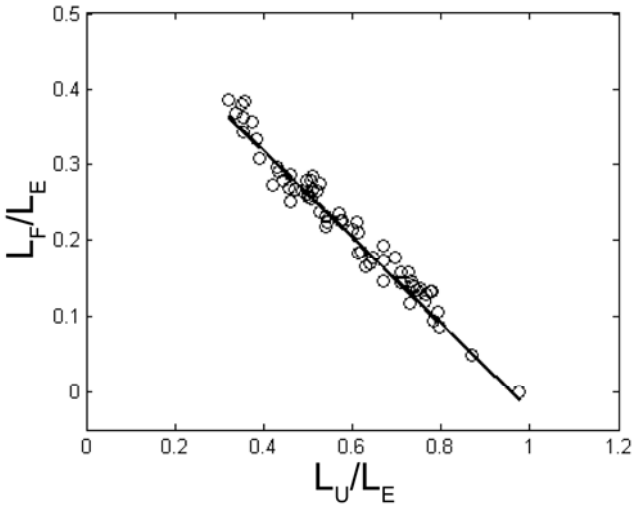

Figure 5. Plot of $L_F(t)$ (folded length) *versus* $L_U(t)$ (unfolded length), both of which have been normalized to L_E (end-to-end length). The result of a linear fit is overlaid (solid line). The extension parameter calculated from the slope is $\gamma = 1.14$, implying larger extension along the folded portion of the molecule relative to the unfolded. The lengths have been averaged over 0.6 s intervals to aid in visualization.

The average extension factors we measure at equilibrium for the 183 and 142 nm channels are 0.20 and 0.35, respectively, which agree quite well with data shown in Figure 4a of Ref. 9. Further, we can rederive Eq. (6) assuming instead that the extension factor for the folded portion of the molecule is the same as for a completely unfolded molecule at equilibrium. However, we then observe an intercept along the L_U / L_E axis that is greater than one by ≈ 30 % for both nanochannel dimensions. To summarize, these results indicate that the unfolded portion of the molecule is extended similarly to the molecule at equilibrium in the channel, and that the folded portion of the molecule is extended by an additional 30% relative to the equilibrium length. We hypothesize that this effect is due to a larger excluded volume interaction for the

folded portion of the molecule since the monomer density has increased relative to an unfolded molecule. However, we cannot prove this hypothesis since we do not yet have a quantitative theory relating this extra extension to excluded volume interactions.

In addition to measuring extension factors, we use the numerical solution to Eq. (4) and (5) to measure the ratio of unfolding force to hydrodynamic friction per contour length f_U/ξ. For a given molecule we initialize the model with L_F and L_U, determined from the first 2.5 s of unfolding, as well as with γ and α found for that molecule as described previously, and with a trial value for f_U/ξ. The model then computes the unfolded and folded lengths as a function of time as well as the position x_3 (Figure 2). We iterate over the input value of f_U/ξ until we find a minimum in the residual, defined as the sum of the squared difference between the measured and model values for the folded length at each time, normalized by the number of data points. We continue to iterate about the minimum until the change in the residual is less than 1%. A typical result comparing the numerical model prediction to the measured unfolding is shown in Figure 6. Note that the iterative procedure finds the minimum residual for L_F, though the model also computes L_E using the input value of gamma. We find good visual agreement between the model's prediction and the data for both L_F and L_E as a function of time. The shape of a typical curve that describes the folded length as a function of time is similar to a power-law with an exponent of $1/2$. The actual bend in the contour is not considered to affect the motion until the last instant of the unfolding process, when the end flops open, and the bending energy is released. We measure average values of $f_U/\xi = (1.8 \pm 1.0)\ \mu\text{m}^2/\text{s}$ and $(2.4 \pm 1.5)\ \mu\text{m}^2/\text{s}$ in the 183 and 142 nm channels, respectively.

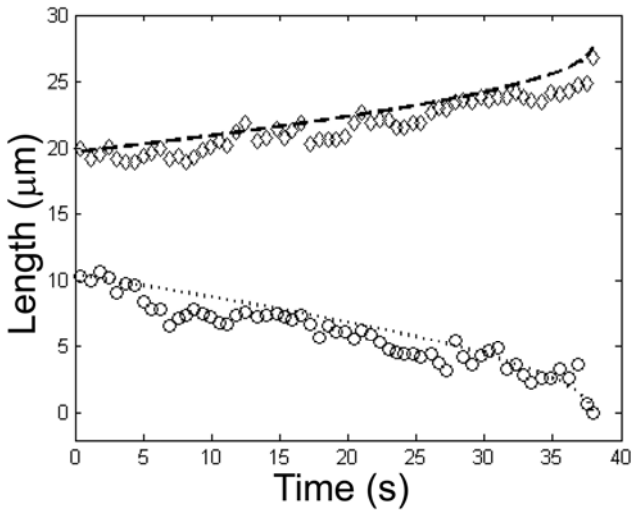

Figure 6. Plot of measured L_E (end-to-end length, diamonds) and L_F (folded length, circles) for a DNA molecule in a 142 nm channel as a function of time. The results from the numerical simulation for L_E and L_F as a function of time are overlaid as dashed and dotted lines, respectively. The best fit from the numerical simulation yields $f_U / \xi = 4.4\ \mu\text{m}^2/\text{s}$. The value for γ was fixed to 1.14 as determined from the fit shown in Figure 5. The lengths have been averaged over 0.6 s intervals to aid in visualization.

We attempt to qualitatively understand the ratio of these values given our nanochannel dimensions. Since the unfolding force is expected to scale inversely with the channel diameter[16], and the friction coefficient is known to scale inversely with the logarithm of the channel diameter[23,25], we expect f_U / ξ to scale as $\approx \ln(D)/D$. We then expect f_U / ξ to be roughly 20% larger in the 142 nm channel than in the 183 nm channel. We find a larger value of f_U / ξ in the smaller diameter channel, though with rather large uncertainty.

In order to obtain an estimate for the unfolding force, we first extrapolate the value of ξ from Mannion *et al.*[11] who measured a friction per unit contour length of $\xi = (10.0 \pm 0.6)\,\mathrm{fN \cdot s/\mu m^2}$ in 95 nm diameter nanochannels. Taking into account the $(\ln D)^{-1}$ scaling for the frictional dependence on channel dimension, we estimate an average unfolding force of $\approx 16\,\mathrm{fN}$ and $\approx 22\,\mathrm{fN}$ in the 183 and 142 nm channels, respectively. Arnold and Jun[16] have recently used MD simulations to investigate the repulsive force between two overlapping polymers confined to a cylindrical tube. They estimate that the repulsive force is given by $k_B T/D$, which is $\approx 25\,\mathrm{fN}$ in our nanochannels at room temperature and agrees well with our measured value.

Additionally, we compare the magnitude of the unfolding force to an entropic recoil force previously measured[11]. Briefly, this recoil force results when a DNA molecule is partially inserted into a nanochannel, with the rest of the molecule in a microchannel. Due to the difference in the number of molecular configurations available to the molecule in the two regions, an entropically induced force acting at the interface pulls the molecule into the microchannel. This force is similar to the unfolding force described in this letter. However, the change in accessible space is clearly greater for the recoiling molecule than for the unfolding one, which should result in a larger force for the recoiling molecule. The measured recoil force was approximately an order of magnitude larger than the unfolding force we present here, supporting this idea.

As previously stated, Arnold and Jun[16] investigated a similar entropic force between confined overlapping polymers using MD simulations. Their main result is that

entropic segregation occurs on a shorter time scale than diffusion However, they report two additional findings that we did not observe. They found that the monomer density in the region in which the polymers overlap did not depend on the presence of the additional polymer. In contrast, we measured an extension factor (reduced monomer density) of approximately 30% in the folded region of the molecule. Also, they observed that the repulsive force caused the polymers to compress as they segregated as seen in Figure 6c of Ref. 16. We did not observe compressions distinguishable from random fluctuations in the projected photon intensities. It is possible that compressions near the folding interface could result in an overestimation of the folded length. However, one would then expect a smooth rather than step-like transition in the intensity, contrary to what was typically observed (see Figure 4b). Our experiment differs mainly from their simulation in that we studied a single molecule unfolding, while Arnold and Jun examined two separate chains repelling. Consequently, the segregation force acts at both ends of the overlapping region in their simulation. Both our numerical model and their dynamic simulation ignored HI between monomers. These disagreements concerning polymer extension or compression may be attributed to a different ratio of the repulsive force to the hydrodynamic friction, or a different value of the polymer spring constant in their model.

Conclusion. It has been shown that DNA molecules can be driven into a nanochannel such that the front end of the molecule is folded over on itself. Using fluorescence microscopy, molecules in a folded conformation can be identified in real time and subsequently analyzed in detail. In this letter, we described two new measurements of folded molecules in nanochannels that have implications for the study of self avoiding

polymers in a confining environment. First, we found a larger extension factor for segments of a DNA molecule that overlap compared to those that do not, which is most likely due to increased excluded volume interactions. Second, we measured the magnitude of an entropic repulsive force between overlapping polymer segments that originates from a difference in the number of available molecular configurations. These results add to the growing body of knowledge regarding the behavior of DNA in nanofluidic channels, and may lead to a greater ability to manipulate and analyze single DNA molecules in lab on chip devices. The observation of the unfolding process suggests that a free energy difference between overlapping and nonoverlapping polymer segments results in an entropically induced force that can segregate two initially overlapping polymers, as originally proposed by Arnold and Jun.

In future studies, we hope to investigate the unfolding process in greater detail, particularly during the initial relaxation of the polymer. While our data suggests that the unfolding force may be a function of channel diameter, we would like to systematically study unfolding using channels of many different sizes, with diameters ranging from sub-50 nm to several hundred nm. Other parameters which could be varied are ion concentration and valence. It is expected that both the dynamic behavior of the DNA and the effective confinement of the nanochannel will change as charges are screened over greater lengths or by ions of higher valence. We hope further simulations can verify the increased extension of folded molecules and quantify its dependence on exclusion volume interactions.

Acknowledgement. This work was supported by the National Human Genome Research Institute, as well as the Nanobiotechnology Center (NBTC), which is funded

by the STC Program of the National Science Foundation (NSF) under agreement No. ECS-9876771 and the New York State Office of Science, Technology and Academic Research (NYSTAR). Device fabrication was performed in part at the Cornell NanoScale Science and Technology Facility (CNF) with the assistance of Daron Westly. The CNF is a member of the National Nanotechnology Infrastructure Network and the Cornell Center for Materials Research (CCMR), both of which are supported by the NSF.

Supporting Information Available. Detailed fabrication methods, experimental methods, difference equations for numerical solution of unfolding model, and video of unfolding DNA molecule (S-1).

SUPPORTING INFORMATION

ENTROPIC UNFOLDING OF DNA MOLECULES IN NANOFLUIDIC CHANNELS

*Stephen L. Levy *, John T. Mannion *, Ji Cheng, Christian H. Reccius, and Harold G. Craighead*[§]

School of Applied and Engineering Physics, Cornell University, Ithaca, NY 14853

[§] Corresponding author. E-mail: hgc1@cornell.edu.

* These Authors contributed equally to this work.

Device Fabrication. Devices were patterned on a mirror-polished fused silica wafer with a thickness of 500 μm (MarkOptics, Santa Ana, CA) using a combination of electron beam and optical lithography. Initially, the negative electron beam resist ma-N 2403 (micro resist technology, Berlin, Germany) was spun onto the substrate with a nominal thickness of 300 nm. A thin layer of the conducting polymer e-spacer was subsequently spun on to help draw current during the electron-beam process. Negative patterns of the nanochannel array regions were exposed using a JBX-9300FS electron beam lithography system (JEOL, Peabody, MA). The entire wafer was then exposed with UV illumination (254 nm) for 90 s on an ABM High Resolution Mask Aligner using a mask to protect the regions previously exposed by electron beam. Following 90 sec development in 300 MIF, nanochannels were etched using a Plasmalab 80Plus REI (Oxford Instruments, Eynsham, UK) with CF_4 at 150 Watts for 4-6 min depending on the desired channel depth. The previous exposure with the ABM prevented the entire wafer surface from being etched in this step. Microchannels connecting to the nanochannel array were subsequently patterned using

optical contact lithography and etched with the Plasmalab using a CHF_3/O_2 gas mixture at 200 Watts for approximately 30 min. Access holes were created by alumina powder blasting from the backside of the wafer. Finally a 170 μm fused silica cover wafer (MarkOptics) was touch bonded and annealed at 1050°C to the device wafer, enclosing the channels. Pipette tip ends were glued to the wafer surface around the access holes using RTV 732 Sealant (Dow Corning, Midland, MI) forming buffer reservoirs.

DNA and Buffer Preparation. T4-bacteriophage DNA molecules (T4GT7 DNA, *Wako, Nippon* Gene) were stained with the bis-intercalating dye YOYO-1 (Molecular Probes, Eugene, OR) and used at a concentration of a few $\mu g/ml$. The buffer consisted of 445 mM Tris-borate and 10 mM EDTA ($5\times$ TBE, pH 8.3, Sigma, St. Louis, MO) containing 4% (v/v) β –mercaptoethanol (Sigma) to limit photobleaching. Electrical contact was made by inserting gold electrodes in the reservoirs.

Microscopy. The individual molecules were observed with an IX71 inverted microscope (Olympus, Melville, NY), which was equipped with a 100x/1.35 NA oil immersion objective (Olympus) and illuminated by a 100W mercury arc lamp or X-Cite 120 PC (Exfo). An XF100 filter set (Omega Optical, Brattleboro, VT) was used for fluorescence imaging. Images were acquired using a Cascade 512b EMCCD (Photometrics) at 10 frames per second using custom software written in Labview (National Instruments).

Difference Equations for Numerical Solution of Unfolding Model. Declaration of length variables and extension factors:

$$L_E = \alpha \cdot C = x_1 - x_3 \qquad \text{(S.1)}$$

$$L_U = \alpha \cdot C_U = x_1 - x_2 \tag{S.2}$$

$$L_F = \beta \cdot C_F / 2 = x_2 - x_3 \tag{S.3}$$

$$C = C_U + C_F \tag{S.4}$$

$$C = L_E / \alpha = L_U / \alpha + 2L_F / \beta \tag{S.5}$$

$$L_E = L_U + \frac{2\alpha}{\beta} L_F \tag{S.6}$$

Viscous Drag:

ρ, the drag per unit extended length of an unfolded portion of molecule

ξ, the drag per unit contour length

$$\rho = \xi \cdot C / L_E = \xi / \alpha \tag{S.7}$$

Force balance equation for long, lower portion of molecule:

$$f_U - \frac{dx_1}{dt} \xi \left(C_U + \frac{\beta}{\alpha} \frac{C_F}{2} \right) = 0 \tag{S.8}$$

$$f_U - \frac{dx_1}{dt} \frac{\xi}{\alpha} (L_U + L_F) = 0 \tag{S.9}$$

$$f_U - \frac{dx_1}{dt} \frac{\xi}{\alpha} \left[(x_1 - x_2) + (x_2 - x_3) \right] = 0 \tag{S.10}$$

$$\frac{\delta x_1}{\delta t} = \frac{f_U \cdot \alpha}{\xi \cdot (x_1 - x_3)} \tag{S.11}$$

Force balance equation for short, upper portion of molecule:

$$f_U + \frac{dx_2}{dt} \xi \cdot \frac{C_F}{2} = 0 \tag{S.12}$$

$$f_U + \frac{dx_2}{dt} \xi \cdot \frac{L_F}{\beta} = 0 \tag{S.13}$$

$$f_U + \frac{dx_2}{dt} \xi \cdot \frac{(x_2 - x_3)}{\beta} = 0 \tag{S.14}$$

$$\frac{\delta x_2}{\delta t} = \frac{f_U \cdot \beta}{\xi \cdot (x_3 - x_2)} \qquad \text{(S.15)}$$

Supplementary Move S1. Real time movie of DNA molecule unfolding in 142 nm diameter nanochannel (images were acquired at 10 frames per second). The contrast has been altered to improve viewing.

REFERENCES

1. Foquet, M., Korlach, J., Zipfel, W., Webb, W. W., and Craighead, H. G., *Anal. Chem.* **74**, 1415 (2002).
2. Reccius, C. H., Stavis, S. M., Mannion, J. T., Walker, L. P., and Craighead, H. G., *Biophys. J.* **95**, 273 (2008).
3. Tegenfeldt, J. O., Prinz, C., Cao, H., Chou, S., Reisner, W. W., Riehn, R., Wang, Y. M., Cox, E. C., Sturm, J. C., Silberzan, P., and Austin, R. H., *Proc. Natl. Acad. Sci.* **101**, 10979 (2004).
4. Riehn, R., Lu, M. C., Wang, Y. M., Lim, S. F., Cox, E. C., and Austin, R. H., *Proc. Natl. Acad. Sci.* **102**, 10012 (2005).
5. Chan, E. Y., Goncalves, N. M., Haeusler, R. A., Hatch, A. J., Larson, J. W., Maletta, A. M., Yantz, G. R., Carstea, E. D., Fuchs, M., Wong, G. G., Gullans, S. R., and Gilmanshin, R., *Genome Research* **14**, 1137 (2004).
6. Phillips, K. M., Larson, J. W., Yantz, G. R., D'Antoni, C. M., Gallo, M. V., Gillis, K. A., Goncalves, N. M., Neely, L. A., Gullans, S. R., and Gilmanshin, R., *Nucleic Acids Research* **33**, 5829 (2005).
7. Chan, E. Y., *Mutation Research* **573**, 13 (2005).
8. Zwolak, M. and Di Ventra, M., *Rev. Modern Phys.* **80**, 141 (2008).
9. Reisner, W., Morton, K. J., Riehn, R., Wang, Y. M., Yu, Z. N., Rosen, M., Sturm, J. C., Chou, S. Y., Frey, E., and Austin, R. H., *Phys. Rev. Lett.* **94** (2005).
10. Reccius, C. H., Mannion, J. T., Cross, J. D., and Craighead, H. G., *Phys. Rev. Lett.* **95** (2005).
11. Mannion, J. T., Reccius, C. H., Cross, J. D., and Craighead, H. G., *Biophys. J.* **90**, 4538 (2006).

12. Cabodi, M., Turner, S. W. P., and Craighead, H. G., *Anal. Chem.* **74**, 5169 (2002).
13. Turner, S. W. P., Cabodi, M., and Craighead, H. G., *Phys. Rev. Lett.* **88** (2002).
14. Petrov, A. S. and Harvey, S. C., *Biophys. J.* **95**, 497 (2008).
15. Jun, S. and Mulder, B., *Proc. Natl. Acad. Sci.* **103**, 12388 (2006).
16. Arnold, A. and Jun, S., *Phys. Rev. E* **76** (2007).
17. Brochard, F. and de Gennes, P. G., *J. Chem. Phys.* **67**, 52 (1977).
18. Daoud, M. and de Gennes, P. G., *Journal De Physique* **38**, 85 (1977).
19. Reisner, W., Beech, J. P., Larsen, N. B., Flyvbjerg, H., Kristensen, A., and Tegenfeldt, J. O., *Phys. Rev. Lett.* **99** (2007).
20. Hsieh, C. C., Balducci, A., and Doyle, P. S., *Nano Lett.* **8**, 1683 (2008).
21. Zhang, C., Zhang, F., van Kan, J. A., and van der Maarel, J. R. C., *J. Chem. Phys.* **128** (2008).
22. Turban, L., *Journal De Physique* **45**, 347 (1984).
23. Bakajin, O. B., Duke, T. A. J., Chou, C. F., Chan, S. S., Austin, R. H., and Cox, E. C., *Phys. Rev. Lett.* **80**, 2737 (1998).
24. Perkins, T. T., Smith, D. E., Larson, R. G., and Chu, S., *Science* **268**, 83 (1995).
25. Morse, D. C., *Macromolecules* **31**, 7044 (1998).

CHAPTER 6

NANOFLUIDIC CHANNELS WITH INTEGRATED CARBON NANOTUBE SENSORS

John T. Mannion, Stephen L. Levy, Paul L. McEuen, H.G.Craighead

Abstract. Nanofluidic channels with integrated carbon nanotube sensors are presented as a means for electronically detecting charged molecules in a highly confined environment while allowing for simultaneous fluorescent observation. Using a novel fabrication method, individually addressable, semiconducting, single-walled carbon nanotubes are incorporated into fluid filled channels with depths of 15 – 100 nm and widths of 500 nm. Given appropriate buffer conditions, channels of this size are comparable in depth to the length scale of ionic screening. Thus, it is theoretically possible that charged DNA molecules travelling through the nanochannel will gate the semiconducting nanotube, causing a shift in at constant source drain bias. Devices employing fluid filled channels of this size are also useful in that they allow for confinement induced partial elongation of genomic length DNA molecules.

Introduction

In recent years, nanofabricated, fluid-filled channels and apertures have been investigated as tools for single biomolecule manipulation and detection. Nanochannels and nanoslits in particular have been used for the elongation and observation of fluorescently labeled DNA molecules. Fragment length analysis [1], restriction site mapping [2], and physical mapping of target motifs using bound probes [3] have all been demonstrated as a result of single molecule elongation. Much effort has been invested into understanding the physics of confinement induced elongation.

DNA extension in such environments is due to the fact that critical intramolecular length scales such as radius of gyration (commonly several 100s of nm) and persistence length (typically 60nm) are comparable to the nanochannel diameter or the nanoslit depth (10-100nm) [4]. It is the similarity in the size of the biomolecule and the length scale of the nanofabricated structure that allows for single molecule control. Additionally, hydrodynamic coupling between DNA molecules and channel boundaries becomes more significant as channel size decreases. Greater hydrodynamic friction stabilizes molecules as they are being probed. This is an improvement as compared to the electrical detection of DNA molecules travelling through nanopores [5] for which thermal agitation is a major factor in limiting length measurement resolution.

In addition to improvements in single molecule manipulation using nanochannels, much work has been done in a related area, detection of single molecules using nanotubes and nanowires. These structures have already been shown to serve in the detection of biomolecules, even at the level of single protein binding and dissociation events [6, 7]. The sensitivity of nanowires and nanotubes is attributed to the fact that they are commonly of the same size or even smaller than the molecules which they are detecting. Therefore, single charged and bound biomolecules can cause a shift in charge carrier concentration throughout the entire cross section of the wire. Additionally, for the case of single walled carbon nanotubes (SWCNTs) and DNA, the diameter of the nanotube can be nearly as small as the inter-base spacing in DNA (0.7 and 0.34 nm respectively) and smaller than the width of double stranded molecules (2 nm).

In this report we present a device in which both the nanoscale fluidic channel and the SWCNT are employed. Diagrams depicting the device geometry and experimental procedure are shown in figure 1. An SWCNT sensor, contacted by source and drain electrodes, is built into a nanofluidic channel in such a way that only the middle segment of the nanotube is inside of the channel and in contact with the electrolyte solution. The nanochannel is used to elongate and confine DNA molecules so that, as they are driven through the channel, they must pass within close proximity to the nanotube sensor. The nanotube is used in a field effect transistor mode to detect the perturbation in solution potential caused by the passage of DNA. The change in nanotube conductance is observed by applying a constant source-drain bias voltage and monitoring the current through the tube.

As compared with other nanotube or nanowire biosensing experiments, our approach is novel in that nanotube detectors are employed for the purpose of sensing unbound biomolecules, as opposed to previous reports which demonstrate gating of chemically functionalized nanotubes [8]. In a sense, our planned mode of operation is closer to another set of experiments. It has also been shown in the literature that carbon nanotubes integrated into micron sized PDMS channels can be used to detect shifts in local solution potential induced either by redox reactions at an electrode interface [9], or by streaming potential caused by pressure driven flow of an electrolyte through the channel [10]. This is similar to our experiment in that only a change in the solution potential is responsible for gating the nanotube.

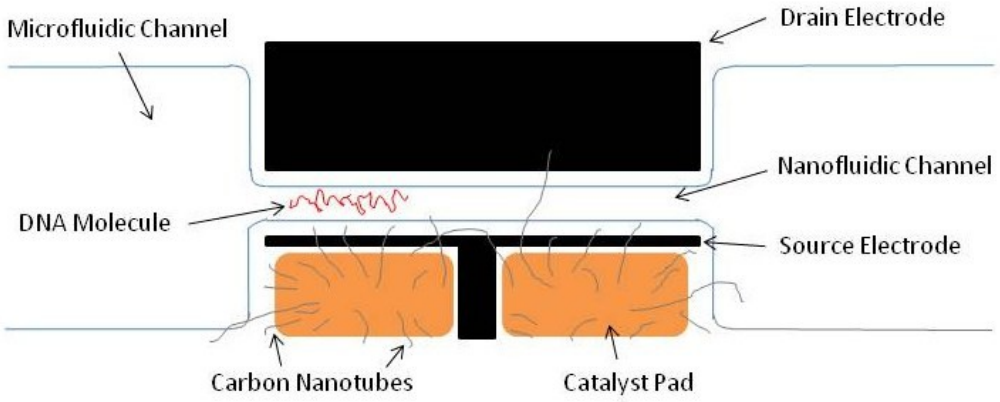

Figure 1. Cartoon diagram showing top down view of device and experimental procedure. The device consists of single walled carbon nanotubes integrated into a nanofluidic channel such that the current through a nanotube can be monitored while DNA molecules are driven through the channel. During fabrication, a chemical vapor deposition method is used to grow nanotubes from metal catalyst pads. As is depicted above, nanotubes grow with a distribution of lengths and directions and in some cases a tube lands such that it connects the source and drain electrodes. A combination of microfluidic and nanofluidic channels is used to guide single DNA molecules toward the connected nanotube. In the initial planned experiment, a molecule is slowly driven through the nanochannel. When its position coincides with an electrically connected semiconducting nanotube, the nanotube conductance is altered by means of field effect gating.

Theory

Double stranded DNA in physiological solution is a highly charged macromolecule, with an estimated surface potential of order $-100mV$ [11]. In an ionic solution, rearrangement of mobile charge carriers serves to screen the large surface potential of DNA over a characteristic length scale termed the Debye screening length. It may be for this reason that previous attempts to detect DNA with nanotubes or nanowires have

focused on cases in which the DNA molecules are bound to the surface of the detector. Nanowire and nanotube detectors have yet to sense unbound charged macromolecules as they freely drift by the detectors in solution. In this report we design and fabricate a device in which DNA molecules driven through a nanochannel are forced to pass close enough to the nanowire detector such that the solution potential at the location of the detector is perturbed (Figure 2).

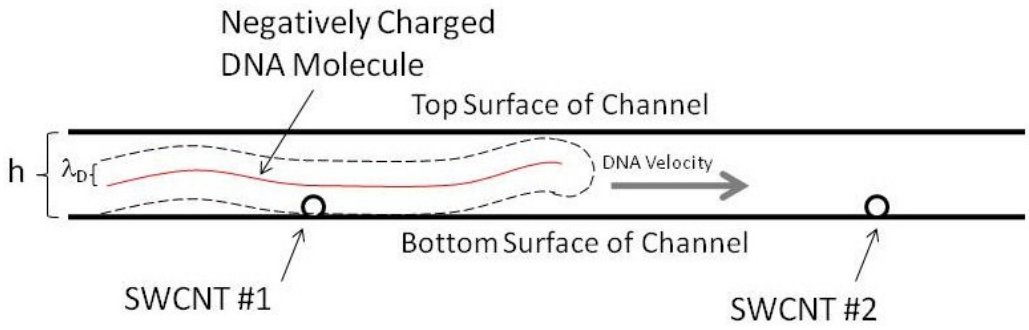

Figure 2. Side view of nanochannel device with cartoon of an elongated DNA molecule in the channel. Two single walled carbon nanotubes (circular cross section shown) run perpendicular to the axis of the nanochannel and the image plane. They are contacted by two source and drain electrode pairs which are not shown here. A DNA molecule travelling through the channel moves from left to right in the image. The negatively charged DNA molecule (red) is surrounded by a cloud of positively charged ions. At a distance y from the DNA backbone, the solution potential is perturbed by an amount $\Delta\varphi_{DNA} = \zeta \cdot \exp(-y/\lambda_D)$ from its bulk value. A perturbation of potential at the nanotube surface gates the device, affecting its conductance. This is measured as a change in current at constant source drain voltage.

In an electrolyte solution, near the surface of a charged object, the electric potential transitions from the zeta potential (electric potential of the immobile ions fixed to the

surface) to the bulk solution potential over a distance which depends on the ionic strength of the solution. A convenient parameter for describing that drop in potential is the Debye screening length, λ_D, which is defined by the expression $\lambda_D \equiv \sqrt{(\varepsilon RT)/2F^2(\Gamma/2)}$ where $\Gamma/2$ is the ionic strength of the solution. Using the Debye-Huckel approximation, the shift in electrolyte potential a distance, y, from the DNA surface is then given by $\Delta\varphi_{DNA} = \zeta \cdot \exp(-y/\lambda_D)$.

In the described devices, carbon nanotubes are located close enough to the backbone of confined DNA molecules so as to avoid significant charge screening. For a carbon nanotube fixed to the bottom surface of the nanochannel, and a DNA molecule elongated in the channel and positioned above the nanotube, the average nanotube/DNA separation distance is roughly half of the height of the channel. Given a DNA zeta potential of $100mV$, an ionic screening length of $10nm$, and a channel depth of $50nm$, we expect a perturbation in solution potential on the order of $10mV$ at the location of the nanotube. In theory, fluctuations in the conformation and vertical position of the DNA molecule due to thermal agitation may cause fluctuations in potential near the nanotube sensors. It is assumed, however, that such fluctuations occur on a timescale which is short compared with the duration of the measurement, thus they can be ignored.

Having estimated the magnitude of the potential shift caused by a DNA molecule, we now calculate the change in nanotube conductance that results. For semiconducting CNTs in solution high mobilities, low contact resistances, and good gate coupling are possible (double layer capacitance of $4\times10^{-9}F\cdot m^{-1}$), leading to an electrolyte gated transconductance of $\sim e^2/h/V$ [12]. Applying an electrolyte gate voltage of $10mV$ should result in a conductance change of order $0.01V \cdot e^2/h/V = 387nAmp \cdot V_{SD}^{-1}$. This

is an upper bound, however, as it assumes the potential along the entire length of the nanotube has been shifted by $\Delta\varphi_{DNA}$. In fact, given the current device design, and a ionic screening length of roughly $10nm$, only a fraction of the length of the nanotube will be affected by the DNA potential . Even so, it is not unreasonable that such a perturbation in solution potential could be detected. Much work has been done on scanning gate microscopy of carbon nanotubes [13-16], which supports this notion. The reported results suggest that local gating of nanotubes from scanning probe AFM tips can affect nanotube conductance even when the affected length of the tube is on the order of $10's$ of nm [14]. While it was reported that the strongest gate coupling effects occur near the contacts, the tube may also be gated to varying degrees anywhere along its length. For our devices, the way in which DNA gating is expected to modulate nanotube band structure is illustrated in figure 3.

Support for this band structure modulation is given by previous work on detailed investigations into the mechanism of electrolyte gating for nanotubes. Over the past several years, a number of theories have been proposed to explain the mechanism of nanowire transconductance in electrolyte solution, for a detector design such as the one shown in figure 4A. Schottky barrier modulation, electrostatic gating of nanotube carrier density, capacitance effects between the nanotube surface and the solution, and decreased electron mobility through the nanotube have all been proposed. Recently, in a paper by Dekker et al. it was argued that, according to theory, each of these mechanisms should affect the $I \cdot V_{\mathrm{lg}}$ (current vs. liquid gate) curve in a qualitatively distinct way [17]. A comparison of experimental data with models for the four different mechanisms suggests that electrostatic gating of carrier density and Schottky barrier effects are primarily responsible for conductance changes upon biomolecule binding for the setup shown in figure 4A. Furthermore, when the contacts are covered

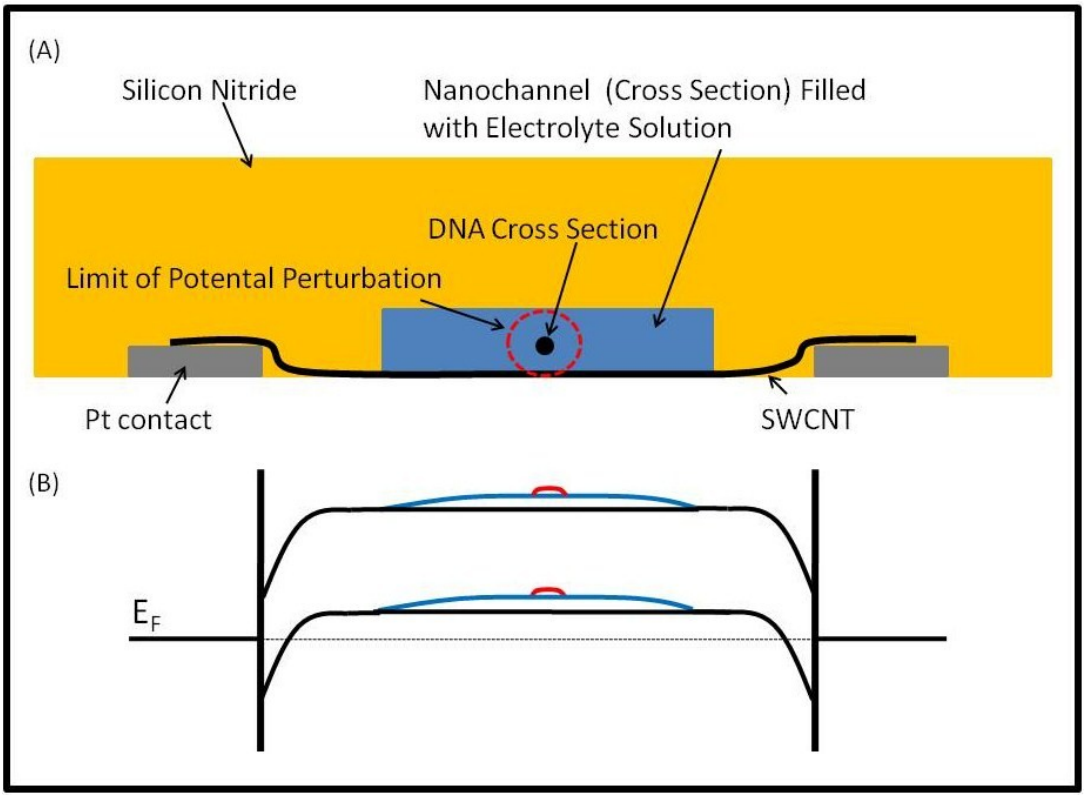

Figure 3. A) Cross sectional diagram of a nanofluidic channel with integrated nanotube sensor device. The source and drain contacts to the carbon nanotube are buried under an insulating layer of silicon nitride. The nanofluidic channel confines the electrolyte solution over the central part of the nanotube only, and forces the DNA molecule to reside at a vertical position which is close to the nanotube. Due to the fact that the channel width is larger than its depth, the DNA molecule has more freedom in the lateral dimension. **B)** Band diagram of a p-type nanotube integrated into the device. If the solution potential is more negative relative to the source and drain electrodes, then the blue correction to the band diagram results. If the potential from the DNA molecule is significant enough, a second perturbation (red curve) will exist in the conduction and valence bands.

as in figure 4B, and only a portion of the SWCNT is exposed to solution, the affect of biomolecule binding on $I \cdot V_{lg}$ is shown to be consistent with the model for gating of carrier density in the nanotube. The latter situation is most similar to our device, for which the nanotube/platinum contacts are imbedded under a silicon nitride film and only a central portion of the nanotube is in contact with the solution. Eventually, DNA molecules, as they are driven through the channel, will also be confined to interact with the exposed central segment of the nanotube only.

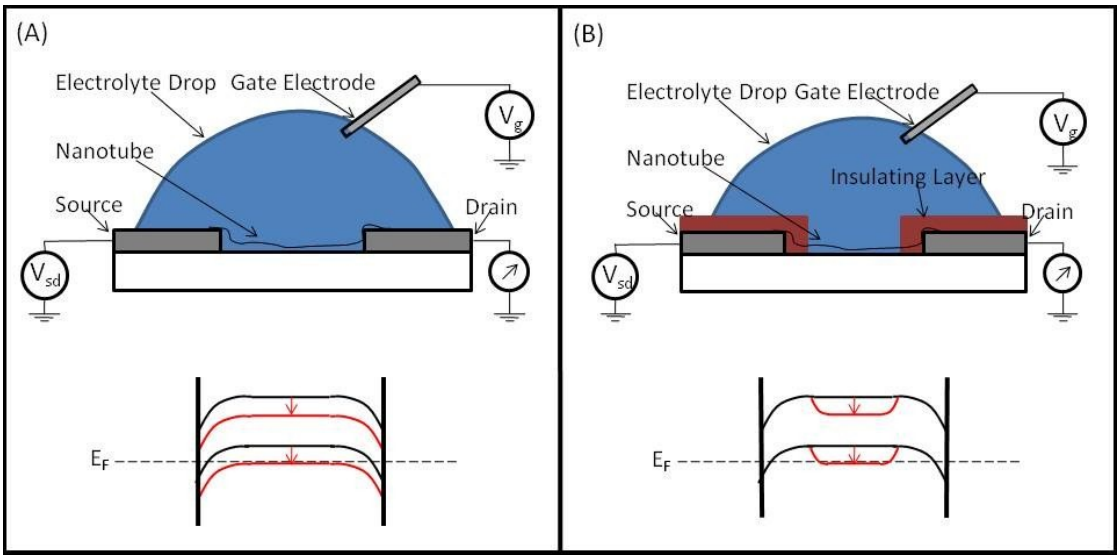

Figure 4. Diagrams illustrating the setup for electrolyte gate sweeps of carbon nanotubes, and the resulting effects on band structure, adapted from results reported in the literature [17]. The black band diagrams indicate an ungated, p-type nanotube. The red diagrams depict a shift toward depletion as the gate voltage is made more positive relative to the source and drain. **A)** Unprotected nanotube source-drain contacts. In this case, both Schottky barrier modulation and carrier density gating were found to be responsible for modulating the nanotube conductance. **B)** Nanotube source drain contacts electrically isolated from the solution by some insulating layer. For the situation, the Schottky barrier modulation may be eliminated as a possible mechanism of nanotube conductance modulation.

Materials and Methods

Device Fabrication

In order to combine leak free, nanoscale fluidic channels with functioning carbon nanotube transistors, a novel fabrication process was developed which employed standard photolithographic and MEMs processing techniques available at the Cornell Nanofabrication Facility, and carbon nanotube growth processes available at Cornell University in the lab of Professor Paul McEuen. An overview of the device fabrication is given here with further details available in the Chapter 7. For this device, a sacrificial layer method is used to create channels with integrated electronic elements.

Initially, an alignment mark level was patterned and etched into $170\mu m$ thick and $100\,mm$ diameter fused silica wafers (Mark Optics). Next, patterned layers of Ti/Pt (thicknesses $4nm/30nm$) for contact electrodes and Al2O3/Co (15nm/3Å thicknesses) for catalyst pads were deposited on separate layers using a combination of photolithography, e-beam evaporation and lift off. The wafers were then diced into chips using a KS 7100 Wafer Saw. After this, carbon nanotube growth was performed on individual chips using a chemical vapor deposition (CVD) process at 800C with ethylene as the carbon source precursor. A thin layer (thickness $10-30nm$) of low stress nitride was conformally deposited on top of the chromium using a plasma enhanced chemical vapor deposition tool. This thin nitride layer protects the nanotubes from reaction with chromium etchant during the sacrificial layer wet etch step. A patterned layer of chromium, of thickness $10-50nm$ was then deposited using a combination of photolithography, e-beam evaporation and lift off. This

patterned chromium layer is the sacrificial material for what will be a network of micro- and nano-fluidic channels in the end.

Following chromium deposition, a second layer of low stress nitride of thickness $\sim 2\mu m$ was deposited using PECVD. Vias were then created along the length of the channels for wet etchant access to the chromium, and over the Pt pads for needle contact. These access holes were defined using photolithography and dry etching (CHF3/O2) in an Oxford 80 Reactive Ion Etch (RIE) Machine (Oxford). After photoresist stripping, chips were submerged in CR-14 Chrome Etchant (Cyantek) for $3-6hrs$, during which time the liquid etchant travelled through the access holes and removed the sacrificial layer of chromium. Chips were soaked in dH_2O and then IPA (15min in each) and then dried with N_2. At this point CNT conductances were checked. The thin layer of protective nitride separating the CNTs from the channel was etched away by submerging chips in MF 312 (5% TMAH) at 70C for anywhere from 15 to 45 min, depending on the protective nitride layer thickness. Following this, chips were soaked in dH_2O and then IPA (15min in each) and dried again with N_2. A third and final layer of low stress silicon nitride of thickness $500nm$ was deposited. This layer served to seal the etchant access holes along the length of the micro and nanochannels. Finally the newly deposited 500 nm thick nitride film above the Pt pads was removed using a combination of photolithography and dry etching to allow for probe needle contact. After stripping resist off of the chip surface, entrances were created at the end of the six microchannels by lightly scratching the nitride with a diamond scribe, and macroscopic reservoirs were aligned by eye and affixed to the chip above the microchannel entrances.

Setup

Optical setup. Fluorescence observation of single DNA molecules in nanochannels was performed with an IX71 inverted microscope (Olympus, Melville, NY), equipped with a 100x/1.35 NA oil immersion objective (Olympus). Images were acquired using a Cascade 512b EMCCD (Photometrics) at 10 frames per second using custom software (Christian Reccius, former Post-doc Craighead group) written in Labview (National Instruments). Videos were saved as a series of .tif files and analyzed using a custom MATLAB program (Reccius and Levy).

Electrical Setup. In order to simultaneously monitor nanotube conductances while visualizing DNA molecules near the tubes, an electrical setup was assembled with the optics as shown in figure 5. Pt electrodes were placed in the fluid reservoirs and were used to electrokinetically drive DNA molecules through the channels. In the future these Pt electrodes are to be replaced by Ag/AgCl reference electrodes during detection for reasons described in the results and discussion section. Between two and four probe manipulators (Quarter Research, Bend, Oregon) were attached to the stage using vacuum mounts, and these were used to place probe needles in contact with the source and drain electrode pads. Source electrode voltage was interfaced to a DAC and controlled using a freeware LABVIEW program MeasureIt.vi (McEuen wiki online). Current between the drain electrode and ground was monitored using an Ithaco 1211 current preamplifier (DL Instruments, Ithaca, NY), whose output was fed to an ADC and recorded using the same LABVIEW program. The current preamplifier gain was set between 10^7 and 10^9 and the time constant between $3ms$ and $100ms$. Sampling rates were set to be equal to or less than the inverse of the time constant, ensuring statistical independence of recorded measurements.

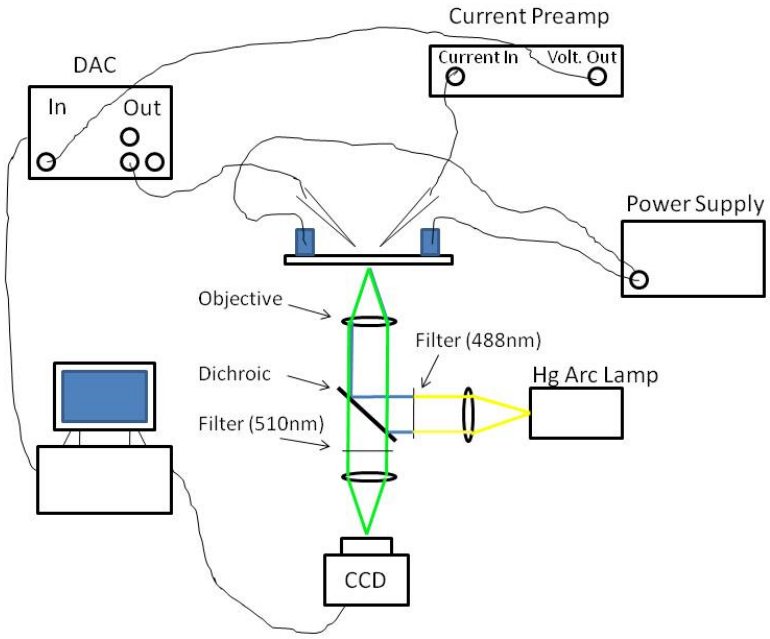

Figure 5. Experimental setup for simultaneous optical and electrical detection.

Results and Discussion

Measurement of CNTs in Air

In order to verify the presence of carbon nanotubes throughout the fabrication process, device conductances were recorded after initial CNT growth while the tubes were still exposed to air. Each of the thirty eight source and drain electrode pairs on each chip could be individually address and tested for tubes. Because of the random nature of carbon nanotube growth with CVD, it was not known a priori how many nanotubes bridged the gap between each source and drain electrode. Immediately after growth, some electrode pairs exhibited no current in response to a source drain bias, and these were considered to have no nanotube bridging the gap between the electrodes. Although it is conceivable that in those cases an SWCNT was there but was simply

depleted of charge carriers, this is believed to only rarely have been the case. This is based on many subsequent measurements in which water gates were used. Most of the time, if a tube was present, at least some small current could be detected at large source drain bias. If there existed a current, it was assumed that one, or more than one nanotube bridged the gap. For most of the chips, more detailed information was not obtained regarding tube growth at this stage. Each chip was simply characterized by the number of connected source drain electrode pairs. If at least a few were connected, then processing steps were continued on that chip. Depending on the wafer or CVD growth run, the majority of chips in a run had between 5 and 30 connected electrode pairs, out of a possible 38. The I-Vsd curves for the majority of connected electrode pairs showed device resistances ranging from $100 k\Omega$ to $10 M\Omega$, with mean square current noise densities of $10^{-17} Amp^2 / Hz$ to $10^{-15} Amp^2 / Hz$ at a source drain bias of 10 mV. Following deposition of the nitride capping layer on the tubes, the conductances were observed to change. This was attributed to charges associated with the nitride/nanotube interface [18-20]. Additionally, the noise level for many nanotubes appeared to go down. This was also attributed to the direct contact between nitride and nanotubes. Due to the fact that no metal gate existed on the chips, it was challenging to properly analyze the shifts in conductance. While a water gate could be used before nitride deposition, water gating appeared to be ineffective even after a small amount of nitride had been deposited.

Electrolyte Gated Measurements

Nevertheless, a comparison of water gating response could be made between tubes that were just grown, and those that were in fully fabricated devices (where the protective nitride layer had been removed and part of the tube was in contact with the nanochannel buffer). CNT devices with exposed surfaces could be investigated using

an electrolyte gate as was first demonstrated for multiwalled nanotubes [21] and later for single walled nanotubes [12]. Source and drain electrodes were contacted in the normal way, but a drop of salty water was placed directly on top of the nanotubes and this electrolyte solution was then gated with a Pt or Ag electrode, as was previously illustrated in figure 4A. In this way, the electrolyte potential was swept between $-800mV$ and $+800mV$ relative to the drain potential. Gate potentials beyond about $\pm 1V$ were observed to destroy the nanotube devices, an effect which is attributed to electrochemical oxidation or reduction of the electrodes, or of the nanotube itself. Typical I-V curves for a semiconducting device are shown in figure 6.

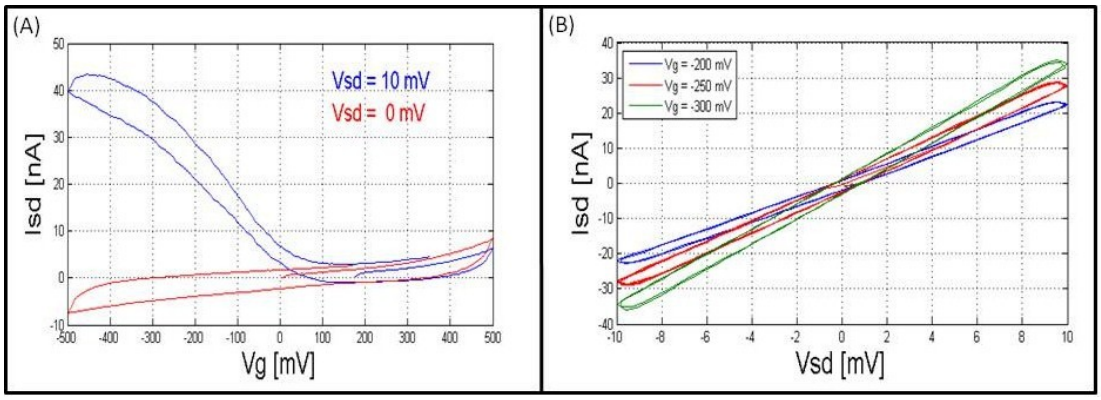

Figure 6. A) Source drain current vs. electrolyte gate sweep for two source drain voltages. For $V_{SD} = 0$, the measured I is entirely due to I_{GD}, the electrochemical leakage current between gate and drain electrodes. A gate sweep which goes from a positive to a negative value and loops is equivalent to a cyclic voltamogram in the electrochemistry literature. The shape of the curve is determined by either mass transport or electron transfer kinetics and is a function of sweep rate among other parameters [22]. For a given sweep rate and electrode surface area, the leakage current may be measured, as is shown above, and later subtracted. **B)** Plot of current vs. source-drain voltage for three differed gate potentials. It is apparent from these curves that a shift in gate potential on the order of 50mV can easily be measured.

It was common for a single carbon nanotube device to exhibit ambipolar behavior. At zero and negative gate voltage, these nanotubes were often p-type. The application of a large positive gate voltage resulted in n-type behavior. In accordance with previously defined metrics for characterization of semiconducting nanotubes, our devices can be characterized by a transconductance value for both the n-type and p-type regions.

For electrolyte gate sweeps, the measured current, I , is a sum of the current between the source and the drain I_{SD} and the leakage current between the gate and drain electrodes I_{GD}. Each of these components can be broken down further. The source drain current is the sum of the electrical current passing through the nanotube and the ionic current between the source and drain electrodes. The gate-drain current is the sum of the current between the gate and the exposed area of the drain electrode surface, and the gate and nanotube. Depending on the values of V_G and V_{SD}, and the electronic properties of the nanotube, one of the possible contributions to total current may dominate at a given time.

When initially analyzing the data for completed devices with nanotubes, it was believed that there was a small leakage current caused by either: 1) electrolytic current between the gate and drain that was travelling through inter dielectric layer spaces caused by nanotube topology, or 2) a leakage current between the gate the carbon nanotube surface directly. Looking carefully at the Vsd = 0 data in figure 7 reveals some small negative current at large gate values. This appeared to support the notion of a small leakage current.

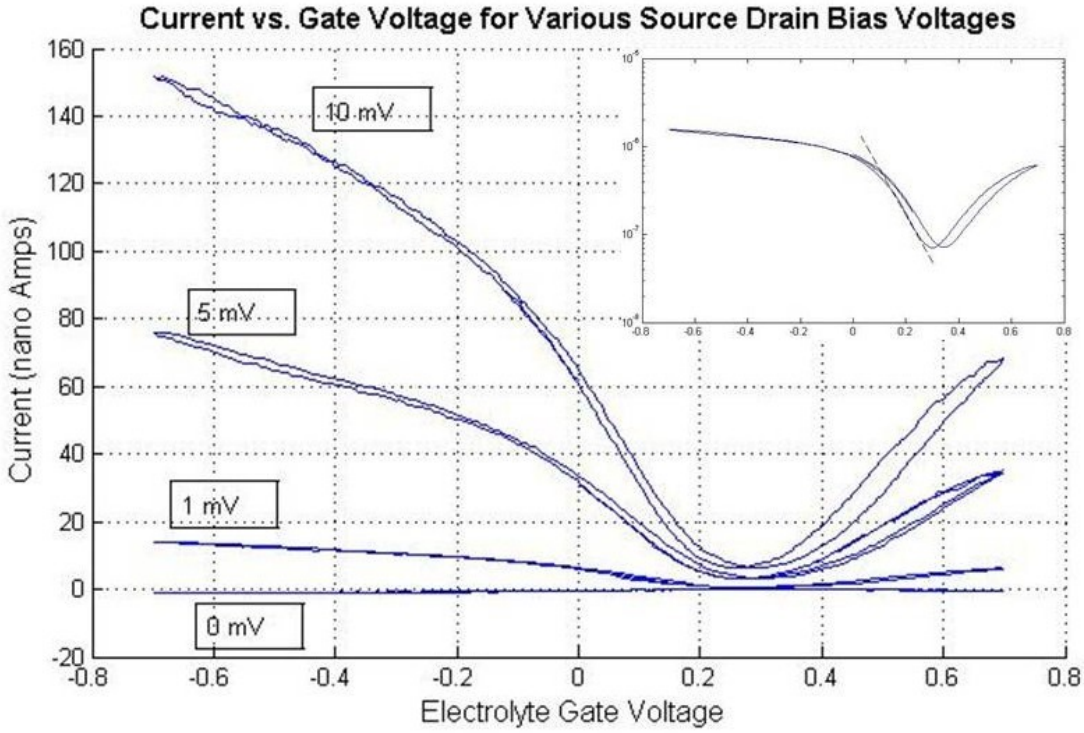

Figure 7. Main) Current versus electrolyte gate voltage at a variety of source-drain biases for a nanotube integrated into a nanochannel device. This particular nanotube shows ambipolar behavior. At its highest the transconductance is approximately $25\mu S/V_G$. **Inset)** Semilog plot of current versus gate at 100mV source drain bias. The exponential decay is characterized by a subthreshold swing (inverse of slope of dashed line) of S = 185 mV / decade.

After a more detailed investigation, it was discovered that, for fully fabricated devices, the observed current at zero source drain bias current was not a leakage current at all. It appears instead to have been the result of an ambient voltage difference between the source and drain electrodes. Despite the fact that the source electrode was set to zero volts, it must have differed from the drain potential by some small negative voltage. The small bias then resulted in a current which was modulated by the gate potential, but which was not a result of leakage between the gate and the drain. Evidence for

this is given in figure 8 and the panels of figure 9. Figure 8 shows the difference in gate-drain leakage current for buried versus exposed electrodes, and figure 9 shows the gate sweeps for four different devices where the nominal source drain biases were set to 0 mV and 10 mV.

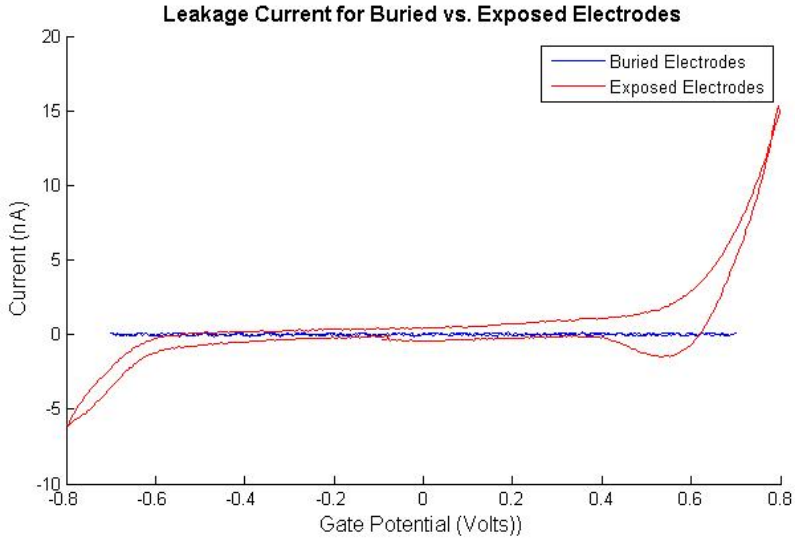

Figure 8. Leakage currents between the gate and drain electrodes for two separate devices. The red data set is for a partially fabricated device, where the source and drain electrodes are exposed, and in contact with the electrolyte as in the diagram of figure 4A. The blue data set is for a fully fabricated device, where the source and drain electrodes are buried under silicon nitride and are separated from the electrolyte solution, as depicted in figure 3. Both of devices measured here were believed to have no nanotube connecting the source and drain electrodes. While the plots shown are for a bias of 100 mV, the current response is nearly identical to this for biases of 0 mV, 1 mV, and 10 mV. The main result here is the difference in leakage current for buried vs. exposed electrodes. No gate drain leakage current for the buried electrodes is apparent. For the exposed electrode, the leakage current takes the form a cyclic voltammogram, as expected for mass transport limited heterogeous reactions.

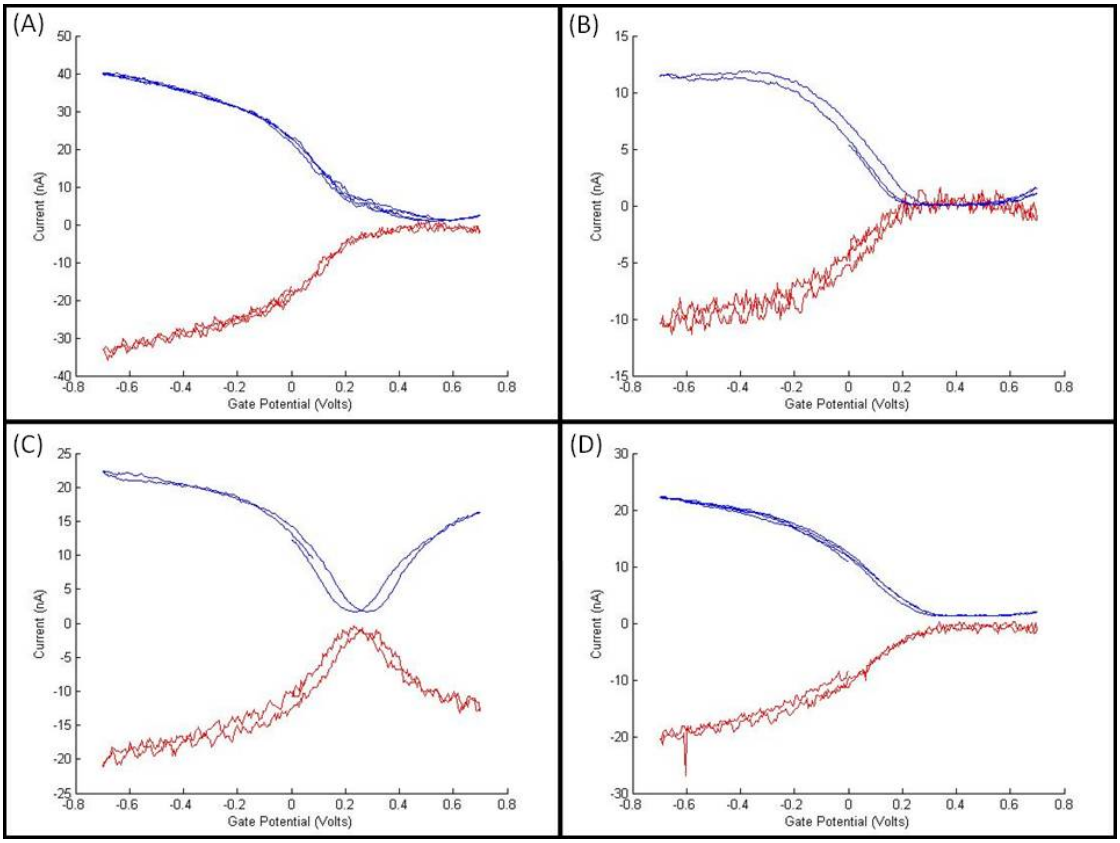

Figure 9. Plots of current versus gate potential for four different source drain electrode pairs for a fully fabricated device (i.e. contact electrodes covered by nitride). Each pair investigated here evidently has either one or more semiconducting carbon nanotubes connected. The blue data sets are for a nominal source-drain bias of 1 mV. The magnitude of the current for the blue data sets is given on the y-axis. The red data sets are for a nominal source-drain bias of 0 mV. The red data set values have been multiplied ten times in order for ease of viewing. Thus, the maximum currents recorded for the red data sets in A, B, C, and D were -3.3 nA, -1 nA, -2 nA, and -2 nA. It appears that there was a small ambient offset source drain voltage of around -0.1 mV, which was not understood as such until long after data was taken. Evidence suggests that there was little, if any, leakage current.

Fluorescence Video of DNA Near Nanotube

Fluorescence video was taken of DNA molecules travelling through nanochannels under electrophoretic motion. Single T4 molecules (120 kbp in length) and fragments could be readily observed and quickly driven to the nanotube region of the device (see figure 10). Once there, the molecules could be positioned using small voltages. It is hoped that this level of control will allow for a DNA molecule to be positioned so that it rests directly above a nanotube for an extended period of time, while the nanotube conductance is monitored.

Factors Contributing to Electronic Noise

As a first step in determining the noise floor of our system, we estimate the current noise inherent to liquid gated carbon nanotube transistors. Due to the nature of our planned DNA detection approach, we are most interested in the low frequency noise power (approximately 1 Hz and lower). Much research on the noise properties of SWCNTs has been performed and $1/f$ noise has been demonstrated. The noise spectra of the source drain current, I, as a function of frequency, f, has typically been interpreted from the point of view of the Hooge model [23]. In this model, noise is caused by independent scattering events of charge carriers. Recently Mannik et. al have interpreted $1/f$ noise in nanotubes differently, using a charge-noise model [24]. In this model, low frequency noise is caused by charge fluctuators which are either near the nanotube or which transiently associate with the nanotube surface. Examples of such charge fluctuations may be dissociation of hydrogen from silanol groups on a substrate surface near the nanotube, or adhesion of an ion in solution to the nanotube surface. This implies that the current-noise power, $S_I(f)$, should be proportional to a factor describing the magnitude of charge fluctuations, S_{input}, multiplied by the square

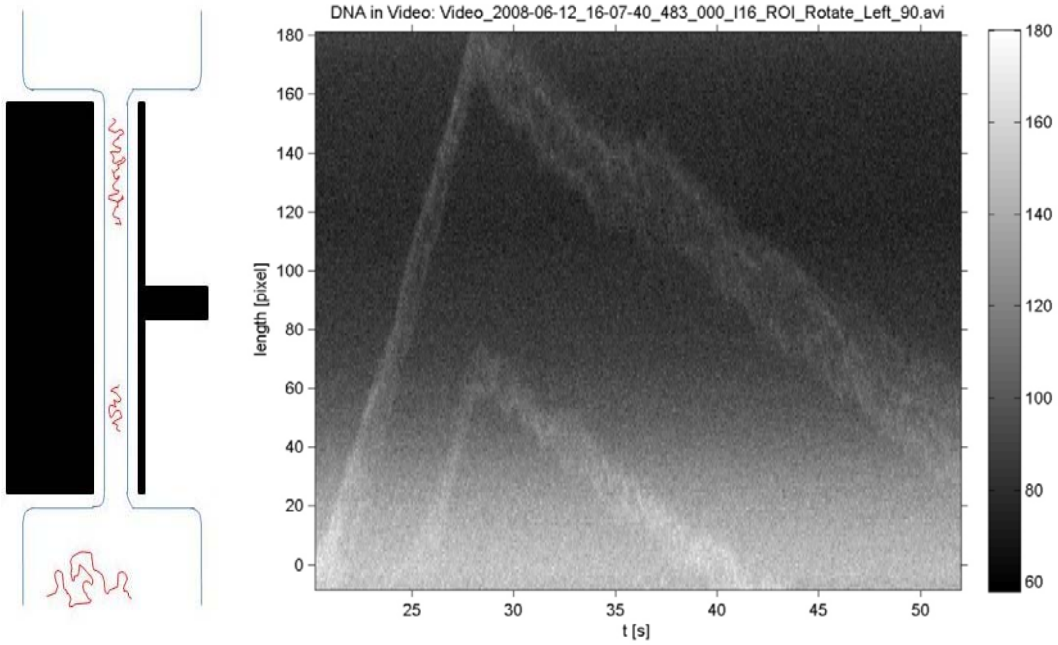

Figure 10. A) Cartoon diagram of DNA molecules in and near the nanofluidic channel region of the device. In this diagram, two molecules are in the channel at the same time. By applying a small voltage (~1V), the molecules may be slowly driven up or down in the channel. **B)** Time trace diagram of two DNA molecules in a nanochannel of a carbon nanotube sensor device. The first molecule enters the channel at time $t = 0$ sec. and the second molecule enters at $t = 25$ sec. At $t = 29$ sec, the direction of the electric field is reversed, causing the two molecules to change their direction of migration.

of the nanotube transconductance $\left(dI/dV_G\right)^2$. In addition to showing that the low frequency noise spectra is governed by charge-noise phenomena, Mannik et al. demonstrate a dependence of noise power on nanotube length. They show that $S_I(f) \propto 1/L$ holds for nanotubes of $2nm$ diameter, with lengths ranging from $60nm$ to $3.4\mu m$, a range of sizes within which our nanotubes fall. To obtain an order of magnitude estimate for our nanotube sensor devices we refer to the 440nm long CNT

sensor studied in [24]. For a 1 Hz bandwidth and a source drain voltage of $10mV$, they find a current noise spectral density at $f = 1Hz$ which varied from 10^{-26} to 10^{-18} Amp^2/Hz as the liquid gate potential was swept. This corresponds to an RMS uncertainty in the current of between approximately .5 pA and 5nA for a source drain bias of $V_{SD} = 10mV$ and a rise time of 30msec.

As a second source of noise, we consider that the nanochannel and microchannel fluidic system connecting the macroscale fluidic reservoirs acts as a resistor. The voltage variance per hertz of bandwith attributed to Johnson noise is given by $\upsilon_n^2 = 4k_B TR$. In order to calculate the voltage variance at the location of the nanotubes, resistances of the various parts of the fluidic system can be calculated using geometrical considerations and known values for buffer resistivity. We conceptualize a simple case in which a single nanotube is located at the center of a nanochannel which is connected to microchannels in series only. We assume a buffer resistivity ρ and a resistance for each channel segment given by $\rho \cdot g$, where $g = l/(d \cdot w)$ is a geometrical factor with l, w and d equal to the channel segment's length, width and depth respectively. All channels in our model are of the same depth, which is set to $d = 100nm$ in this calculation. For purposes of the calculation, we assume the first microchannel is 5 mm long and 30 um wide. The second microchannel is 1 mm long and 5 um wide, and the nanochannel is 15 um from the end to its middle, and is 500 nm wide. Thus the geometrical factors are $g_1 = 1.7 \times 10^9 m^{-1}$, $g_2 = 2 \times 10^9 m^{-1}$ and $g_3 = 1 \times 10^9 m^{-1}$.

At low ionic strength, the resistivity for an electrolyte in a nanoscale channel, ρ_{nano}, differs from the bulk resistivity, ρ_{bulk}, by an appreciable amount, as was recently reported by Stein et. al [25]. Stein investigates channels with depths ranging from

$70nm$ to $1015nm$ and observes that channel conductance decreases with depth and with ionic strength. He also reports a conductance saturation level at very low ionic strength, an effect which is explained by the dominance of surface charge governed ionic transport. It is in this concentration regime which we expect to operate. We therefore use his reported value in our resistivity estimate. Given that saturation conditions are satisfied, $\rho_{nano} \cdot d \approx 2 \cdot 10^8 \Omega \cdot (width / length)$ regardless of channel height. Using this value, we estimate the total resistance for our channels, assuming that ionic strength is low enough that surface governed ionic transport dominates conductance. Given our channel geometry, we find that $R = (\rho \cdot d) \cdot L \cdot w^{-1} = (2 \cdot 10^8 \Omega) \cdot (10^{-3} m / 10^{-5} m) = 2 \cdot 10^{10} \Omega$. Thus, at the location of the nanotube, the voltage variance per hertz of bandwidth attributed to thermal motion of fluid in the channels is $\upsilon_n^2 = 4k_B TR = 3.3 \times 10^{-10} V^2 Hz^{-1}$. Through field effect, this translates to a Johnson induced current noise of

$$S_J(f) = \upsilon_n^2 \cdot (dI / dV_{\lg})^2 = 3.3 \times 10^{-10} \cdot (3.87 \times 10^{-5})^2 \approx 50 \times 10^{-20} Amp^2 / Hz$$

at $V_{SD} = 10mV$, where the frequency dependence is trivial since thermal agitation across a resistor leads to a white noise spectrum. Note that our actual system of channels is more complicated in that there are six reservoirs as opposed to two (see Chapter 7). There are also six microchannel loading arms leading to each of the reservoirs, and nineteen nanochannel branches in parallel. Nevertheless the simple case that we have considered gives a rough estimate of the Johnson noise for this type of fluidic system, and from that we have obtained an estimate of its contribution to nanotube current noise.

As a third contributor to current noise, we consider the interface between the reservoir electrodes and the buffer. It is known that chemical interactions at an electrode

interface can cause additional variations in solution potential. This was recently investigated extensively by Dekker et al [26]. Dekker shows that, when performing biosensing measurements with carbon nanotubes, it is critical to use a reference electrode separated from the solution by a frit in order to accurately control the solution potential. He points out that many previously reported nanowire biosensing experiments employed bare electrodes in solution, which can lead uncertainty in knowledge of solution potential over time. For example, for a Pt electrode immersed in bovine serum albumin with target protein molecules, interactions at the electrode surface can cause shifts in global solution potential on the order of 20-40 mV.

In our case, one might imagine that aggregates of DNA molecules, pieces of crystallized salt, or other particles diffusing in the macroscopic reservoir might interact with a bare electrode and cause a similar shift in global solution potential. Because the "signal" perturbation from our DNA molecule is only expected to be on the order of 10 mV, it is clear that interactions between electrode surface and solution impurities must be avoided. To prevent this, we intend to use Ag/AgCl reference electrodes, immersed in a highly concentrated AgCl solution and separated from the bulk solution in the reservoir by a frit. While we have not directly tested this yet, it has been reported that such a reference electrode can hold the solution potential steady to within 1mV. Thus we estimate that the effect of reference electrode / solution-impurity interactions contribute 1mV RMS fluctuations in background noise, leading to a current noise PSD of $S_E(f) = (1mV)^2 \cdot \left(dI/dV_{\lg}\right)^2 = 15 \times 10^{-14} Amp^2/Hz$ at $V_{SD} = 10mV$.

As a final possible source of noise, we consider the measurement equipment itself. We note that the preamp gain is selected to be significantly larger than the source

dynamic impedance, R_d, to keep the preamp from adding substantially to the source noise. For a gain of 10^7 and a rise time of $1 m\text{sec}$ the nominal preamp current noise is on the order of $50\ fA$ [27]. This is much smaller than the noise from any of the other sources. Other factors such as 60Hz pickup and acoustic vibrations are also likely contributors to noise. However, we do not estimate these here as they depend largely on the details of the setup. It assumed that, with effort, their noise contribution could be made smaller than that of other sources of noise considered above.

Conclusion

The integration of carbon nanotube sensors into nanofluidic channels represents a first step in electrical detection of unbound biomolecules. In this report, we have described a novel device design and fabrication method for achieving this integration. We have also performed initial characterization of the optical and electrical properties of the device. It was shown that single DNA molecules could be observed and manipulated in the detection region using a combination of electrokinetic driving forces and real time fluorescence video microscopy. It was further shown that SWCNTs, built into a nanochannel, could be gated through modulation of the solution potential. The gating characteristics differ from those of tubes on an open surface. Due to covering of the source and drain electrodes, leakage currents were reduced to a level that is below the noise. Final steps in this experiment are underway. More nanotube devices are currently being fabricated. It is hoped that they will allow for an experiment in which a single DNA molecule is slowly driven over a nanotube, and a change in nanotube conductance results.

REFERENCES

1. Reccius, C.H., et al., *Conformation, length, and speed measurements of electrodynamically stretched DNA in nanochannels.* Biophysical Journal, 2008. **95**(1): p. 273-286.
2. Riehn, R., et al., *Restriction mapping in nanofluidic devices.* Proceedings of the National Academy of Sciences of the United States of America, 2005. **102**(29): p. 10012-10016.
3. Phillips, K.M., et al., *Application of single molecule technology to rapidly map long DNA and study the conformation of stretched DNA.* Nucleic Acids Research, 2005. **33**(18): p. 5829-5837.
4. Tegenfeldt, J.O., et al., *The dynamics of genomic-length DNA molecules in 100-nm channels.* Proceedings of the National Academy of Sciences of the United States of America, 2004. **101**(30): p. 10979-10983.
5. Healy, K., B. Schiedt, and A.P. Morrison, *Solid-state nanopore technologies for nanopore-based DNA analysis.* Nanomedicine, 2007. **2**(6): p. 875-897.
6. Patolsky, F., G. Zheng, and C.M. Lieber, *Nanowire sensors for medicine and the life sciences.* Nanomedicine, 2006. **1**(1): p. 51-65.
7. Patolsky, F., G.F. Zheng, and C.M. Lieber, *Nanowire-based biosensors.* Analytical Chemistry, 2006. **78**(13): p. 4260-4269.
8. Katz, E. and I. Willner, *Biomolecule-functionalized carbon nanotubes: Applications in nanobioelectronics.* Chemphyschem, 2004. **5**(8): p. 1085-1104.
9. Larrimore, L., et al., *Probing electrostatic potentials in solution with carbon nanotube transistors.* Nano Letters, 2006. **6**(7): p. 1329-1333.
10. Bourlon, B., et al., *A nanoscale probe for fluidic and ionic transport.* Nature Nanotechnology, 2007. **2**(2): p. 104-107.

11. Wagner, K., et al., *Analytical Debye-Huckel model for electrostatic potentials around dissolved DNA.* Biophysical Journal, 1997. **73**(1): p. 21-30.
12. Rosenblatt, S., et al., *High performance electrolyte gated carbon nanotube transistors.* Nano Letters, 2002. **2**(8): p. 869-872.
13. Bachtold, A., et al., *Scanned probe microscopy of electronic transport in carbon nanotubes.* Physical Review Letters, 2000. **84**(26): p. 6082-6085.
14. Freitag, M., et al., *Controlled creation of a carbon nanotube diode by a scanned gate.* Applied Physics Letters, 2001. **79**(20): p. 3326-3328.
15. Kim, Y., et al., *Mapping potential landscapes of semiconducting carbon nanotubes with scanning gate microscopy.* Nanotechnology, 2007. **18**(47).
16. Zhang, L.M. and M.M. Fogler, *Scanned gate microscopy of a one-dimensional quantum dot.* Nano Letters, 2006. **6**(10): p. 2206-2210.
17. Heller, I., et al., *Identifying the mechanism of biosensing with carbon nanotube transistors.* Nano Letters, 2008. **8**: p. 591-595.
18. Chen, B.H., et al., *A carbon nanotube field effect transistor with tunable conduction-type by electrostatic effects.* Solid-State Electronics, 2006. **50**(7-8): p. 1341-1348.
19. Kojima, A., et al., *Air stable n-type top gate carbon nanotube filed effect transistors with silicon nitride insulator deposited by thermal chemical vapor deposition.* Japanese Journal of Applied Physics Part 2-Letters & Express Letters, 2005. **44**(8-11): p. L328-L330.
20. Mizutani, T., et al., *Effects of fabrication process on current-voltage characteristics of carbon nanotube field effect transistors.* Japanese Journal of Applied Physics Part 1-Regular Papers Short Notes & Review Papers, 2005. **44**(4A): p. 1599-1602.

21. Kruger, M., et al., *Electrochemical carbon nanotube field-effect transistor.* Applied Physics Letters, 2001. **78**(9): p. 1291-1293.
22. Bard, A. and L. Faulkner, *Electrochemical Methods*. 2001: John Wiley & Sons.
23. Hooge, F.N., *1/F NOISE SOURCES.* Ieee Transactions on Electron Devices, 1994. **41**(11): p. 1926-1935.
24. Mannik, J., et al., *Charge noise in liquid-gated single-wall carbon nanotube transistors.* Nano Letters, 2008. **8**: p. 685-688.
25. Stein, D., M. Kruithof, and C. Dekker, *Surface-charge-governed ion transport in nanofluidic channels.* Physical Review Letters, 2004. **93**(3).
26. Minot, E.D., et al., *Carbon nanotube biosensors: The critical role of the reference electrode.* Applied Physics Letters, 2007. **91**.
27. Instruments, D. *Applying the Model 1211 Current Preamplifier to Tunneling Microscopy* 1987; Available from: http://www.dlinstruments.com/technotes/technotes.html.

CHAPTER 7

FABRICATION OF NANOFLUIDIC CHANNEL WITH INTEGRATED CARBON NANOTUBE DEVICE

7.1 Chapter Introduction

The “nanochannel with integrated nanotube” device described in Chapter 6 of this thesis is fabricated using a novel process. The fabrication method is comprised of a combination of standard micro-electro-mechanical (MEMS) processing techniques, available in the Cornell Nanoscale Facility (CNF), as well as carbon nanotube growth techniques available in the lab of Professor Paul McEuen in the Cornell University physics department.

While the concept of the device operation is described in Chapter 6, in this chapter we focus on the fabrication method. We begin by reviewing a list of device requirements. We then give a broad overview of the fabrication process flow that was designed to meet these requirements. This is followed by a more in depth explanation of each step. Finally select portions of the process are expanded upon, in order to show characterization of the device at specific points in the fabrication process. In Appendix B is a detailed version of the full fabrication recipe, written with the intent that a person replicating the process for the first time would use it as a guide.

7.2 Device Requirements and Resulting Process Restrictions

Based on the concepts for electrical detection of charged DNA molecules in nanochannels using integrated carbon nanotubes, outlined in Chapter 6, we expect that a functional device will need to meet the following requirements:

1) *Nanochannel depths must be on the order of the Debye screening length.* For reasonably low ionic strength solutions, this screening length can be made as large as order $10nm$.
2) Nanochannels must be connected to microchannels in such a way that it is possible to load DNA molecules into the channels and individually flow them over the integrated carbon nanotubes in a controllable way. Based on the experience of this author, that necessitates simultaneous optical observation of fluorescently labeled DNA molecules in the channels. *Thus a fused silica substrate wafer with thickness of 170 μm is required.*
3) For the device to operate as intended, there must exist addressable semiconducting nanotubes which behave as electrolyte gated field effect transistors. For the nanotubes to respond to small perturbations in solution potential, it is believed that *integrated carbon nanotubes must be in direct contact with the electrolyte solution in the channel.*

Having established the essential device requirements, we can immediately describe several restrictions which these requirements place on the fabrication process.

1) The standard Craighead group process for fabrication of nanoslits and nanochannels in fused silica cannot be employed. This process involves fusion bonding and high temperature annealing of two fused silica wafers to enclose the channels. Fusion bonding requires that wafer surfaces are flat and clean (i.e. no bumps from electrodes or soot from nanotube growth). Typically, in order to sufficiently clean the surfaces, a wet chemical clean is used and this is followed by a high power oxygen plasma. After the oxygen plasma and touch bounding steps are performed an overnight anneal in air at $1050^{o}C$ is used.

Carbon nanotubes can survive neither oxygen plasma processes or a bake in atmosphere (specifically oxygen) at temperatures higher than $\sim 300^{o}C$.

2) In order to reliably drive molecules into the nanochannel detection regions, a network of loading channels must connect the detection region with a macroscopic fluidic reservoir. These channels must be leak free, and channel walls must be insulating. If photolithography is used, then the minimum aspect ratios required for channels with $10nm$ depths necessitate that the channel wall and ceiling structures must be relatively stiff to avoid collapse. This, and the desire for leak free channels, discourages the use of PDMS as a channel structure, for example.
3) It is anticipated that actual electrical detection will be challenging at first. The signal to noise ratio of the nanotube response to nearby DNA molecules will likely be low, perhaps even below unity. It is important then, that DNA molecules can be precisely positioned above the nanotubes and held in place for an extended period of time. This requires good visualization of the DNA molecules, in practice requiring that high numerical aperture objective lenses be used. It is therefore beneficial to fabricate devices on $170\mu m$ thick fused silica substrates. This permits the use of a 100 X , 1.35 N.A., oil immersion lens, which is known to be adequate for visualizing single DNA molecules. A further requirement of single molecule fluorescent microscopy is that the channel materials exhibit low autofluorescence.
4) Finally, in order for nanotubes to be placed inside of the channel, growth must occur before a number of other processing steps are performed. Growth of small diameter single wall carbon nanotubes typically requires the use of a catalyst such as Fe, or Co. Some thin film processing machines have sample restrictions. For example, samples with metals are banned from MOS

furnaces. Such restrictions were necessary to consider during development of the fabrication method.

7.3 Nanochannel/Nanotube -Device Fabrication Process Overview

While several variations of the fabrication process exist, we currently describe only the final version. This version has been selected to optimize the yield and throughput of devices while meeting the basic requirements outlined above. While it is not necessary for the yield and throughput to meet the level of "high volume manufacturing" , a phrase commonly used to describe industrial production levels, it is necessary to produce enough working devices that the experimental concept can be thoroughly tested. Even a fully fabricated device with working nanotubes may easily be damaged during the experimental runs. That damage may take the form of electrolytic destruction of nanotubes contacting solution, or clogging of nanochannels, for example. By using the following process, a researcher is able to fabricate roughly $10 - 20$ working devices within several weeks.

7.3.1 Precise Definition of a "Device", and its Geometry

In this chapter the word "device" refers to a continuous system of microfluidic and nanofluidic channels, connected to macroscopic fluidic reservoirs and to a number of detection regions, at which nanotube sensors are located. The prescribed fabrication method produces one device per chip, where each chip is a $20mm$ X $20mm$ piece of fused silica with various features constructed on one side. Each device contains 19 parallel nanochannel branches with a total of 38 separately addressable source/drain electrode pairs for contact with the imbedded carbon nanotubes. Diagrams of such a device are shown in Figure 1.

Figure 1. Device diagrams. For ease of viewing, not all features within each image are drawn to scale relative to one another. When necessary, critical dimensions are indicated by red arrows and labels. **A)** View of full fluidic network. Blue circles represent the six macroscopic reservoirs for loading fluid and DNA. Thick black lines represent fluidic channels used for transporting DNA into the device from the reserviors. These channels are $40\mu m$ wide, $100nm$ deep, and several mm long. Support columns (not shown) in the middle of the loading channels help to prevent the ceiling structure from collapsing. The left and right loading channels are connected by 19 smaller microchannel branches, which are $6\mu m$ wide and $100nm$ deep. **B)** Close-up of region where 3 microchannel branches connect to the larger loading channel. This correspond to the large red rectangle in 1A. **C)** Close up on middle portion of a microchannel branch. This corresponds to the small red rectangle in 1A. As is drawn, two detection regions are present in each microchannel branch. **D)** Close-up of a detection region. Two platinum electrodes (a source and drain) are separation by a gap of $1\mu m$. The $6\mu m$ microchannel branch tapers into a $500nm$ nanochannel in order to thread the gap between the source and drain electrodes. An unspecified number of carbon nanotubes bridges the gap between electrodes. A portion of each nanotube exists in the nanochannel and is in direct contact with the fluid.

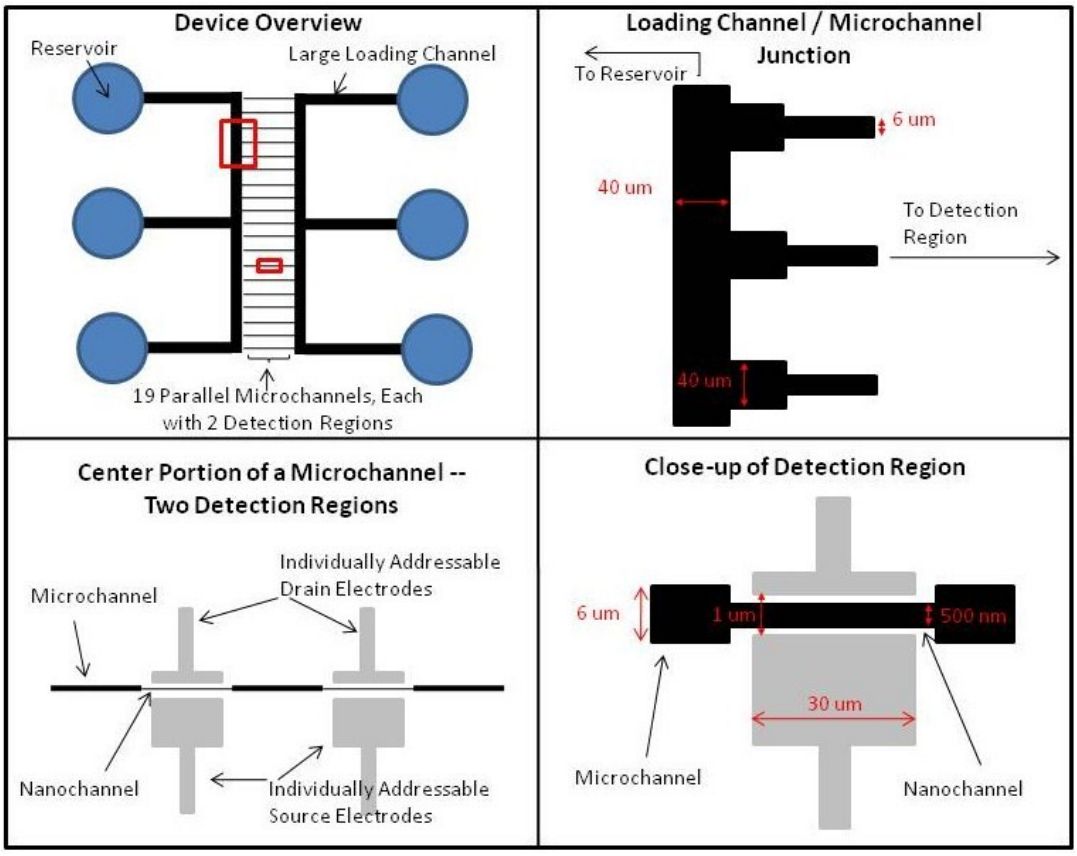
Device Overview
Reservoir
Large Loading Channel
19 Parallel Microchannels, Each with 2 Detection Regions
Loading Channel / Microchannel Junction
To Reservoir
6 um
40 um
To Detection Region
40 um
Center Portion of a Microchannel -- Two Detection Regions
Individually Addressable Drain Electrodes
Microchannel
Nanochannel
Individually Addressable Source Electrodes
Close-up of Detection Region
6 um
1 um
500 nm
30 um
Microchannel
Nanochannel

7.3.2 Major Fabrication Steps

The fabrication process can be broken down into 14 major steps and those are organized into 3 phases:

I. Cleanroom Processing on Full Wafers (Major Steps 1-3, shown below)

II. Carbon Nanotube Growth on Chips Diced from Full Wafers (Major Step 5 shown below)

III. Clean Room Processing on Chips (Major Steps 6-13, shown below)

Beginning with a $170\mu m$ fused silica wafer, the 14 major fabrication steps are:

1) Alignment Layer
2) Pt/Ti Electrode Layer
3) Aluminum Oxide Supported Cobalt Catalyst Layer
4) Wafer Dicing
5) Carbon Nanotube Growth
6) Thin Silicon Nitride Layer
7) Microchannel/Nanochannel Sacrificial Chromium Layer
8) Thick Silicon Nitride Layer
9) Access Hole Layer #1 (For Wet Etch of Sacrificial Material)
10) Wet Etch of Sacrificial Material
11) Wet Etch of Thin Silicon Nitride Layer
12) Thin Silicon Nitride Layer #2 (For Enclosing Access Holes)
13) Access Hole Layer #2 (For allowing access of probe needles to source and drain contact pads)
14) Macroscopic Reservoir Attachment

In the panels of Figure 2, a diagram is used to illustrate only 9 of the 14 major steps, though below we make a few remarks about each of the 14 major steps.

Figure 2. A select number of the 14 major steps. Only those steps which lend themselves to illustration are shown here. Each cross sectional image is labeled with its corresponding step number and name. **Step 1)** Alignment marks (not actually shown) are etched into a 4 inch, $170\mu m$ thick, fused silica wafer. **Step 2)** Pt contact pads are deposited onto the wafer. **Step 3)** Cobalt catalyst pads are deposited onto the wafer using photolithography, ebeam evaporation, and liftoff. **Step 5)** After dicing (illustration not shown) chips are placed into nanotube furnace for CNT growth. **Step 6)** A $5-20nm$ thin layer of silicon nitride is deposited on the wafer, covering the fused silica, Pt contact pads and nanotubes. **Step 7)** A 10 nm thick, patterned layer of chromium is placed onto the wafer using pholithography, ebeam evaporation and liftoff. **Step 8)** A $2\mu m$ thick layer of low stress silicon nitride is deposited directly onto the nanotubes. **Step 10)** After access holes are defined along the length of the microchannels (illustration not shown) the chromium sacrificial layer is selectively etched away using a CR-14 Chromium etchant (Cyantek). **Step 11)** Wet etch of protective nitride layer, within which the nanotubes are buried. The etch height is controlled with a timed etch of heated MF-312 (5% TMAH, Microposit Corp.). The wet etch is followed by drying the channels, covering access holes with nitride, re-etching contact pad access, and installing macroscopic fluidic reservoirs, none of which is illustrated above.

1. Fused Silica Wafer with Alignment Marks

2. Platinum Electrode Deposition

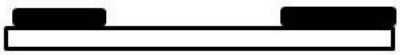

3. Co Catalyst Deposition

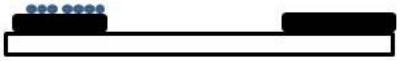

5. Carbon Nanotube Growth

6. Protective Nitride Layer

7. Cr Sacrificial Layer Deposition

8. Thick Nitride Capping Layer

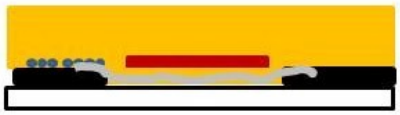

10. Wet Etch of Cr Sacrificial Layer

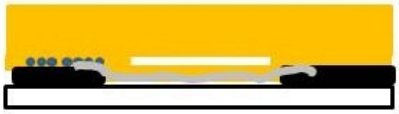

11. Wet Etch of Protective Nitride

Step 1, Alignment Layer. Fused silica wafers are initially featureless, and marks must be made on the wafer which allow for alignment of each of the subsequent lithography layers. Two types of alignment marks are employed in this process, which is designed for the GCA Autostep Aligner in the CNF. Global GCA marks are used to perform a course alignment by eye. micro-DFAS (Dark Field Alignment System) marks are then used to perform a fine alignment.

Step 2, Pt/Ti Electrode Layer. Source and drain electrodes for contacting carbon nanotubes are defined using photolithography, e-beam evaporation and lift-off. The electrodes are composed of Pt (30nm thickness) and Ti (5 A thickness). The purpose of titanium is to promote adhesion between the Pt metal and the fused silica wafer.

Step 3, Aluminum Oxide Supported Cobalt Catalyst Layer. Catalyst pads, for promoting nanotube growth, are defined using photolithography, e-beam evaporation and lift-off. The evaporated materials are Ti (5 A), Al2O3 (15 nm), Co (2.5 A). Titanium is used to promote adhesion between aluminum dioxide and fused silica. Aluminum dioxide is used for two purposes. First it has previously been shown that catalyst deposited on aluminum oxide surfaces yield better growth than catalyst deposited on silicon dioxide. At least 10 nm is required so that a continuous film is achieved. Second, the thickness of the aluminum dioxide raises the position of the Co particles with respect to the Pt contact pad. It is surmised that this may increase the likeliness for a carbon nanotube to make it over the Pt during the growth stage. Thus far this affect has not been quantified.

Step 4, Wafer Dicing. Prior to carbon nanotube growth, the 4 inch (100 mm) device wafers are diced into 16 chips (20mm x 20mm) using a wafer saw. Each of the chips

contains one of the “devices” described in Section 7.2. This dicing step is required in order that the chips are able to fit in the carbon nanotube furnace. The fused silica furnace tube inner diameter is roughly 22 mm. It is known that the wafer dicing process can cause damage to MEMs type structures. During development of the fabrication procedure, it was discovered that damage was being caused to areas of the fused silica between the source and drain electrodes. This problem was solved with the use of a thick resist coating to protect features from debris during dicing and changes to the device geometry, the length of the platinum wires was shorted, presumably reducing stress induced by the platinum.

Step 5, Carbon Nanotube Growth. Single walled carbon nanotubes are grown with a Chemical Vapor Deposition technique using the carbon nanotube furnace in the Paul McEuen lab. One of two growth recipes is used depending on the desired yield of nanotubes. A recipe which includes Ethylene as a carbon precursor, and which is run at 800C results in a moderate yield of carbon nanotubes. A recipe which includes both Ethylene and Methane as carbon precursors and which is run at 900C results in a higher yield of carbon nanotubes. Nanotube growth is initiated only at the location of the Co catalyst particles. The resulting direction and length of each nanotube is random, and the probability that a certain number of tubes connects source and drain electrodes is given by Poisson statistics.

Step 6, Thin Silicon Nitride Layer. After the nanotubes are grown, a thin layer of silicon nitride is conformally deposited on top of it using a Plasma Enhanced Chemical Vapor Deposition (PECVD) process. This layer should be on the order of 10nm in thickness. The function of the thin nitride layer is to protect the carbon nanotubes from wet chromium etchant during Step 10. It is believed that the strong

oxiding agent (cerric ammonium nitrate) in Cr-14 Chromium Etchant damages carbon nanotubes if it directly contants them for an extended period of time. Thus during the chrome etch, nanotubes are separated from the channel by the thin nitride layer. That thin layer is later removed (Step 12) using an etchant that does not damage carbon nanotubes. It also appears that covered nanotubes with nitride provides for some protection from the possibility of static charge induced damage during the remaining fabrication steps. Because nitride is deposited directly onto bare nanotubes, the deposition parameters also must be carefully chosen so as not to damage the tubes. To begin with, PECVD silicon nitride was selected instead of PECVD silicon oxide, due to the well known observation that nanotubes are quickly etched in an RF oxygen plasma. During the course of process development it was observed that low frequency RF plasma in direct contact with bare nanotubes, induces damage to the tubes (in the form of reduced conductance). We surmise that this is a result of physical ion bombardment. In order to protect the nanotubes from low frequency nitride deposion, a short high frequency nitride deposition is first performed. This covers the nanotubes and protects them from physical ion bombardment. This topic is described in more detail in section 7.4.5.

Step 7, Microchannel/Nanochannel Sacrificial Chromium Layer. Using photolithography, e-beam evaporation and lift-off, a layer of chromium is deposited on the wafer. The chromium pattern defines the shape and thickness of the desired micro-channels and nanochannels. The final channel height can be no less than the thickness of the chromium sacrificial layer (although it may be more depending on the wet etch Step 11). Chromium was chosen as the sacrificial material due to the high

selectivity between the wet etch rates of chromium versus silicon nitride and fused silica in CR-14 Chrome Etchant.

Step 8, Thick Silicon Nitride Layer. After Cr deposition, the sacrificial material and the carbon nanotubes are covered by a thick layer ($\sim 2\mu m$) of low stress nitride. This nitride layer later becomes the "ceiling" of the nanofluidic device. As such, its mechanical properties are critical for maintaining structural integrity of the channel. A nitride film with low tensile stress and thickness of $\sim 2\mu m$ was chosen in order to prevent cracking or collapse of the nitride after sacrificial layer removal. Films with higher tensile stress were found to crack, and thinner films were found to collapse. Films with compressive stress properties were found to bow. Testing and characterization of these effects is shown in Section 7.4.3

Step 9, Access Hole Layer #1 (For Wet Etch of Sacrificial Material). Access holes through the thick silicon nitride layer are created using a combination of photolithography and dry chemical etching. The access holes run along the length of the microchannel and nanochannel regions. During this step, in addition to the access holes for wet chemical etching, holes above the contact pads are created, enabling access of probe needles to the source and drain contact pads.

Step 10, Wet Etch of Sacrificial Material. The sacrificial chromium layer is removed using Cyantek CR-14 Chromium Etchant. With access holes spaced approximately $50\mu m$ apart along the length of the channel, and a lateral etch rate of $10\mu m/hr.$, all of the chromium can be remove in about 3 hours. Generally the etch is allowed to run roughly double of this time (5-6 hours). Evidence suggests that in Cr-

14 etchant, the selectivity between chromium and silicon nitride is very high, as is the selectivity between chromium and fused silica.

Step 11, Wet Etch of Thin Silicon Nitride Layer. After removal of the chromium layer, a system of channels has been created with a depth equal to that of the original chromium layer. This allows for quick delivery of the next wet etchant (MIF 312). Trimethylammonium hydroxide (TMAH) is present at 5% of total volume in MIF 312. When heated, TMAH etches low stress GSI PECVD silicon nitride at a rate of about $2nm/\min$. This allows for upwards etching of the silicon nitride, to the point at which carbon nanotubes are released from within the nitride ceiling. The chip is submerged in MIF 312 at $70^{\circ}C$ for anywhere from 15 min to 45 min, depending on the thickness of the previously deposited protective nitride layer.

Step 12, Thin Silicon Nitride Layer #2 (For Enclosing Access Holes). After the second wet etch step, chips are dried and electrical conductance of nanotubes can be tested. The access holes used in the wet chemical etch must be sealed, in order for channels to be complete. Low stress silicon nitride is once again deposited using PECVD. The final silicon nitride film is of medium thickness (several hundred nm) to ensure that all of the access holes are completely sealed.

Step 13, Access Hole Layer #2 (For allowing access of probe needles to source and drain contact pads**).** Having deposited a final layer of silicon nitride, the contact pads must once again be uncovered. This is done using a combination of photolithography and reactive ion etching.

Step 14, Macroscopic Reservoir Attachment. In the chip's near final state, the contact pads are exposed, but the nanochannels and microchannels are completely sealed. Entrances at the six microchannel ends are created by lightly scratching the nitride with a diamond scribe. Macroscopic reservoirs are then aligned to the channel entrances by eye and glued to the chip using RTV sealant. After the glue sets, the devices are ready to be filled and used in DNA experiments.

7.4 In-Depth Characterization of Select Processes in Fabrication Procedure

7.4.1 Etch Characterization

Wet Etch Rates

In order to describe the characteristics of the chromium sacrificial layer removal step, we first describe etching of another material layer that had been tested as a candidate for the sacrificial layer before chromium was settled on. Namely, that material is amorphous silicon. According to reports in the literature, there exists excellent selectivity for amorphous silicon and silicon nitride in TMAH. For a-Si and LPCVD nitride, selectivities as high as 20000:1 have been reported in 5% TMAH. This combination of materials was therefore a good candidate for our sacrificial process. After testing the etch rates of a-Si and GSI PECVD nitride, it was found that the selectivities were much lower than expected. Namely, they were on the order of 50:1. A compilation of measured etch rates and values found in the literature can be found in Table 1.

Table 7.1 Etch rates for a variety of possible wall and sacrificial materials in Cr-14 and MF-312 etchants. For each etchant and material there is either a value for etch rate found in the literature, or measured by the author of this thesis, or both. The measured selectivity between chromium and silicon nitride is infinite within error. The measured selectivity between amorphous silicon and silicon nitride in 5% TMAH is between 48:1 and 62:1, depending on whether a high stress or low stress recipe was used for the nitride. This differs from the value reported in the literature of 20000:1 for amorphous silicon and high stress nitride. The discrepancy is attributed to the fact that the high stress nitride investigated in the literature is LPCVD deposited nitride, while that investigated by ourselves is PECVD deposited nitride.

	Cr-14 @ 25C		***MF-312 (5% TMAH) @ 70C***	
	Literature	***Measured***	***Literature***	***Measured***
Silicon	***0.0 nm/min***	***0.0 nm/min***	***100 nm/min***	***100 nm/min***
Silicon Nitride (High Stress)	*--*	***0.0 nm/min***	***0.005 nm/min***	***1.6 nm/min***
Silicon Nitride (Low Stress)	*--*	***0.0 nm/min***	*--*	***2.1 nm/min***
Silicon Dioxide	***0.0 nm/min***	***0.0 nm/min***	***0.02 nm/min***	***0.5 nm/min***
Chromium	***93 nm/min***	***23 nm/min***	*--*	*--*
Fused Silica	***0.0 nm/min***	*--*	*--*	*--*

The poor selectivity of a-Si and GSI PECVD nitride resulted in channels which were tapered and much deeper near the access hole entrances. This concept is illustrated in figure 3, and optical images of the channels after the wet etch step are shown in figure 4. Chromium wet etch selectivities were later measured as well. During various stages of the etch, the distance between the nanochannel entrance and the chrome in a

partially etched channel could be measured by optical microscopy. Examples of such images are shown in figure 5. The observed rate is approximately $10 \mu m / hr$ or $27 nm / \min$. Within the error of our measurement, there is infinite selectivity between chromium and silicon nitride in Cr-14 etchant.

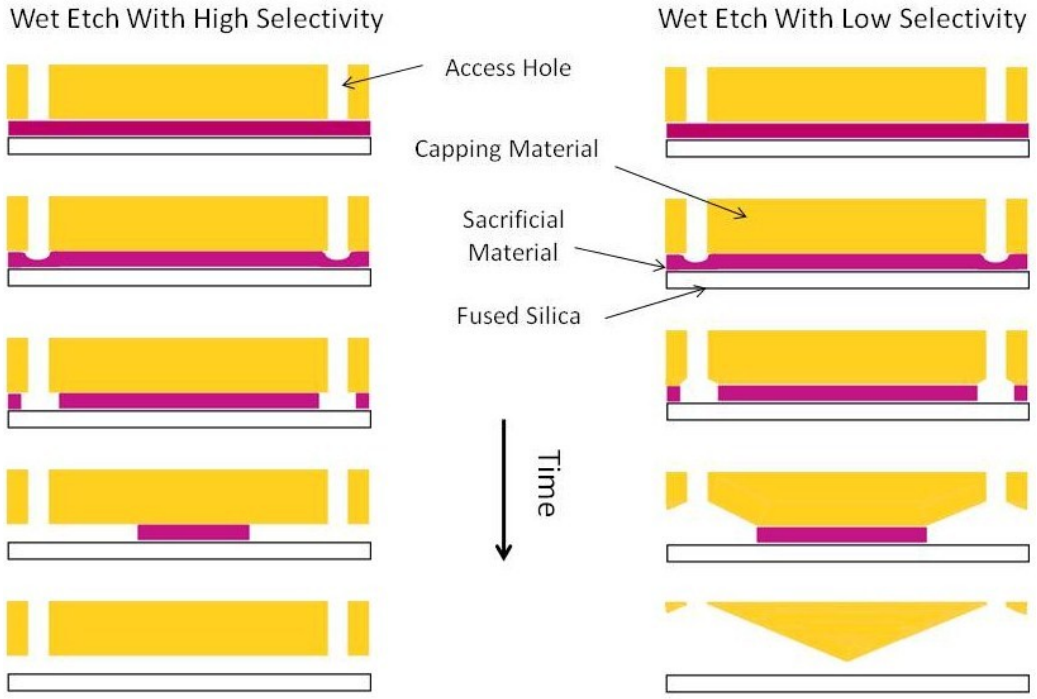

Figure 3. Cartoon illustrating the importance of selectivity in sacrificial Layer removal. Left Column) Channel depth is determined by sacrificial layer thickness only. Right Column) Channel depth is determined by sacrificial layer thickness plus amount of capping material etched.

Dry Etch Rates

Using a combination of reactive ion etching, profilometry, and interferometry, dry etch rates were measured for silicon nitride. Low Stress Nitride in CHF3/O2, Oxford 80#1 Nitride Recipe: 98 nm/min.

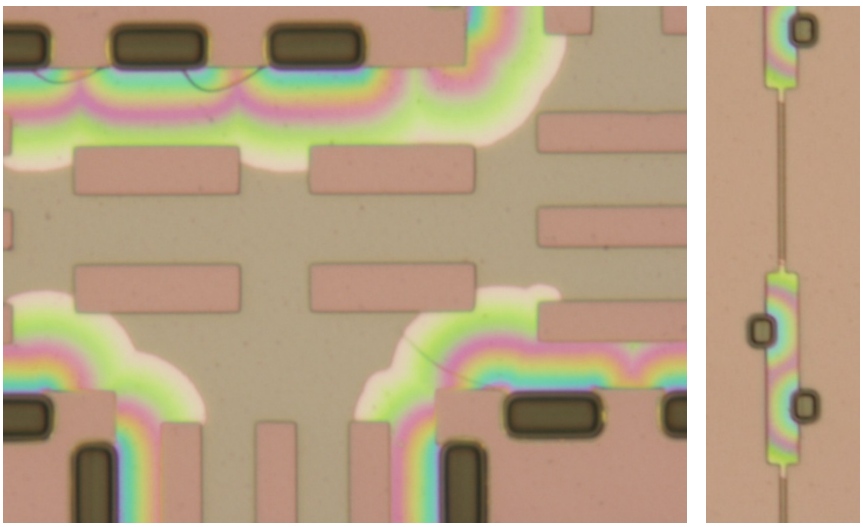

Figure 4. Images of a-Si/ Nitride based channels after partial removal of a-Si with TMAH etch. Access holes are the dark rectangles. The light gray areas are places where the a-Si sacrificial layer has not yet been etched away. The gaps between the fused silica surface, and nitride ceiling vary in depth due to upward etching of the nitride as the a-Si was etched inward.

7.4.2 Nitride Deposition

Silicon nitride films deposited by PECVD at temperatures lower than 400C are typically observed to be amorphous, and their structural, electrical and optical properties are strongly dependent on deposition parameters [1, 2]. Our device requirements necessitate a nitride film that has low autofluorescence, is electrically insulating, and is structurally stable in the form of a nanochannel ceiling and wall. In testing various nitride deposition parameters, we have observed that the first two conditions are met to satisfaction over the entire range of parameters tested. It is the mechanical properties of the film which can vary by the greatest amount. And, it turns

out that only a narrow range of deposition parameters result in a film with satisfactory mechanical properties.

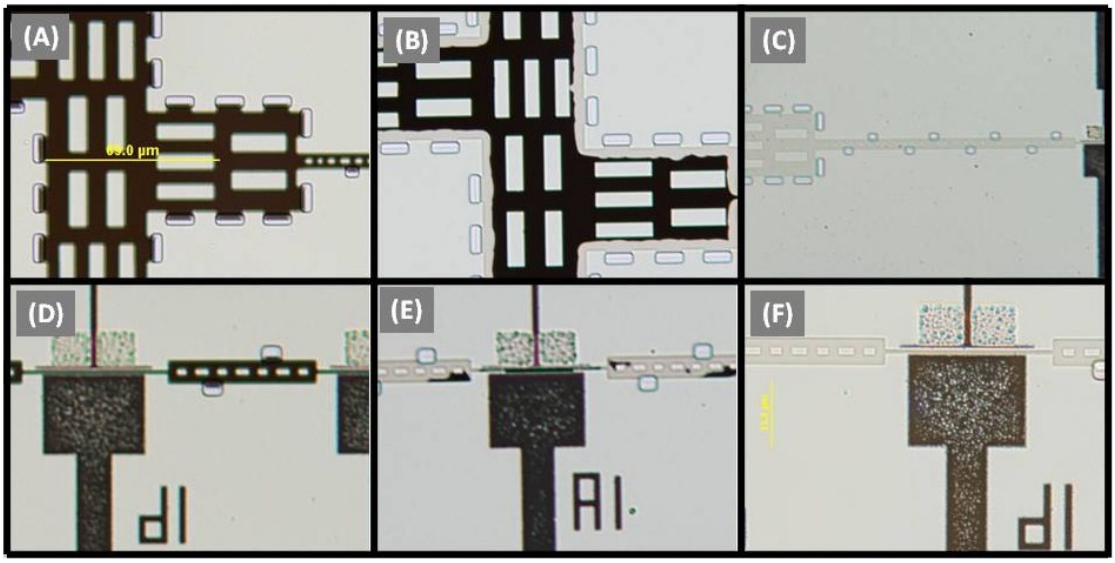

Figure 5. Images of Cr/Nitride based channels after partial removal of Cr with Cr-14 Chromium Etchant. **A-C)** Images of microchannel region before etch, after 25 min, and after 3 hours. **D-F**) Close up of nanochannel region before etch, after 25 min, and after 3 hours. Note that because all portions of the etched channel are the same depth, there are not regions of etched channel with different colors as is the case with the channels of figure 4.

For reasons which are discussed in detail later in this section, it is necessary that the deposited film be one of low tensile stress. Several deposition parameters are known to effect the residual stress of the material including deposition temperature [3, 4], ratio of precursor gases leading to variations in stoichiometric content [5], and the frequency or combination of frequencies used to generate the plasma during deposition [5, 6].

While deposition temperature can be used in part to tune stress, and is typically a free parameter in nitride deposition processes, we find that we are restricted to a deposition temperature of 300 C only. CNTs are already present on the chips before nitride deposition, and if the wafers were heated to temperatures much higher than 300C during loading into the PECVD machine, oxygen in the chamber may cause the CNTs to burn. Furthermore, it has been reported that increasing deposition temperature causes an increases residual tensile stress. As will be shown later in this section, we go to lengths to decrease the tensile stress as compared the nominal stress value for films deposited using standard CNF recipes. We do not use temperatures below 300 C because it has been reported that as deposition temperature is reduced toward 200 C the observed film quality becomes poor [3]. Namely, film porosity increases.

Having established 300 C as our optimal deposition temperature, we choose to vary the frequency characteristics of the plasma in order to tune film stress. As reported by Pearce et al. [5], the use of two radio frequency generators, one at 13.56 MHz and one at several hundred kHz, can be used to vary intrinsic film stress by altering the amount of power supplied by each source. It was observed that the low frequency excitation favors the formation of N-H bonds, and the relative amount of N-H bonds and Si-H bonds were shown to affect stress. As the percentage of low frequency power used was increased from 50% to 70%, the film stress changed smoothly from 50 MPa tensile to 150 MPa compressive. Even greater ranges of low frequency powers and the resulting film stresses have been reported elsewhere.

The GSI PECVD machine available in the CNF has two radio frequency sources, one at 13.56 MHz, and another at 300kHz, with maximum output powers of 1000W and 200W respectively. A comprehensive study is underway by the tool manager Phil

Infante in which the effect of the percentage of low frequency power on stress of nitride films deposited on silicon wafers at 400 C is being investigated. His results are thus far in accordance with what has been found in the literature. These results are available in the GSI manual or upon request, though we do not reprint them here as absolute stress values have been known to change dramatically if certain changes are made to the tool. Nevertheless, in all cases the trend of decreasing tensile stress and increasing compressive stress with increasing low frequency power has been observed.

The nitride steps in our fabrication process differ from what has been investigated by the tool manager in two ways. First, we use a deposition parameter of 300 C as opposed to 400 C. Second, we use a fused silica substrate as opposed to a silicon substrate. The way in which these differences affect film stress is through a mismatch in thermal expansion characteristics. While low temperature deposition reduces the effects of mismatch. The reported coefficients of linear thermal expansion for silicon , fused silica, and silicon nitride at 327 C are 3.7, 0.5, and 2.8 $10^{-6} K^{-1}$ respectively. A temperature transition from 300 C to 20 C results in a compression of 14%, 9.3% and 2.4 % for each of the three materials on their own [7]. For stacked materials, we assume that the substrate wafer dominates the thermal compression process and the thin film is forced to comply.

When a thin film of silicon nitride deposited on a silicon wafer at 300 C cools to room temperature, it is forced to compress to14% of its original length in one dimension. This is greater than the 9.3% linear compression it would experience if it were not fixed to the silicon surface. This thermal contraction mismatch causes the film to have a higher compressive stress than it would have had on its own.

For a thin film of silicon nitride deposited on a fused silica wafer, the effect is reversed. The fused silica substrate wafer compresses by only 2.4% in one direction, while the nitride, on its own, would have compressed by 9.3% upon cooling. Because the nitride is not permitted to fully relax, the film has a higher tensile stress than it would have if it were not fixed to the fused silica.

Thus the effect of cooling from 300 C to 25 C has the opposite effect on stress for thin nitride films deposited on silicon as compared to films deposited on fused silica. It is for this reason that the Phil Infante recipes yield higher tensile stress films than expected, when the substrate is fused silica.

We now consider the effect of various types of stress on our micro- and nanochannel ceilings. The channel ceilings are modeled as doubly clamped beams. The channel length is much greater than the channel width and depth in all cases, therefore the dimension along the direction of the channel axis can be ignored, and we consider only the cross section. Depending on the stress of the nitride film, the beam experiences forces that may cause it to deform in a number of different ways. For example, high compressive stress can lead to buckling in either the up or down vertical directions, as is illustrated in figures 6A and 7A. At the opposite extreme, a high tensile stress film inevitable leads to cracking of the ceiling at many points along the channel (not shown in the figure). A low tensile stress film represents the ideal case, but if the stress is too small in magnitude, the beam cannot resist deforming under the load of dispersion forces and/or the capillary forces acting on the walls during any number of fabrication steps in which the channel must be dried.

In order to find the appropriate stress, we investigated the regime of high to low tensile stress. Our goal was to find a condition under which both cracking and collapse is avoided. Under a uniform load, such as is induced by dispersion forces between a ceiling and a floor, the beam experiences a maximum downward deflection, z, given by,

$$z = \frac{L^3 \cdot \lambda}{E \cdot h^3}$$

where L is the length of the beam (in our case the width of the nanochannel), λ is the the load, E is the Young's modulous (which is a function of the stress), and h is the height of the thin film (beam thickness). Using this equation as a guide, we see that the maximum deflection is more strongly dependent on the film thickness and length of channel spanned, than it is on the stress. These are two additional parameters worth varying in order to create channel ceiling which do not crack under their own stress, yet also do not collapse.

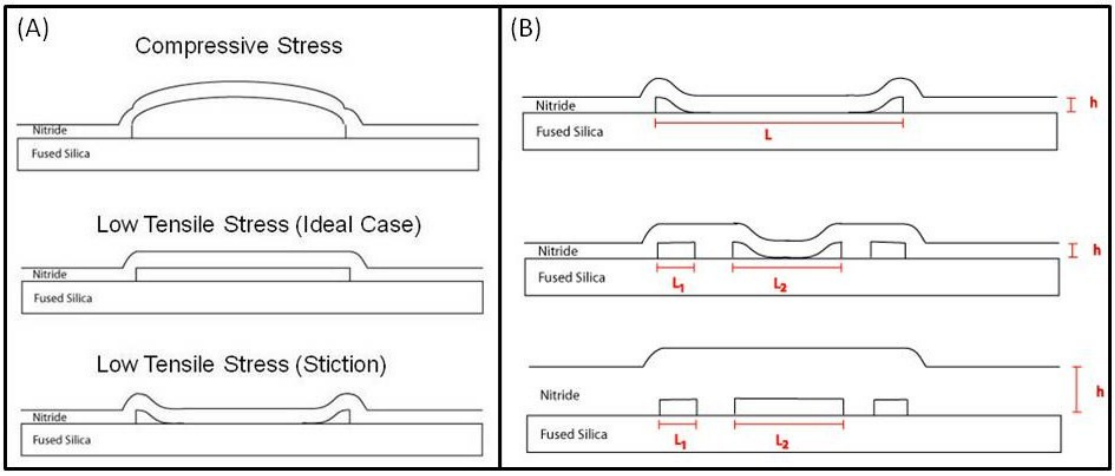

Figure 6. Deformation of channel ceiling structure. **A)** Affect of stress on deformation. **B)** Affect of nitride thickness and width of channel spanned on deformation under a uniform load.

In figure 6B, and figures 7B and 7C, we demonstrate the effects of beam length (channel width) and thickness on probability of collapse given a constant internal stress. Previous to these tests, we first determined the deposition parameters that would result in a low enough tensile stress such that cracking did not occur. Images of cracked channel ceilings and other parts of the nitride film are not shown in this chapter but are available upon request. In the image of figure 7B and the images of 7C the same combination of frequencies is used during deposition.

The deposition parameters that are currently suggested are as follows: high frequency power 19% (190W), low frequency power 81% (162W), deposition duration 20 min (=2 um thick film), maximum channel width 16 um. This results in a negligibly small probability of cracking or collapsing for channels created with a sacrificial Cr layer as thin as 10nm in thickness. A sub 10nm Cr layer has not yet been tested. It should be

Figure 7. Various micrographs illustrating the effects of film stress, thickness and channel width on channel integrity. **A)** A 40 um wide channel with no support columns. The film was deposited using a pure low frequency deposition process with the IPE CVD machine, and is under a high degree of compressive stress. As a result after removal of the Cr, the ceiling buckles both upwards and downwards. The left hand micrograph is an optical image in which variation in color and intensity results from variations in cavity height. The right hand image is an SEM micrograph of the same channel. The black line over the left image represents the location of a profilometry scan in which the maximum vertical deflection of the ceiling was found to be 2 um. **B)** The effect of channel width on collapse probability can be seen by looking at a single image of a channel with various amounts of space between the walls and the support columns. The green areas represent an air gap between the floor and ceiling of 25nm. The tan areas represent nitride in direct contact with the fused silica substrate below it. The bright red area represents Cr (25 nm thick) which had not yet been removed before the wet etch was stopped. **C)** The three channels shown illustrate the effect of nitride thickness on probability of collapse. It is clear that the evenly colored channel for the 1650nm thick film is the only one which did not collapse. Note that in all cases, profile scans were used to verify the notion that certain portions of the ceiling had or had not collapsed.

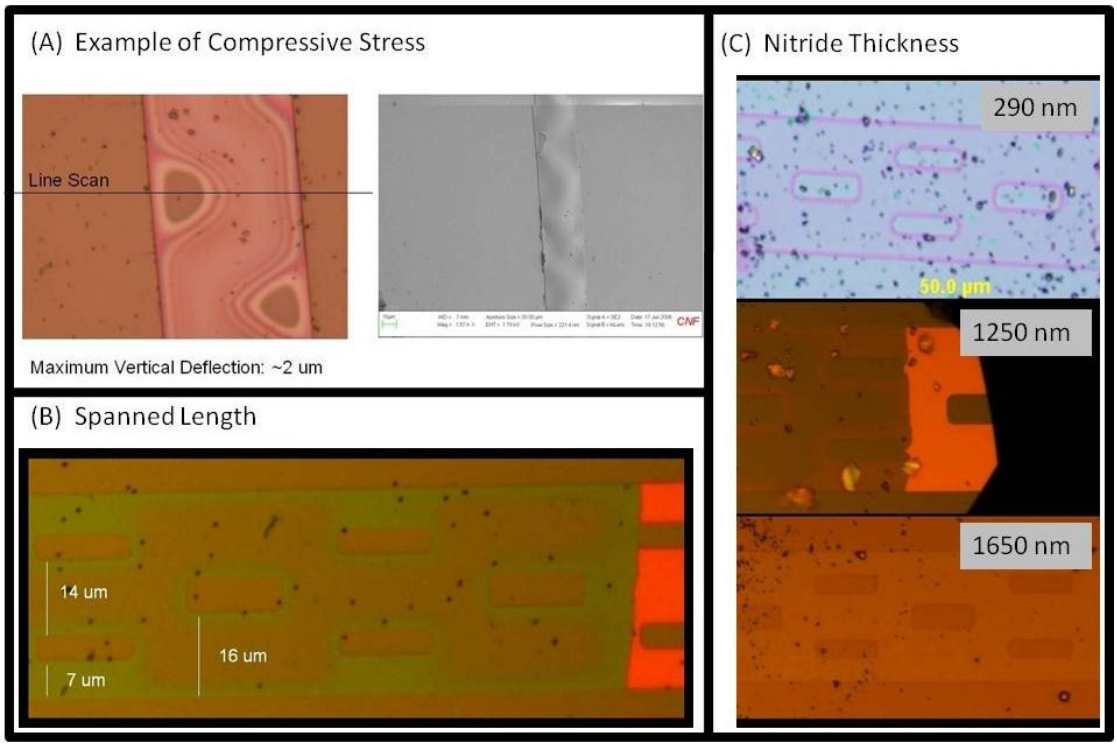
(A) Example of Compressive Stress
Line Scan
Maximum Vertical Deflection: ~2 um
(B) Spanned Length
14 um
16 um
7 um
(C) Nitride Thickness
290 nm
50.0 µm
1250 nm
1650 nm

noted that for nitride films with thickness of less than 1000nm, no degree of stress could be found which prevented both channel collapse and film cracking.

7.4.3 Notes on CNT Growth

Catalyst Deposition Cobalt catalyst particles are deposited in photolithographically defined areas, as described in section 7.3. Cobalt was eventually chosen over iron for the catalyst due to processing restrictions in the GSI PECVD machine. However Fe catalyst was used in the initial stages of the project. Based on SEM images, the carbon nanotubes appear, on average, shorter and less dense when grown using Co catalyst than when grown using Fe catalysts. This is an impression only, as no statistical analysis was performed. Several thousand SEM images were taken over the course of this project. From observation of those images, it is clear that both Co and Fe catalyst growths result in a sufficient density of nanotubes with lengths greater the several microns.

For the two different catalysts, the distribution of CNT diameters may also be different. An article by the Dai group suggests that a 0.5A thick cobalt catalyst film and 750 C ethylene growth provide for tubes predominantly in the 1.0 to 1.8 nm range [8]. While we did take some AFM images of grown tubes, we did not take a large enough number of AFM images to enable us to make a statement regarding difference in tube diameters resulting from the two different catalysts tested.

It should be noted that, in the future, if a person wanted to use the GSI PECVD for a chip which has a small amount of iron on it, it may be possible to persuade the tool

manager Phil Infante to allow this. His official policy is that no Fe is permitted, however he appears to be on the fence about this.

Nanotube Device Yield

Using the current device design and procedure, it has been observed that anywhere from 0 to 10 nanotubes bridge each source and drain electrodes. It is expected that the actual number of nanotubes per electrode pair is random and is governed by Poisson statistics. The probability mass function for rare occurrence statistics is

$$f(k,\lambda) = \frac{\lambda^k \exp(-\lambda)}{k!}$$

where, in our case, f is the probability that a source drain electrode pair has k connecting them, if the mean number of nanotubes connecting the source drain pairs is λ. If, for example, the mean number of connecting nanotubes per electrode pair is $\lambda = 1$, then the probability that an given electrode pair has exactly $k = 1$ connected nanotubes is $f = e^{-1} \approx 0.36$, the probability that there are no connected nanotubes for a given electrode pair is also $f = e^{-1} \approx 0.36$, and the probability that there is more than one connected nanotube for a given electrode pair is also $f = e^{-1} \approx 0.38$. Recently, when running the ethylene growth process at 800C we found that only about 10% of the electrode pairs have no connecting nanotube, given our device geometry and catalyst particles. When running the same process at 750 C the percentage of electrode pairs showing no current above the noise was closer to 90%. Note that these growth runs were performed with chips from the same wafer (i.e. same catalyst processing) and within a three week period (so nanotube furnace temperature probably had not drifted much). In any case, temperature adjustment appears to offer some degree of control over nanotube yield in our process. Other factors which also affect the number of connect nanotubes per device are catalyst and source drain pad size,

source-drain separation distance, catalyst thickness, catalyst support (Al2O3 or fused silica), height of T-shaped Pt pad and height of Cr sacrificial layer, etc. These parameters and others have been adjusted at one time or another throughout the process development, and any of them could be explored in a more systematic way.

7.4.4 Notes on Photolithography

Micro DFAS Alignment Marks

In any multilayer photolithography based process, accurate inter layer alignment is critical. In our process, alignment is achieved through the use of a system specific to the Autostep machine called the micro Dark Field Alignment System (microDFAS). In order to utilize this system, a patterned layer of regularly spaced marks are etched directly into the wafer. These are then used to align the wafer with the Autostep reticle in each of the subsequent alignment and exposure steps. There are several patterns available, each of which can be recognized by the microDFAS system. In this section we show that choosing a pattern appropriate to our substrate and resist is crucial for good alignment. In figure 8 diagrams of three possible microDFAS patterns are shown, as is a bright field image of one of those patterns.

Dark field images of these marks appears quite different. In dark field microscopy, the edges of the etched features appear brightest, as can be seen by comparing figure 8D with figure 9A. It is the long edges of each rectangle which the microDFAS system uses when aligning a wafer. In figure 9A the edges of the rectangle appear very sharp, and one might guess that a good alignment is possible. Typically, if the substrate wafer is silicon, coating the features with a layer of photoresist will not affect the dark field alignment pattern. In our case, the substrate wafer is fused silica, which

has an index of refraction similar to that of photoresist. Thus when photoresist non-uniformly coats the etched rectangles, edges in the dark field image appear to be smoothed out instead of sharp. The apparent edge is blurred and shifted toward middle of each the rectangle. This results in a poor alignment mark signal and inconsistent alignment by the microDFAS system.

As an alternative to the "rectangle edge" pattern, a series of lines can be defined by etching small circles where the rectangle "edges" used to be. In this way, photoresist cannot severely distort the dark field image, as is apparent figures 9C and 9D. Employing this pattern results in much better alignment by the microDFAS system.

LOR Thickness and Minimum Feature Separation

Several of the "major steps" in the process require a combination of photolithography e-beam evaporation and lift-off. Commonly, in order to achieve a resist sidewall profile which allows for a clean metal lift-off, a technique known as image reversal is used. For several reasons we choose an alternative method of using a bi-layer resist, or more specifically, a lift-off resist (LOR) in combination with a standard photoresist layer. This method also produces sharp metal edge profiles, but does not require a lengthy image reversal step, and for certain patterns permits more straightforward mask design.

Several versions of LOR are available, each having a different viscosity and producing a different LOR film thickness when spun onto a wafer. For most metal lift off applications, it is recommended to LOR 5A or 10A which results in film thicknesses in the range of 400-600nm and 900-1100nm respectively. Typically LOR5A is the

Figure 8. Variations of the micro DFAS mark pattern available for use with the Autostep mask aligner. **A)** Snapshot of CAD image for "solid rectangle" micro DFAS mark in positive tone. Shaded areas are exposed in the photolith step and are etched into the substrate wafer. The width of each rectangle is 6 um and the half pitch is also 6 um. **B)** Snapshot of CAD image for "segmented line" microDFAS mark in positive tone. The small shaded squares composing each segmented line are separated by approximately 2um. The segmented lines are spaced by 6 um. **C)** Snapshot of CAD image for "solid rectangle" micro DFAS mark in negative tone. Shaded areas are exposed in the photolith step and are etched into the substrate wafer. Thus the rectangles are un-etched and are raised off the surface. The negative tone version of the "segmented line" pattern is also available but is not shown here. **D)** Bright field image of a micro DFAS mark etched into a fused silica wafer. This mark is the "solid rectangle" pattern shown in figure 9A, where the rectangles have been etched greater than 2 um into the wafer.

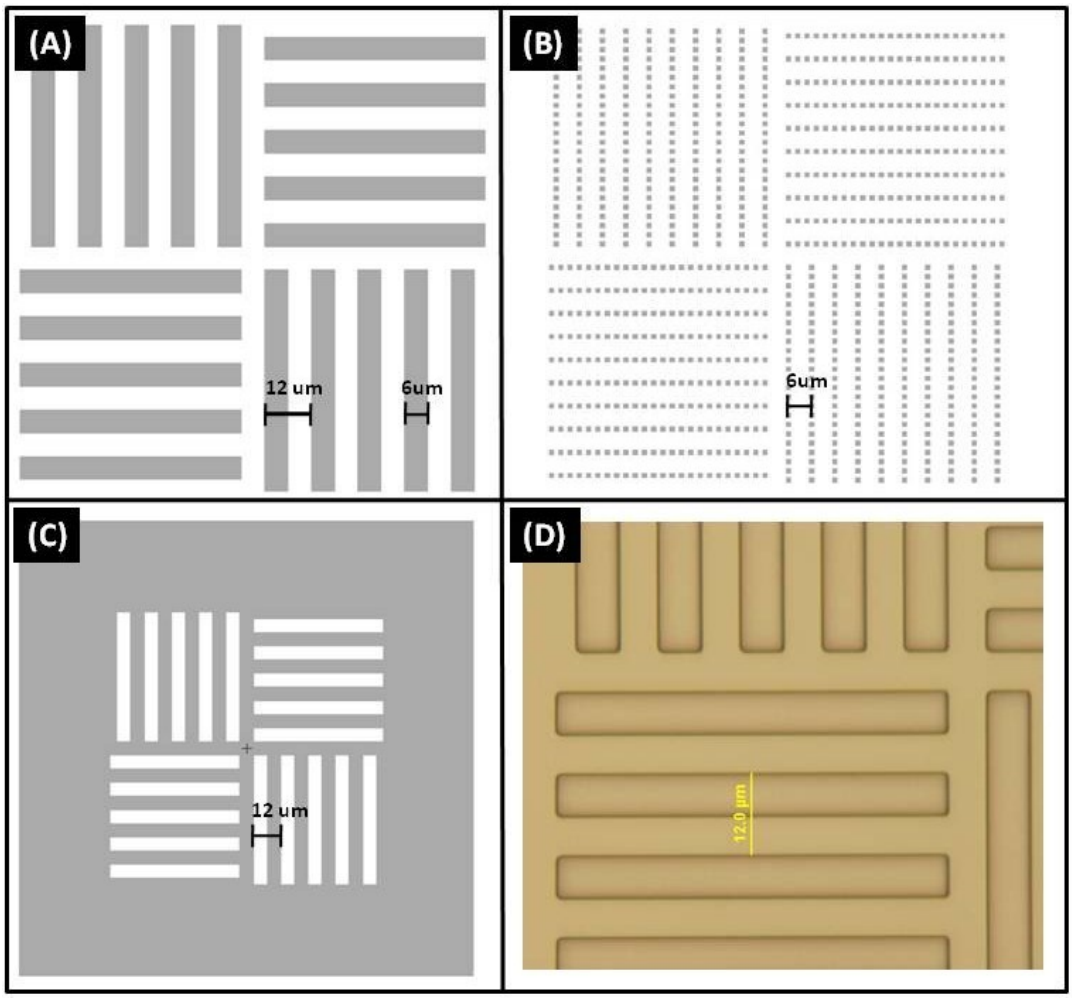
(A)
12 um
6um
(B)
6um
(C)
12 um
(D)
12.0 µm

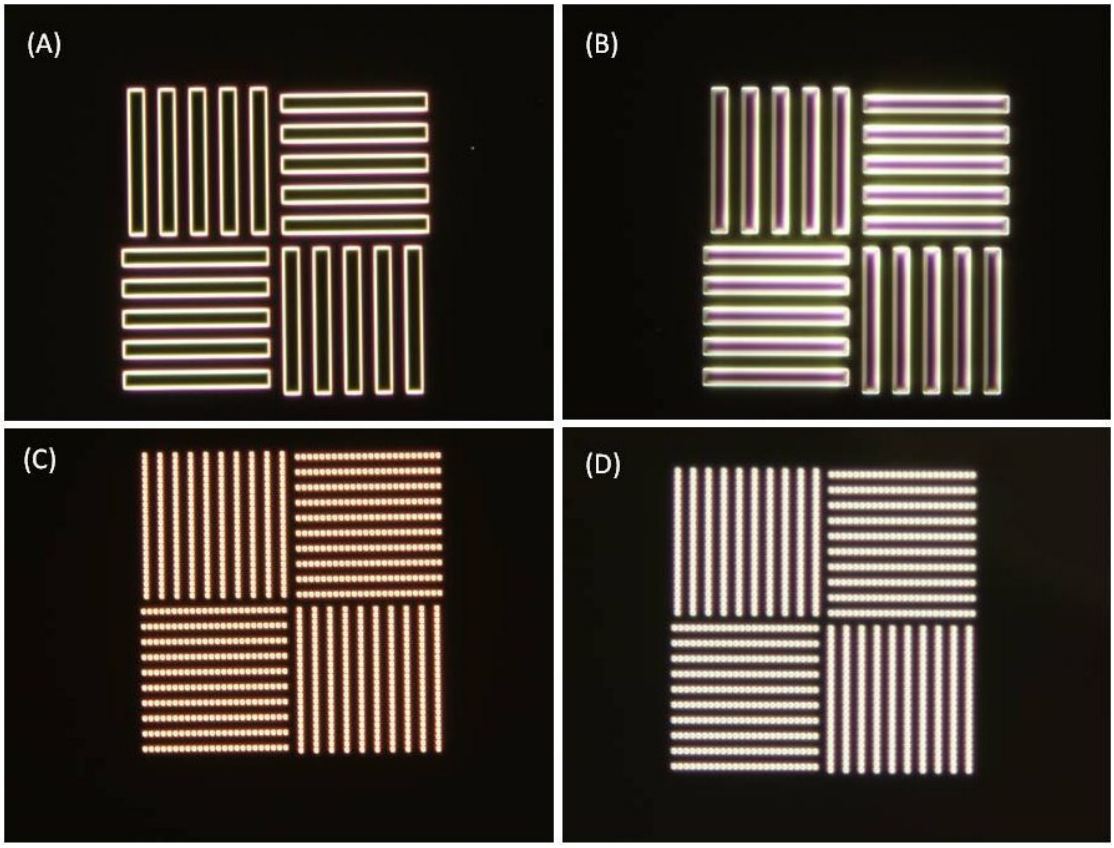

Figure 9. A) dark field image of μDFAS mark pattern 1 etched into fused silica. **B)** dark field image of μDFAS mark pattern 1 under SPR 955 0.9 photresist. Due to uneven filling of the rectangular etch mark trenches, the line edges of the etch marks become blurred the dark field. **C)** dark field image of μDFAS mark pattern 2 etched into fused silica. **D)** dark field image of μDFAS mark pattern 2 under SPR 955 0.9 photresist. Due to uneven filling of the rectangular etch mark holes, the line edges of the etch marks become blurred the dark field. However in the case of holes this does not matter since the entire hole is viewed as one "edge" by the μDFAS system.

least viscous lift off resist stocked by the CNF. If, however, there exist features on a pattern which are separated by less than a micron, then a thinner LOR film may be required. During development, after rapid dissolution of the exposed portions of

photoresist, the LOR directly underneath that photoresist is etched isotropically, immediately creating an undercut. It is required however, to continue to etch the LOR until it has completely cleared in the patterned spaces where metal is to be deposited. If the LOR is 500nm in thickness then the minimum lateral undercut is 500nm. For two features closer than 1 um apart, all of the LOR between them is etched. In the best case this results in a suspended bridge of photoresist which can still be used for lift off. Such a scenario is illustrated in figure 10B. More often however, that bridge of photoresist either tears away or collapses and the pattern must be reshot.

The solution to this is to use an LOR layer with a thickness on the order of 100nm, as is depicted in figure 10A. As it turns out, this is the case for the Pt electrode layer, since the gap between source and drain electrodes is roughly 1 um.

7.4.5 Effect of Nitride Deposition on CNT Electrical Properties

It is known that carbon nanotubes burn when heated in the presence of oxygen. They are similarly destroyed by oxygen plasma. Previous to the development of this fabrication process it had been reported that CNTs do not burn during silicon nitride using thermal CVD [9] [Mizutani]. Furthermore, one group reported that CNTs can also survive PECVD nitride deposition, while another group reported that PECVD immediately destroyed the tubes, and thermal CVD was used instead. While we are not able to use the thermal CVD furnaces in the CNF (material restrictions), we are permitted to use the GSI PECVD, as mentioned above. It is partly for this reason that silicon nitride was chosen as the capping material.

Figure 10. Photoresist and Lift-off Resist (LOR) profiles for two different thicknesses of LOR. The left column shows the profile of 100nm thick LOR during various stages. A) a fused silica wafer is prepared with 100nm LOR (red) and 900nm photoresist (blue). B) after exposure the wafer is placed into 300 MIF developer. Initially the exposed pattern in photoresist dissolves. C) Over the course of the development process, LOR is isotropically etched at a much slower rate than the exposed photoresist, but at a faster rate that the unexposed photoresist. D) A thin layer of metal is deposited by e-beam evaporation. E) fused silica wafer is prepared with 500nm LOR (red) and 900nm photoresist (blue). F-I) photoresist is developed and LOR is isotropically etched. If separation between two features 1000nm or less, then the LOR under the resist in between those features will completely clear. Thus it is possible to resist to collapse or tear off, affecting the pattern of evaporated metal.

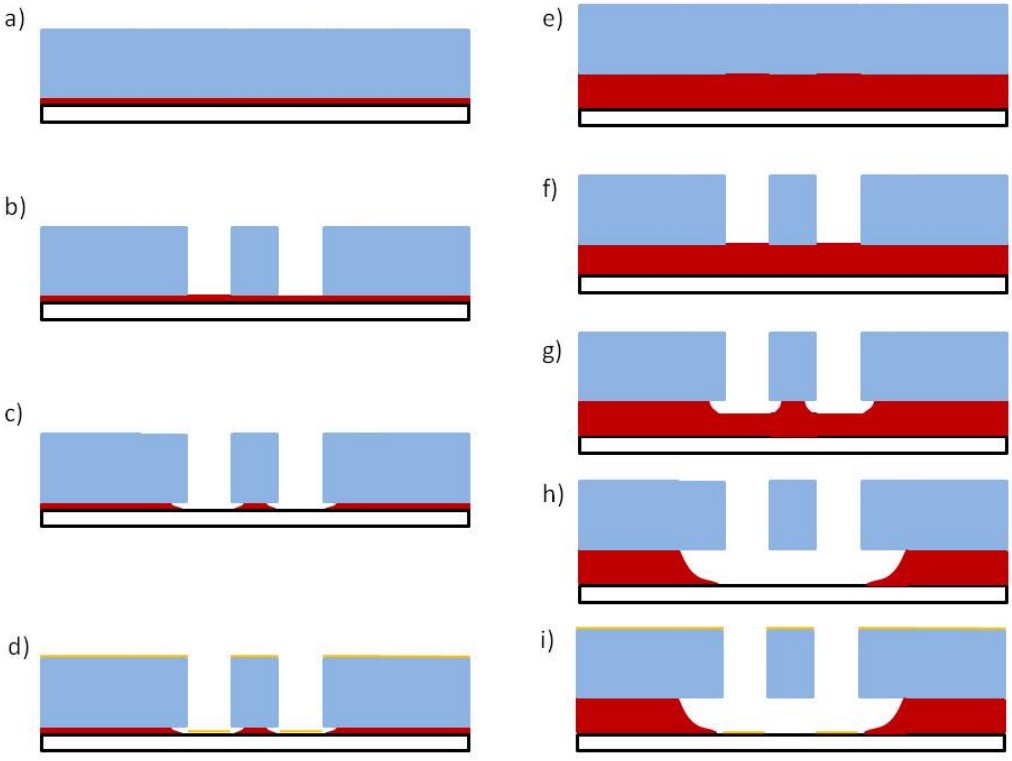
a)
b)
c)
d)
e)
f)
g)
h)
i)

Through our process development, we have verified the reports that CNTs can survive silicon nitride deposition by PECVD, but only given certain process restrictions. In the paper which reported CNT survival, only high frequency RF generated plasma was used during nitride deposition, however our process requires low frequency RF plasma in order to create low tensile stress nitride films. Thus the effect of low frequency RF plasma on bare carbon nanotubes had to be tested.

We observe that for purely high frequency RF PECVD nitride deposition, individual carbon nanotubes appear to both increase and decrease their conductance, while the average conductance over many nanotubes does not change significantly. This is thought to be a result of interactions between nanotube surfaces and charges associated with the deposited silicon nitride, the removal of water vapor, or the removal of oxygen from the CNT surface [10-12]. We also observe that as the power of the low frequency RF is increased, both the individual and average nanotube conductances tend to decrease dramatically. Furthermore, we observe that this decrease in conductance only occurs as a result of the first few seconds of nitride deposition. After a short deposition, any subsequent nitride deposition does not result in a change of nanotube conductance, regardless of the duration or frequencies used.

It is our hypothesis, that the mechanism of nanotube destruction is physical bombardment of ions accelerated into the substrate surface by the low frequency electromagnetic field. Once nanotubes are covered by an initial layer of silicon nitride, they appear to be protected from further damage. This series of thoughts has resulted in our current method for depositing silicon nitride onto the carbon nanotubes. First, a silicon nitride film is deposited using a high frequency plasma for a short duration of time. Namely, 10nm of nitride is deposited over 5 sec. Following

deposition of this thin high stress film, a thick layer of low stress nitride is deposited using a dual frequency plasma. The 20 min deposition results in a low stress film which is 2 um in thickness and which has the mechanical properties required for the micro and nanochannel wall/ceiling material.

7.5 Chapter Conclusions

In this fabrication chapter we have presented a method for manufacturing nanochannel devices with integrated carbon nanotube sensors. The device performance requirements were shown to place several restrictions on the processing steps available for use. An overview of the finalized process was given, as were more detailed descriptions of each of the major processing steps. Several topics in device fabrication that had originally presented unforeseen challenges in development of the method were also discussed in an effort to explain the reasoning behind the final fabrication prescription.

REFERENCES

1. Lin, K.C. and S.C. Lee, *THE STRUCTURAL AND OPTICAL-PROPERTIES OF A-SINXH PREPARED BY PLASMA-ENHANCED CHEMICAL-VAPOR DEPOSITION.* Journal of Applied Physics, 1992. **72**(11): p. 5474-5482.
2. Parsons, G.N., J.H. Souk, and J. Batey, *LOW HYDROGEN CONTENT STOICHIOMETRIC SILICON-NITRIDE FILMS DEPOSITED BY PLASMA-ENHANCED CHEMICAL VAPOR-DEPOSITION.* Journal of Applied Physics, 1991. **70**(3): p. 1553-1560.
3. Walmsley, B.A., et al., *Effects of deposition temperature on the mechanical and physical properties of silicon nitride thin films.* Journal of Applied Physics, 2005. **98**(4): p. 6.
4. **Martyniuk, M.**, et al., *Stress in low-temperature plasma enhanced chemical vapour deposited silicon nitride thin films.* Smart Materials and Structures, 2006.
5. Pearce, C.W., et al., *CHARACTERISTICS OF SILICON-NITRIDE DEPOSITED BY PLASMA-ENHANCED CHEMICAL VAPOR-DEPOSITION USING A DUAL FREQUENCY RADIOFREQUENCY SOURCE.* Journal of Applied Physics, 1992. **71**(4): p. 1838-1841.
6. Cianci, E., et al., *Dual frequency PECVD silicon nitride for fabrication of CMUTs' membranes.* Sensors and Actuators a-Physical, 2006. **127**(1): p. 80-87.
7. *Thermal Expansion, Nonmetallic Solids*. Thermophyisical Properties of Matter, the TPRC Data Series. Vol. 13. 1977, IFI Plenum: NY, NY.
8. Zhang, G.Y., et al., *Selective etching of metallic carbon nanotubes by gas-phase reaction.* Science, 2006. **314**(5801): p. 974-977.

9. Holt, J.K., et al., *Fabrication of a carbon nanotube-embedded silicon nitride membrane for studies of nanometer-scale mass transport.* Nano Letters, 2004. **4**: p. 2245-2250.
10. Mizutani, T., et al., *Effects of fabrication process on current-voltage characteristics of carbon nanotube field effect transistors.* Japanese Journal of Applied Physics Part 1-Regular Papers Short Notes & Review Papers, 2005. **44**(4A): p. 1599-1602.
11. Kojima, A., et al., *Air stable n-type top gate carbon nanotube filed effect transistors with silicon nitride insulator deposited by thermal chemical vapor deposition.* Japanese Journal of Applied Physics Part 2-Letters & Express Letters, 2005. **44**(8-11): p. L328-L330.
12. Chen, B.H., et al., *A carbon nanotube field effect transistor with tunable conduction-type by electrostatic effects.* Solid-State Electronics, 2006. **50**(7-8): p. 1341-1348.

CHAPTER 8

CONCLUSIONS AND FUTURE EXPERIMENTS

8.1 Summary of Key Results and Their Relevance

The original work on nanochannels, described in this thesis, was built upon a body of previously reported experimental results. Fluorescence video microscopy experiments were first performed on single DNA molecules moving through solution and gels in the early 1990's. Visualization of DNA strands in microchannels was first demonstrated in 1996, and in nanochannels in 2000. Much has been said regarding the mechanical properties of DNA in these environments. To describe the forces on a molecule in the shear flow of a microchannel, the worm-like chain molecule was used by Perkin's et al. Following the first nanochannel experiments the blob theory of DeGenne's was immediately applied. While it is recognized that DNA in sub-100 nm channels is at the limit of blob theory applicability, it is still used with great success to describe the statics and dynamics of confined molecules.

Blob theory was the model of choice for Chapter 2 of this thesis and is used to estimate the resolution limit for length measurements in nanochannels. While it is not explicitly utilized in the experiments of Chapter 4 and Chapter 5, on entropic recoil and spontaneous unfolding, a firm understanding of the theory informed the researchers in determining proper methods of analysis.

The recoil and unfolding experiments are novel as a demonstration of the precise control that can be achieved over single molecules using confinement induced forces. In Chapter 4, for the first time, the distinction between recoil and recoil-contract

processes was made. Molecules with looped front ends were shown to unfold with use of the entropically induced interfacial force, and a distinction was made between folded and knotted molecules. And in Chapter 5, spontaneous unfolding was shown to occur for folded molecules at rest in a channel. This experiment has validated the concept of entropically induced segregation of overlapping molecules in confinement. An experiment which was only briefly described in this thesis, but to which the author was a contributor, is the decompression experiment of Reccius et al. Previous single molecule measurements of DNA mechanics were limited to stretching the molecule by other means, such as with optical tweezers, elongational flow, or hooking around a post. As far as the authors are aware, the Reccius paper represented the first observation of single molecule DNA compression and free expansion dynamics, a topic which is a vital importance in the field of biology.

As discussed in Chapters 1, 2 and 3, nanofluidic channel based devices have technological applications in performing both length measurements and optical mapping measurements on single DNA molecules. The essential function of the nanochannel is molecular elongation, and compared to other methods of stretching, such as molecular combing and hydrodynamic stretching in microchannels (Chapters 1, 2 and 3), confinement induced elongation produces a higher degree of extension, and more uniform and consistent elongation.

Another experiment not discussed in depth in this thesis, but to which the author contributed, is the work by Reccius et al on rapid fragment length measurements using two laser beams focused on a nanochannel. As part of the analysis for this experiment, it was shown that folded molecules could be virtually unfolded, revealing their true contour length. It is believed that this type of analysis could help improve

the fraction of molecules passing through the channel that can be used in optical mapping experiments.

8.2 Future Directions and Conclusion

Nanochannel devices have been tested in the laboratory setting, and have been successfully employed to perform a number of biologically relevant measurements. There is, however, still much room for improvement in their performance. Here we outline several key aspects of "DNA in nanochannel" experiments which would benefit from further investigation.

The traditional Craighead group fabrication method for creating nanofluidic devices involves defining patterns with electron beam lithography, etching trenches directly into fused silica, and bonding a second wafer to enclose the trenches. The method was used for fabricating the devices of Chapters 4 and 5, and is known to be a convenient and reliable method. Using this approach one can produce channels with sub-$100\,nm$ diameters that are $10's$ of microns in length.

Several problems with the method have placed practical limits on observation of DNA in the channels. First, the channel walls and floors have a roughness on the order of $10nm$ at best. This estimate is based on SEM images of nanochannel regions and AFM scans of microchannel regions. Because of this roughness, the extension of DNA molecules in the channels likely undergoes some variation along the length of the molecule. In fact, many channel defects produce visible alterations in the extension of the molecules. These variations in intensity can be distinguished from thermal fluctuations in local extension and from photobleached portions of a molecule, because they remain fixed in place relative to the wafer as the DNA strand diffuses or

is driven through the channel. The worst of these defects act as constrictions, causing a DNA molecule travelling through the channel to highly compress at the location of the defect. Although these defects were useful for running experiments on DNA compaction and free expansion [1], in general they are undesirable.

One route toward devices with smoother channel walls may be to develop greater expertise at electron beam lithography. There are many factors involved in producing good e-beam patterns (type of resist, resist thickness, dose, development time, etc.) and the electron beam lithography processes used were almost certainly not optimized. It would also likely be fruitful if time were spent adjusting dry etch recipes for pattern transfer. Many factors are known to affect this process as well (resist sputtering, formation of fluorinated hydrocarbons, etc.), and, again, the processes are not yet optimized, in this author's opinion. It may also be interesting to investigate radically new approaches such as nanoimprint lithography or sacrificial layers based on an atomic layer deposition method. Much work has been done using nanoimprint to create long, narrow, and smooth channels already, and more could be done still [2].

According to the analysis of Chapter 2, the theoretical limit to the resolution for a single length measurements is imposed by statistical fluctuations of the molecule. It is also shown that hydrodynamic friction for the DNA increases as channel sizes decrease. An obvious route toward improving this fundamental limit is to create smaller channels, which increase molecular extension and which impose a greater friction on the molecule, thus holding it stable. In order to achieve this, the issue of surface roughness must be addressed.

Despite the degree of surface roughness in the present devices, useful measurements were made regarding DNA dynamics, as shown in Chapters 3, 4 and 5. In addition to the possibility that experimental results such as these will aid in the engineering of future lab on chip devices, they also fuel the development of polymer models by theorists in other research groups. There is still a tremendous amount of debate over statics and dynamics of DNA molecules in sub-$100\,nm$ channels, and many new theory papers are being published each year.

The experiments of Chapters 4 and 5 represent an initial investigation into various confinement induced effects. Both could benefit from a systematic variation in experimental parameters such as nanochannel diameter or ionic strength, and it appears that the community of theorists is eager for this to be done.

In addition to experiments in which more careful observation of DNA dynamics is conducted, there is also the possibility of varying some of the biological parameters. As reviewed in Chapter 3, experiments performed by the company U.S. Genomics utilize PNA nucleic acid probes to identify the location of target motifs on a backbone. We considered attempting the same experiment in nanochannels as opposed to microchannels, and a grant was written describing this goal. We had problems visualizing the hybridized probes and desisted at that point. However we know it is possible to do this. If it could be made to work for our group, the results for gene mapping on DNA molecules stretched in nanochannels would likely rival that for mapping on molecules stretching by elongational flow, and may even surpass it.

Using this method, the limit to the resolution for two nearby probes on a molecule would be set by diffraction and the measurement time. Part of the motivation for

building the nanotube/nanochannel device was to replace the optical probes of focused laser beams with much smaller electrical probes and thus circumvent this limit. In theory, one might be able to electrically detect a bound PNA strand as a perturbation of solution potential in addition to the perturbation caused by the double stranded DNA molecule itself. This would be an extremely small perturbation and it would likely require channels with depths and widths on the order of $5nm$ or so. At this point in time, it is not yet possible such to fabricate such a device, but it may be in the future.

Regardless, it is presently necessary to prove that detection of dsDNA is possible using the nanochannel/nanotube devices. As described in Chapters 6 and 7, a fabrication process for producing many of these devices has been developed. At the time of writing this thesis, roughly twenty new chips are in production and several new wafers worth of devices are farther up in the pipeline. It is hoped that electrical detection will soon be shown.

In conclusion, the study of single DNA molecules in nanofluidic channels is an exciting field of research. Continued progress in the field may lead to a number of important applications, ranging from further development of polymer theory to commercial nanofluidic devices for DNA manipulation and analysis. While many promising results have been demonstrated by a number of researchers, there is still much work to be done.

REFERENCES

1. Reccius, C.H., et al., *Compression and free expansion of single DNA molecules in nanochannels.* Physical Review Letters, 2005. **95**(26).
2. Liang, X.G., et al., *Single sub-20 nm wide, centimeter-long nanofluidic channel fabricated by novel nanoimprint Mold fabrication and direct imprinting.* Nano Letters, 2007. **7**: p. 3774-3780.

APPENDIX A

CALCULATION OF FULL CHEMICAL EQUILIBRIA FOR VARIOUS DILUTIONS OF TBE BUFFER WITH BETA-MERCAPTOETHANOL.

For a general introduction to calculation of chemical equilibria, the reader is referred to [1]. All Tris Borate EDTA (TBE) solutions used in the experiments of this thesis were purchased as 10X concentrate buffer.

Stock 10X TBE: 890 mMolar Tris-Borate; 20mM EDTA, pH 8.3

Five dilutions could be prepared by mixture with the appropriate volume of deionized water. The initial mixed concentrations for five possible TBE buffers are shown in Table 1.

Table 1. Dilutions of TBE Buffer

Component	5X with beta	1X with beta	0.5X with beta	0.05X with beta	0.005X with beta
Tris base	445 mM	89 mM	44.5 mM	8.9 mM	0.89 mM
Borate Acid	445 mM	89 mM	44.5 mM	8.9 mM	0.89 mM
EDTA	10 mM	2 mM	1 mM	0.2 mM	0.02 mM
2-mercaptoethanol	0.58 mM	0.58 mM	0.58 mM	0.58 mM	0.58 mM

For each of the dilutions, it is assumed that $pH = 8.3$. Tris is a weak base, boric acid is a weak acid, EDTA is a polyprotic acid, beta-mercaptoethanol is a weak acid. The following reactions are possible:

$Tris \leftrightarrow TrisH^+$ $\qquad pK_{a1} = 8.1$

$BoricAcid \leftrightarrow Borate^{-}$	$pK_{a2} = 9.24$
$EDTA \leftrightarrow EDTA^{-}$	$pK_{a3} = 1.99$
$EDTA^{-} \leftrightarrow EDTA^{2-}$	$pK_{a4} = 2.67$
$EDTA^{2-} \leftrightarrow EDTA^{3-}$	$pK_{a5} = 6.16$
$EDTA^{3-} \leftrightarrow EDTA^{4-}$	$pK_{a6} = 10.26$
$Beta \leftrightarrow Beta\_conjugate\_base^{-}$	$pK_{a7} = 9.6$

The Henderson Hasselback equation relates the pH, pK_a, and ratio of the concentrations of an acid and its conjugate base. Derivation of this equation can be found in Chapter 2.

$$pH = pK + \log\left[\frac{A^{-}}{HA}\right]$$

Since the solution *pH* and the electrolyte components' pK_a values are known, Equation 1 can be rearranged to solve for the ratio of the concentrations of each acid in solution with respect to its conjugate base.

$$\frac{[A^{-}]}{[HA]} = 10^{[pH - pK_A]}$$

1) We first determine the ratio of each of the acid/base conjugates for a solution $pH = 8.3$
2) After all seven ratios have been determined, we use the initial mixed concentration of acid or base along with the ratios, to calculate the absolute concentration for each of the amphoteric salts. The most cumbersome calculation is for EDTA:

$$x \cdot \left(\frac{[EDTA^-]}{[EDTA]} + \frac{[EDTA^{2-}]}{[EDTA^-]} \cdot \frac{[EDTA^-]}{[EDTA]} + \frac{[EDTA^{3-}]}{[EDTA^{2-}]} \cdot \frac{[EDTA^{2-}]}{[EDTA^-]} \cdot \frac{[EDTA^-]}{[EDTA]} + \frac{[EDTA^{4-}]}{[EDTA^{3-}]} \cdot \frac{[EDTA^{3-}]}{[EDTA^{2-}]} \cdot \frac{[EDTA^{2-}]}{[EDTA^-]} \cdot \frac{[EDTA^-]}{[EDTA]} \right) = [EDTA]_{Mixed}$$

$$x = \frac{[EDTA]_{Mixed}}{\left(\frac{[EDTA^-]}{[EDTA]} + \frac{[EDTA^{2-}]}{[EDTA^-]} \cdot \frac{[EDTA^-]}{[EDTA]} + \frac{[EDTA^{3-}]}{[EDTA^{2-}]} \cdot \frac{[EDTA^{2-}]}{[EDTA^-]} \cdot \frac{[EDTA^-]}{[EDTA]} + \frac{[EDTA^{4-}]}{[EDTA^{3-}]} \cdot \frac{[EDTA^{3-}]}{[EDTA^{2-}]} \cdot \frac{[EDTA^{2-}]}{[EDTA^-]} \cdot \frac{[EDTA^-]}{[EDTA]} \right)}$$

$$x = \frac{[EDTA]_{Mixed}}{\left(10^{(pH-pK_{a2})} + 10^{(pH-pK_{a3})} \cdot 10^{(pH-pK_{a2})} + 10^{(pH-pK_{a4})} \cdot 10^{(pH-pK_{a3})} \cdot 10^{(pH-pK_{a2})} + 10^{(pH-pK_{a5})} \cdot 10^{(pH-pK_{a4})} \cdot 10^{(pH-pK_{a3})} \cdot 10^{(pH-pK_{a2})} \right)}$$

Where, for example,

$$[EDTA^{3-}] = x \cdot \frac{[EDTA^{3-}]}{[EDTA^{2-}]} \cdot \frac{[EDTA^{2-}]}{[EDTA^-]} \cdot \frac{[EDTA^-]}{[EDTA]} \cdot [EDTA]_{Mixed}$$

Table 2. Expanded version of Table 1 including the final concentration for all species in solution. Concentrations are written in units of mM.

Species	5X with 4% beta	1X with 4% beta	0.5X with 4% beta	0.05X with 4% beta	0.005X with 4% beta
Tris base	272.8	54.6	27.6	5.5	0.5
TrisH +	172.2	34.4	17.4	3.4	0.3
Borate Acid	399.2	79.8	40.4	8.0	0.8
Borate -	45.8	9.2	4.6	0.9	0.1
EDTA	0	0	0	0	0
EDTA-	0	0	0	0	0
EDTA 2-	0.07	0.01	0.007	0.001	0.0001
EDTA 3-	9.82	1.96	0.982	0.196	0.019
EDTA 4-	0.108	0.0215	0.0108	0.0022	0.0002
2-mercaptoethanol	0.556	0.556	0.556	0.556	0.556
2-mercaptoethanol	0.0278	0.0278	0.0278	0.0278	0.0278

Table 3. Ionic strength, debye screening length, and zeta potential at the fused silica/ electrolyte shear plane for various buffer concentrations. All values for ionic strength and debye screening length are calculated using theoretical models. The value for zeta potential in 1X buffer was measured experimentally in the literature. Values for zeta potential at different ionic strengths are extrapolated using equation XX, the validity of which is described by [2]

As-mixed Component	5X with beta	1X with beta	0.5X with beta	0.05X with beta	0.005X with beta
Ionic Strength	0.15 M	0.031 M	0.016 M	0.0031 M	0.0003 M
Debye Screening Length	0.78 nm	1.8 nm	2.5 nm	5.5 nm	17 nm
Fused Silica Zeta Potential	-21 mV	-40 mV	-48 mV		

REFERENCES

1. Segel, I.H., *Biochemical Calculations 2nd Edition*. 2nd ed. 1976: John Wiley & Sons.
2. Kirby, B.J. and E.F. Hasselbrink, *Zeta potential of microfluidic substrates: 1. Theory, experimental techniques, and effects on separations.* Electrophoresis, 2004. **25**(2): p. 187-202.

APPENDIX B: DETAILED FABRICATION RECIPE

B-1 Alignment Layer

1. Pre-processing:
    a. Obtain three, 100mm diameter, 170μm thick, fused silica wafers. (Mark Optics) Wafers should have a scratch dig parameter of 40/20 or lower, and an RMS surface roughness of $< 20 \overset{\circ}{A}$.
    b. Scribe Wafer Numbers onto back of wafers using a diamond scribe. For scribing, it is recommended that wafers be placed face down on blue cleanroom paper and not a beta wipe. The beta wipe gives too much and can result in wafer cracking. In order to be consistent with what has previously been done, place the wafer with the flat closest to you. Write the mirror image of the number in the lower right hand corner. The results in the number appearing correctly, and in the lower left hand corner when observed from the device side of the wafer.
    c. Clean wafers in an automated spin-rinse-dry machine. Use care when loading boat. If wafers touch the metal boat holder when loading they can crack.
2. Photoresist Prep:
    a. p-20 primer; spin @ 3000 RPM, 5000 R/S, 45 sec
    b. SPR 220 3.0 Photoresist; spin @ 3000 RPM, 5000 R/S, 45 sec
    c. Bake on hotplate @ 115C for 2 min.
3. Photolithography (Autostep)
    a. Load mask: NTSLEVEL1

b. Command “Exec NTSWAFER \LVL1”; use exposure time of 0.3 sec
c. Post exposure bake @ 115C for 2 min
d. Develop in 300 MIF for 90 sec. via hand dip and agitation.

4. Reactive Ion Etch (Oxford 80#1 or Oxford 80#2)
    a. Descum wafers using 20sec. O2 plasma @ 150W
    b. CHF3/O2 Oxide Recipe; etch for either 59 min (Oxford 80#)1 or 1hr. 20min (Oxford 80#2)
    c. Fluorinated Polymer Removal using 40 sec. O2 plasma @ 150W
5. Resist Strip. Clean wafers using hot resist strip bath for ~2 hrs, followed by spin-rinse-dry.

B-2 Pt/Ti Electrode Layer

1. Photoresist Prep:
    a. p-20 primer; spin @ 4000 RPM, 10,000 R/S, 45 sec
    b. LOR 1A (lift off resist); spin @ 4000 RPM, 10,000 R/S, 45 sec
    c. Bake on hotplate @ 180C for 5 min.
    d. SPR 955 0.9 Photoresist; spin @ 4000 RPM, 5000 R/S, 45 sec
    e. Bake on hotplate @ 100C for 2 min.
2. Photolithography (Autostep)
    a. Load masks: NTSLEVEL5G
    b. Command “MAP NTSWAFER \LVL5G”; use exposure time of 0.14 sec.
    c. Post exposure bake @ 115C for 2 min
    d. Develop in 300 MIF for 60 sec. via hand dip and agitation.
3. Descum (Branson): run standard photoresist descum for 1 min.

4. E-beam Evaporation of Ti/Pt (Even Hour or Odd Hour Evaporator)
    a. load samples, titanium slug, Craighead group platinum slug, and new QCM
    b. evaporate 4nm titanium at rate of 0.2-0.4 $\mathring{A}/s$
    c. evaporate 30nm platinum at rate of 0.2-0.4 $\mathring{A}/s$
5. Ti/Pt Lift-Off
    a. Place wafers in '1165' microposit remover and let sit overnight
    b. (next day) Sonicate for 20-30 min., transfer wafers to IPA, remove from IPA and dry with Nitrogen.

B-3 Aluminum Oxide Supported Cobalt Catalyst Layer

1. Photoresist Prep:
    a. p-20 primer; spin @ 4000 RPM, 10,000 R/S, 45 sec
    b. LOR 1A (lift off resist); spin @ 4000 RPM, 10,000 R/S, 45 sec
    c. Bake on hotplate @ 180C for 5 min.
    d. SPR 955 0.9 Photoresist; spin @ 4000 RPM, 5000 R/S, 45 sec
    e. Bake on hotplate @ 100C for 2 min.
2. Photolithography (Autostep)
    a. Load masks: NTSLEVEL4G
    b. Command "MAP NTSWAFER \LVL4G"; use exposure time of 0.14 sec.
    c. Post exposure bake @ 115C for 2 min
    d. Develop in 300 MIF for 75 sec. via hand dip and agitation.
3. Descum (Branson): run standard photoresist descum for 1 min.
4. E-beam Evaporation of Al2O3 supported Cobalt Catalysis (Even Hour Evaporator Only)

a. load samples, titanium slug, aluminum oxide cobalt slug, and new QCM.
b. evaporate 0.3 nm titanium at rate of 0.1 $\mathring{A}/s$
c. evaporate 15nm aluminum oxide at rate of 0.2-0.4 $\mathring{A}/s$
d. evaporate 0.25 nm cobalt at rate of 0.1 $\mathring{A}/s$

5. Supported Catalyst Lift-Off
    a. Place wafers in '1165' microposit remover and let sit overnight
    b. (next day) Sonicate for 20-30 min., transfer wafers to IPA, remove from IPA and dry with Nitrogen.

B-4 Wafer Dicing

1. Photoresist Prep (to protect features from dicing saw debris):
    a. SPR 220 7.0 Photoresist; spin @ 2000 RPM, 1000 R/S, 45 sec
    b. Bake on hotplate @ 115C for 2 min.
2. Dicing (Wafer Saw)
    a. Dice wafers into 20mm X 20 mm squares
    b. Peel tape from chips. Scribe labels onto chips so that numbers are visible and readable in lower left hand corner of chip when looking at the device side.
3. Photoresist Strip
    a. Place chips in '1165' microposit remover and let sit for several hours or more.
    b. Sonicate for 20-30 min., transfer wafers to IPA, remove from IPA and dry with Nitrogen.

B-5 Carbon Nanotube Growth

1. CVD growth of single walled carbon nanotubes using modified ethylene growth recipe in Paul McEuen lab Furnace #1:
    a. Clean furnace tube by baking each segment at 900C for 10 min. Cool to 500C.
    b. Insert 3 Chips into the tube at the center of the furnace. The words "CNF" should be on the downstream edge of each chip. Calcine chips by baking in atmosphere (tube ends open) for 30 min at 500C. Cool to room temp (furnace thermometer <100C).
    c. Attach hoses to ends of tube and pre-flow process gases at room temp in order to purge system of oxygen. Using the electronic gas flow controllers, flow the following for ~10 min:
        i. 0.8 SLM Ar
        ii. 0.2 SLM H2
        iii. 5.5 SCCM C2H4
    d. Switch off ethylene, and continue flowing argon and hydrogen. Raise temperature to 700C and hold this for 30min. This serves to reduce the catalysts.
    e. Raise temperature to 800C, wait 3 min.
    f. Add ethylene while maintaining hydrogen and argon. Hold this for 10 min. This is the CNT growth stage.
    g. Subtract ethylene. Reduce temperature to room temp, while maintaining hyrdrogen and argon flow.
    h. Turn off all gases, open ends of furnace tube and remove chips. Place chips in conductive cases only to reduce probability of static charge accumulation.

2. Probe Station Measurements (optional). At this stage it is a good idea to perform DC source drain measurements on the 38 sensor regions of each chip. Three or four chips can be tested in about 1 hour.
    a. Before performing measurements, take measured to reduce the likelihood of nanotube destruction from static charge. Ensure that relative humidity of room is around 45%. Use desktop deionizer. Individually connect each drain to ground with a 10 giga-ohm resistor in series. If static charge has built up this last step will help to slowly dissipate it.
    b. It is also possible to electrolytically gate tubes at this point, using a drop of salty water and a third, gate electrode. If this is done, be sure to rinse chip with DI water before drying.

B-6 Thin Silicon Nitride Layer

1. GSI PECVD for deposition of thin silicon nitride "protective" layer. First use "High Stress Nitride" recipe with the following modifications.
    a. Temperature = 300C
    b. RF#1 = 35% power; RF#2 = 0% Power
    c. Deposition time between 2 sec and 5 sec.
2. Next use "Low Stress Nitride" recipe with the following modifications.
    a. Temperature = 300C
    b. RF#1 = 35% power; RF#2 = 0% Power
    c. Deposition time between 5 and 10 sec, depending on the desired thickness of the nitride protective later.

B-7 Micrchannel/Nanochannel Sacrificial Chromium Layer

1. Photoresist Prep:
    a. p-20 primer; spin @ 4000 RPM, 10,000 R/S, 45 sec
    b. LOR 1A (lift off resist); spin @ 4000 RPM, 10,000 R/S, 45 sec
    c. Bake on hotplate @ 180C for 5 min.
    d. SPR 955 0.9 Photoresist; spin @ 4000 RPM, 5000 R/S, 45 sec
    e. Bake on hotplate @ 100C for 2 min.
2. Photolithography (Autostep)
    a. Load masks: NTSLEVEL2G and NTSLEVEL3G
    b. Command “MAP NTSCHIP \LVL2G”; use exposure time of 0.14 sec.
    c. Command “MAP NTSCHIP \LVL2G”; use exposure time of 0.14 sec.
    d. Post exposure bake @ 115C for 2 min
    e. Develop in 300 MIF for 75 sec. via hand dip and agitation.
3. Descum (Branson): run standard photoresist descum for 1 min.
4. E-beam Evaporation of Chromium (Even Hour or Odd Hour Evaporator)
    a. load samples, chromium, and new QCM
    b. evaporate 10nm chromium at rate of 0.2-0.4 $\mathring{A}/s$
5. Chromium Lift Off
    a. Place wafers in ‘1165’ microposit remover and let sit overnight
    b. (next day) Sonicate for 20-30 min., transfer wafers to IPA, remove from IPA and dry with Nitrogen.

B-8 Thick Silicon Nitride Layer

GSI PECVD for deposition of thick silicon nitride layer. Use "Low Stress Nitride" recipe with the following modifications.

a. Temperature = 300C
b. RF#1 = 35%; RF#2 = 0% Power
c. Deposit for 5 sec. This results in a thin film for CNT protection.
d. RF#1 = 19% power; RF#2 = 80% Power
e. Deposit for 20 min. This results in approximately 2 microns of nitride.

B-9 Access Hole Layer #1

1. Photoresist Prep:
    a. p-20 primer; spin @ 3000 RPM, 5000 R/S, 45 sec
    b. SPR 220 3.0 Photoresist; spin @ 3000 RPM, 5000 R/S, 45 sec
    c. Bake on hotplate @ 115C for 2 min.
2. Photolithography (Autostep)
    a. Load masks: NTSLEVEL6G, NTSLEVEL7G, NTSLEVEL8G
    b. Command "Exec NTSCHIP \LVL6G"; use exposure time of 0.3 sec
    c. Command "Exec NTSCHIP \LVL7G"; use exposure time of 0.36 sec
    d. Command "Exec NTSCHIP \LVL8G"; use exposure time of 0.3 sec
    e. Post exposure bake @ 115C for 2 min
    f. Develop in 300 MIF for 90 sec. via hand dip and agitation.
3. Reactive Ion Etch (Oxford 80#1 or Oxford 80#2)
    a. Descum wafers using 20sec. O2 plasma @ 150W
    b. CHF3/O2 Nitride Recipe; etch for 40 min (Oxford 80#2).

c. Fluorinated Polymer Removal using 40 sec. O2 plasma @ 150W

4. Resist Strip. Clean wafers using '1165' microposit remover. Soak for several hours or overnight. Transfer to IPA and then dry with nitrogen.

B-10 Wet Chemical Etch of Chromium Sacrificial Material

1. Place chips in Cr-14 chrome etch (acid hood in CNF). Etch for 6-8 hours or overnight.
2. Transfer chips to a beaker of dH2O . Move dH2O beaker with chips to the photoresist hood. Allow chips to soak for 15-30min.
3. Either …
    a. Transfer chips to beaker of IPA. Let soak for 5 min. Remove and dry with nitrogen, and then do electrical measurements on chips, or
    b. continue to step 7.4.11-2 without transferring to IPA and drying.

B-11 Wet Chemical Etch of Thin Protective Nitride Layer

1. Insert chips into a beaker of IPA. Let soak for 5 min.
2. Transfer chips to a beaker of dH2O. Transfer chips to a beaker of MF 312 (5% TMAH)
3. Move beaker with chips into Base Hood in CNF.
4. Transfer chips into a heated beaker of MF 312 (this beaker should be pre-heated to 70C). Etch at 70C for 20-60 min, depending on the thickness of protective nitride that must be removed.
5. Transfer chips to beaker of dH2O. Move dH2O beaker with chips to the photoresist hood. Transfer chips to beaker of IPA. Let soak for 5 min. Remove and dry with nitrogen, and then do electrical DC measurements on chips.

B-12 Deposition of Thin Silicon Nitride Layer #2

1. GSI PECVD for deposition of thin silicon nitride “protective” layer. Use “Low Stress Nitride” recipe with the following modifications.
2. Temperature = 300C
3. RF#1 = 19% power; RF#2 = 80% Power
4. Deposition time = 5 min.

B-13 Access Hole Layer #2

1. Photoresist Prep:
    a. p-20 primer; spin @ 3000 RPM, 5000 R/S, 45 sec
    b. SPR 220 3.0 Photoresist; spin @ 3000 RPM, 5000 R/S, 45 sec
    c. Bake on hotplate @ 115C for 2 min.
2. Photolithography (Autostep)
    a. Load mask: NTSLEVEL7G
    b. Command “Exec NTSCHIP \LVL7G”; use exposure time of 0.3 sec
    c. Post exposure bake @ 115C for 2 min
    d. Develop in 300 MIF for 90 sec. via hand dip and agitation.
3. Reactive Ion Etch (Oxford 80#1 or Oxford 80#2)
    a. Descum wafers using 20sec. O2 plasma @ 150W
    b. CHF3/O2 Nitride Recipe; etch for either 5-7 min (Oxford 80#)1 or 7-9 min (Oxford 80#2).
    c. Fluorinated Polymer Removal using 40 sec. O2 plasma @ 150W
4. Resist Strip. Clean wafers using ‘1165’ microposit remover. Soak for several hours or overnight. Transfer to IPA and then dry with nitrogen.

B-14 Macroscopic Reservoir Attachment

1. Scratch openings at the end of each microchannel using a diamond scribe. This can be done fairly precisely while using the McEuen probestation objective and camera setup.
2. Prepare six reservoirs by slicing the ends off of pipet tips with a razor blade. Put RTV sealant on the bottom edge of each pipet tip before pressing it to the surface at the microchannel end. Be careful not to put too much glue, not to press to hard, and to place the reservoir carefully so that the RTV sealant does not clog the opening of the microchannel. With a little bit of practice this can be done correctly every time.